DEVELOPMENT OF A SOLID STATE SPOT WELDING TECHNIQUE FOR THE MANUFACTURING OF DEFECT FREE JOINTS

A Dissertation

by

Isam Jabbar Ibrahim

Submitted to the

Graduate School of Sciences and Engineering
In Partial Fulfillment of the Requirements for
the Degree of

Doctor of Philosophy

in the
Department of Mechanical Engineering

Özyeğin University
June 2019

Copyright © 2019 by Isam Jabbar Ibrahim

DEVELOPMENT OF A SOLID STATE SPOT WELDING TECHNIQUE FOR THE MANUFACTURING OF DEFECT FREE JOINTS

Approved by:

Assoc. Prof. Dr. Güney Güven YAPICI,
Advisor,
Department of Mechanical Engineering
Head of Department
Özyeğin University

Assist. Prof. Dr. Altuğ BAŞOL,
Department of Mechanical Engineering
Özyeğin University

Assist. Prof. Dr. Polat ŞENDUR,
Department of Mechanical Engineering
Özyeğin University

Assist. Prof. Dr. Mehmet İPEKOĞLU,
Department of Mechatronic Systems Engineering
Turkish-German University

Assist. Prof. Dr. Yasemin Şengül TEZEL,
Faculty of Engineering and Natural Sciences
Sabancı University

Date Approved: June 2019

To my mother, wife, and my children…

ABSTRACT

Development of a Solid State Spot Welding Technique for the Manufacturing of Defect Free Joints

Friction stir spot welding (FSSW) processing is a recently developed process for joining hard weldability materials, which has expanded into automotive applications by using the concept of light alloys. Thus, by reducing its fuel consumption, FSSW as a solid-state welding method does not need to melt the workpieces used, which has attracted the attention of automotive manufacturing companies around the world.

Although considerable research has been conducted to observe the advantages of the FSSW process, rather more attention has been paid to solving the probe hole (keyhole) defect, which appears at the weld spot center in the welds as a result of the pin of the welding tool after joining process is complete. This study investigates the fabrication of flat friction stir spot welds without the keyhole by using a newly developed FSSW process, which uses the intermediate layer (IL) part, and tracks the mechanical properties of the fabricated welds.

The welds produced by the Intermediate Layer FSSW (IL-FSSW) process showed an excellent appearance with no large distortion resulting from the welded sheets. The top surface of the spot weld showed a smooth, flat surface. Regardless of the use of different welding parameters, the appearances of all the spot welds were comparable. It is considerable that no keyhole is formed in comparison with the conventional FSSW welds.

It was shown that using the IL part improved the lap shear failure force (LSFF). Some of the welded samples, which were about two folds relative to the maximum value of the

American Welding Society (AWS) welds quality requirements. In order to understand the effect of the welding parameters on the tensile behavior, design of experiment (DOE) were utilized to optimize the results of the tensile test. The optimization work indicated that the LSFF increases linearly with the increasing plunging depth. The analysis of the variance (ANOVA) statistical method in respect to LSFF indicates that the tool rotation speed was the most significant parameter, whereas the plunging feed rate was the lower one in this regard.

The fatigue tests were conducted under T6 and annealing (O) conditions and over N_f of the lap welded samples of the dissimilar Al 6061/Al 2024 and similar Al 6061/Al 2024 alloys, which were determined for all the conditions. In all the samples, the annealing treatment was observed to have a negative effect on the N_f under high applied loads. However, no heat treatment effect was clearly observed under the low load levels, except in Al 2024, in which the annealing treatment had a positive effect on the N_f.

In terms of the Al/Cu welds, the flat weld spots without the keyhole were produced successfully. The results revealed that there was very little difference in the LSFF achieved with the IL-FSSW using the pinless tool when compared to the welds conducted with the conventional FSSW using a tool with a pin. The X-ray diffraction (XRD) analyses showed that the Al_2Cu and Al_4Cu_9 phases formed as a result of the peritectic reactions at the interface of the sheets within the weld nugget. The Vickers examination showed distinctly different microhardness levels up to 575 Hv, which are superior to that of the base metal corresponding to the hard intermetallic compounds formed in the weld nugget.

Two finite element models were built to simulate the IL-FSSW process, i.e. thermal and mechanical. The temperature distributions obtained from the thermal model were

compared with the experimental measurements with decent agreement. The mechanical model is utilized to predict the strength of the joints in conjunction with the experimental values from shear-tensile tests, providing satisfactory results for demonstrating the trends in the mechanical behavior of various joints.

ÖZET

Kusursuz Bağlantıların İmalatı İçin Katı Hal Nokta Kaynağı Tekniğinin Geliştirilmesi

Sürtünme karıştırma nokta kaynağı (FSSW) işlemi, hafif alaşımlar konseptini kullanarak otomotiv uygulamalarına genişleyen zor kaynaklanan malzemelerin birleştirilmesi için yakın zamanda geliştirilen bir işlemdir. Bu nedenle, katı hal kaynak yöntemi olarak FSSW, kullanılan iş parçalarını ergitmek durumunda kalmadığı ve yakıt tüketimini azalttığı için dünyadaki otomotiv üretici firmalarının dikkatini çekmiştir.

FSSW işleminin avantajlarını gözlemlemek için önemli araştırmalar yapılmış olmasına rağmen, takım piminin bir sonucu olarak kaynak noktasındaki pim deliği (anahtar deliği) kusuruna daha fazla önem verilmiştir. Bu çalışma, orta katman (IL) parçasını kullanan ve üretilen kaynakların mekanik özelliklerini sergileyen yeni geliştirilen bir FSSW işlemi kullanarak, anahtar deliği olmadan düz yüzeyli sürtünme karıştırma nokta kaynaklarının imalatını araştırmaktadır.

Orta katman FSSW (IL-FSSW) işlemi kullanılarak üretilen kaynaklar, büyük bir çarpılma olmadan mükemmel bir görünüm sergilemiştir. Nokta kaynağının üst yüzeyi pürüzsüz ve düz bir yüzey göstermiştir. Farklı kaynak parametrelerinin kullanılmasından bağımsız olarak, tüm nokta kaynaklarının görünümleri karşılaştırılabilir durumdadır. Geleneksel FSSW kaynaklarına kıyasla herhangi anahtar deliği kusurunun oluşmaması oldukça önemlidir.

IL parçasını kullanmanın, bindirmeli kesme kırılma kuvvetini (LSFF) Amerikan Kaynak Topluluğu (AWS) kaynaklarının kalite gereksinimlerinin maksimum değerinin yaklaşık iki katına geliştirdiği gösterilmiştir. Kaynak parametrelerinin çekme davranışı üzerindeki etkisini anlamak için çekme testi sonuçlarının eniyilenmesi için deney tasarımı (DOE) kullanılmıştır. Optimizasyon çalışması, LSFF'nin artan dalma derinliği ile doğrusal olarak arttığını göstermiştir. LSFF'ye göre varyans (ANOVA) istatistiksel yönteminin analizi, takım dönme hızının en önemli parametre olduğunu gösterirken, dalma besleme hızı bu konuda çok ciddi etkisinin olmadığını gözlemlemiştir.

Yorulma testleri, T6 ve tavlama (O) koşulları altında, benzer ve benzer olmayan Al 6061 / Al 2024 alaşımlarının bindirmeli kaynaklı numunelerinin kırılma döngü sayısına (N_f) etkisini belirlemek için gerçekleştirilmiştir. Tüm numuneler için tavlama işleminin yüksek seviyede uygulanan yükler altında N_f üzerinde olumsuz bir etkiye sahip olduğu gözlenmiştir. Bununla birlikte, numunelerin düşük yük seviyelerindeki N_f'i üzerinde ısıl işlemin etkisi gözlemlenmeden yalnızca Al 2024'te tavlama işleminin olumlu etkisi açıkça gözlemlenmiştir.

Al / Cu kaynakları açısından, anahtar deliği olmayan düz kaynak noktaları başarıyla üretildi. Sonuçlar, pimsiz takım kullanılan IL-FSSW ile elde edilen LSFF değerleri ile pimli bir takımın kullanıldığı geleneksel FSSW ile elde edilen değerler ile karşılaştırıldığında çok az bir fark olduğu ortaya çıkarıldı. X ışını kırınımı (XRD) analizleri, Al_2Cu ve Al_4Cu_9 fazlarının, levhaların ara yüzündeki kaynak bölgesinde meydana gelen ötektik ve peritektik reaksiyonların bir sonucu olarak oluştuğunu göstermiştir. Vickers sertlik incelemesi, kaynak

bölgesinde oluşan sert metaller arası bileşiklere tekabül eden 575 Hv seviyesinde mikro sertlik göstermiştir.

IL-FSSW işleminin termal ve mekanik benzetimi için iki sonlu eleman modeli geliştirilmiştir. Termal modelden elde edilen sıcaklık dağılımları deneysel ölçümlerle karşılaştırılmış ve uygunluk gösterilmiştir. Mekanik model, kesme-çekme testlerinden elde edilen deneysel değerlerle birlikte bağlantıların gücünü tahmin etmek için kullanımış olup, çeşitli bağlantıların mekanik davranışındaki eğilimleri sergilemek için tatmin edici sonuçlar vermiştir.

ACKNOWLEDGEMENTS

First and foremost, I would like to thank my supervisor, Dr. Güney Güven Yapıcı, for his invaluable advice throughout the course of my research project. Without his guidance and support, I would not have been able to be successful in this field of study.

I would also like to acknowledge the other members of my dissertation committee for their valuable contributions to this dissertation.

I am grateful to Mr. Ulaş Yıldırım for his help with the preparation of samples. Also, I'd like to sincerely thank my colleagues in the MEMFIS group Ali Hosseinzadeh, Onur Bilgin, Veghar Mohammadi, and Görkem Şimşek for the enjoyable time I spent with them. Special thanks go to my best friend, Dhyai Hassan, for his valuable helps and comments.

I would also like to thank my colleagues in Iraq, Isam Tariq and Oday Wadee, not only for their contributions to this project, but also for introducing a new aspect of a positive attitude to me, which I will consider throughout life. I would like to thank Prof. Dr. Hatim Mahmood for his collaboration during my stay for performing the experimental tests in Baghdad, Iraq.

Finally, I would like to dedicate this dissertation to my family and my wife Duaa. It is with their unreserved love and support that I keep moving forward. My sincere thanks go out to my dear father-in-law, Mr. Akram Ali for his support and kindness. This dissertation could not have been completed without their encouragement.

Thank you,

Isam

TABLE OF CONTENTS

ABSTRACT ..... **iv**

ÖZET ..... **vii**

ACKNOWLEDGEMENTS ..... **x**

LIST OF TABLES ..... **xvi**

LIST OF FIGURES ..... **xvii**

1. INTRODUCTION **1**

1.1 Motivation 1

1.2 Research Objectives 3

1.3 Work Summary 4

2. BACKGROUND AND LITERATURE REVIEW **6**

2.1 Friction Stir Welding (FSW) 6

2.2 Friction Stir Spot Welding (FSSW) 8

2.2.1 FSSW Versus Other Single Point Joining Processes 10

2.2.2 Effect of FSSW Parameters on Welding Quality 13

2.2.3 The Keyhole Problem of FSSW 15

2.3 Weldability of Al 6061 and Al 2024 Alloys, and FSSW Applications 18

2.4 Weldability of Aluminum to Copper Alloys, and FSSW Applications 24

2.5 FSSW Applications of Other Materials 27

2.6 Design of Experiment (DOE) Applications in FSSW 30

2.7 Finite Element Analysis of FSSW 33

2.8 Fatigue Behavior of FSSW Joints 35

2.9 The Intermediate Layer Friction Stir Spot Welding (IL-FSSW) 38

3. EXPERIMENTAL METHODS 40

3.1 As Received Materials Characterization 40

3.1.1 Al 6061 Aluminum Alloy 40

3.1.2 Al 2024 Aluminum Alloy 41

3.1.3 Pure Copper Alloy 42

3.2 Design of the Fixture and Welding Tool 42

3.3 IL-FSSW Process Parameters 43

3.4 Design of Experiment (DOE) Based on Taguchi Method 44

3.5 Mechanical Testing 48

3.5.1 Shear-Tensile Test 48

3.5.2 Hardness Measurement 49

3.5.3 Axial Load and Torque Measurement 49

3.5.4 Fatigue Test 51

3.6 Temperature Distribution Measurement 51

3.7 Microstructure Evaluation Methods 52

3.7.1 Optical Light Microscopy 52

3.7.2 Scanning Electron Microscopy (SEM) 53

3.8 X-Ray Diffraction Examination (XRD) 54

4. THE CHARACTERIZATIONS OF Al 6061 AND Al 2024 SIMILAR AND DISSIMILAR WELDS FABRICATED BY THE IL-FSSW PROCESS 55

4.1 Microstructure and Hardness Characterizations 55

4.1.1 Similar Welds of Al 6061 55

4.1.2 Similar Welds of Al 2024 59

4.1.3 Dissimilar Welds of Al 2024 to Al 6061 62

4.2 Mechanical Characterizations 66

4.3 Fracture Morphology Analysis 70

4.3.1 Similar Welds of Al 6061 70

4.3.2 Similar Welds of Al 2024 72

4.3.3 Dissimilar Welds of Al 2024 to Al 6061 75

4.4 Summary on Fabrication of Al 6061 and Al 2024 Welds by IL-FSSW 78

5. THE FATIGUE PROPERTIES OF Al 6061 AND Al 2024 SIMILAR AND DISSIMILAR WELDS FABRICATED BY IL-FSSW PROCESS 79

5.1 Fatigue Test of Similar Al 6061 Welds (Group 1) 79

5.1.1 Wohler Diagram 80

5.1.2 Appearance of Fracture 81

5.1.3 Fracture Morphology 85

5.2 Fatigue Test of Similar Al 2024 Welds (Group 2) 86

5.2.1 Wohler Diagram 87

5.2.2 Appearance of Fracture 88

5.2.3 Fracture Morphology 91

5.3 Fatigue Test of Dissimilar Al 2024/Al 6061 Welds (Group 3) 92

5.3.1 Wohler Diagram 93

5.3.2 Appearance of Fracture 94

5.3.3 Fracture Morphology 98

5.4 Summary of Fatigue Test 99

6. THE THERMAL AND MECHANICAL MODELS OF SIMILAR AND DISSIMILAR WELDS FABRICATED BY THE IL-FSSW PROCESS 100

6.1 Coupled-Field Analysis 100

6.2 The IL-FSSW Developed Models 101

6.2.1 The Model Analysis 101

6.2.2 Assumptions 102

6.2.3 Geometry 104

6.2.4 Elements Used 105

6.2.5 Mesh Generation 106

6.2.6 Material Properties 107

6.2.7 Boundary Conditions 111

6.3 Heat Generation in IL-FSSW 113

6.4 Temperature Distributions 117

6.5 Results of The Mechanical Model 121

6.6 The Summary 125

7. THE CHARACTERIZATIONS OF Pure Cu/Al 6061WELDS FABRICATED BY THE IL-FSSW PROCESS 126

7.1 Microstructure and Hardness Characterizations 126

7.2 Mechanical Characterizations 129

7.3 Analysis EDS and XRD Results 131

7.4 Analysis of Intermetallic Compounds Formation 134

7.5 Fracture Morphology Analysis 138

7.6 Summary of Al 6061/Cu Welds Fabricated by IL-FSSW 140

8. CONCLUSION 141

9. FUTURE WORKS 143

BIBLIOGRAPHY 144

VITA 162

LIST OF TABLES

Table 2.1 Aging effect on weld strength and hardness of Al 2024 [66] 22

Table 3.1 Standard and actual chemical compositions of Al 6061-T6 alloy (wt %)…….40

Table 3.2 Standard and actual chemical compositions of the Al 2024-T3 alloy (wt %) 41

Table 3.3 The Standard and actual chemical compositions of the pure Cu alloy (wt %) 42

Table 3.4 IL-FSSW processing parameters with their ranges and levels 44

Table 3.5 The welding parameters used and output responses of the average LSFF based on the Taguchi method 45

Table 4.1 UTS of the base metals used 68

Table 4.2 Comparison of the LSFF values between the AWS standard and experimental results 69

Table 5.1 Results of fatigue testing (Group 1) 79

Table 5.2 Results of fatigue testing (Group 2) 86

Table 5.3 Results of fatigue testing (Group 3) 93

Table 6.1 Temperature dependent material properties for Al 2024-T3 alloy [147,152]....108

Table 6.2 Temperature dependent material properties for Al 6061-T6 alloy [145,151]....108

Table 6.3 The contact diameter with respect to the plunging depth for both cases of the Al 6061-T6 and Al 6061-T6 to Al 2024-T3 weld processing 114

Table 6.4 P, μ, & Q for each step of plunging through welding of the Al 6061-T6 sheets116

Table 6.5 P, μ, & Q for each step of plunging through welding of Al 2024-T3 to Al 6061-T6 117

Table 6.6 The error values between the experimental and model results 125

LIST OF FIGURES

Figure 2.1 Schematic representation of the FSW [2].....7

Figure 2.2 (a) Schematic diagram of microstructural zones in friction stir welds of aluminum, (b) micrograph showing various micro-structural zones [22] 7

Figure 2.3 Schematic representation of the steps in the FSSW process [26] 8

Figure 2.4 Schematic of the resistance spot welding [30] 10

Figure 2.5 Schematic representation the resistance element welding [31].....11

Figure 2.6 Schematic of the joining process of self-piercing riveting [34] 12

Figure 2.7 Schematic of the joining process of mechanical clinching [34].....12

Figure 2.8 Effect of the rotational speed on the FSSW joints properties [38].....13

Figure 2.9 Shear separation load as a function of the shoulder penetration depth [43].....15

Figure 2.10 Schematic illustration of the RFSSW process [48]. 16

Figure 2.11 Schematic representation of the FSSW developed [52].....17

Figure 2.12 Schematic of the keyhole refilled FSSW process illustration [54].....17

Figure 2.13 The dimensions and tool design developed [55].....18

Figure 2.14 Weldability of various wrought aluminum alloys [57,58] 19

Figure 2.15 Lap-shear force for different welding parameters [63] 20

Figure 2.16 Effect of pin length and rotation speed on the spot welds strength [64].....21

Figure 2.17 (A) tools geometries: (a) cylindrical shoulder and pin (CC), (b) triangular shoulder and cylindrical pin (TC), (c) cylindrical shoulder and triangular pin (CT); (B) shear-tensile force as a function of rotational speed & tool geometry [67] 23

Figure 2.18 The effects of SiC nanoparticles of FSSW joints: (a) tension-shear force, (b) wear rates, (c) hardness profile [68] 24

Figure 2.19 (a) welding parameters effect on welds, (b) cross-section of weak weld strength (500 N), (c) cross-section of strong weld strength (1900 N) [77] 26

Figure 2.20 (A) cross nugget failure, (B) pull nugget failure [79] 28

Figure 2.21 (a) process profile and test conditions, (b) vertical load and temperature history [81].....29

Figure 2.22 A sample pulled to partial failure: (A) crack propagation along the ferritic region in the weld nugget, (B) close view of the zigzag, thin ferritic region [82].....30

Figure 2.23 ANOVA analyses results for shear-tensile force of (a) case 1 and (b) case 2 [88] 32

Figure 2.24 Taguchi optimized parameters for joints produced for (a) galvanized steel and (b) non-galvanized steel [89] 33

Figure 2.25 The deformed shape of the weld cross-section (a) practically and (b) theoretically [93].....34

Figure 2.26 Temperature verification: (a) thermocouple insertion points, (b) and (c) comparison of temperature history between model and experiments data [94] 34

Figure 2.27 The output of forge force vs time at rotational speeds (a) experimentally and (b) Theoretically [95] 35

Figure 2.28 Fatigue results for the FSSW welds under cyclic loading [51].....37

Figure 2.29 Fatigue results for the FSSW welds under cyclic loading [102].....37

Figure 2.30 Experimental data obtained from the fatigue test [103] 38

Figure 2.31 Schematic illustrations the IL-FSSW process 39

Figure 3.1 Schematic representation of the fixture of the IL-FSSW processing 43

Figure 3.2 The flat tip welding tool used in this study 43

Figure 3.3 The main effect plots of the welding parameters on the LSFF values 46

Figure 3.4 Lap shear-tensile test sample.....48

Figure 3.5 Schematic representation the top view of the rig designed to measure the axial load and torque of the welding tool 50

Figure 3.6 Temperature distribution measurement.....52

Figure 3.7 JEOL scanning electron microscope (SEM). 53

Figure 4.1 The IL-FSSW welds surface's appearance of the aluminum sheets 55

Figure 4.2 Top and cross section views of the weld's macroscopic appearance: (a) Al 6061-O and (b) Al 6061-T6 56

Figure 4.3 (a) Microstructures of the Al 6061-O joint: (b) SZ, (c) TMAZ, (d) HAZ, and (e) BM 57

Figure 4.4 (a) Microstructures of the Al 6061-T6 joint: (b) SZ, (c) TMAZ, (d) HAZ, and (e) BM 57

Figure 4.5 Hardness distribution of the Al 6061 welded joints in (a) T6 and (b) O tempers 58

Figure 4.6 (a) Microstructures of Al 2024-O joint: (b) SZ, (c) TMAZ, (d) HAZ, and (e) BM 60

Figure 4.7 (a) Microstructures of Al 2024-T3 joint: (b) SZ, (c) TMAZ, (d) HAZ, and (e) BM 60

Figure 4.8 Hardness distribution of the Al 2024 welded joints in (a) T3 and (b) O tempers 62

Figure 4.9 Microstructure images of the dissimilar Al 2024-O/Al 6061-O welds [129] 63

Figure 4.10 View of the hook formation and material distribution around the nugget zone in the dissimilar welds of Al 2024-O to Al 6061-O [131].....64

Figure 4.11 Hardness distribution of Al 2024/Al 6061 welded joints in (a) as received condition and (b) O tempers [129].....66

Figure 4.12 LSFF-displacement curves of the IL-FSSW welded joints.....67

Figure 4.13 The tensile curves of the workpieces before the IL-FSSW weld processing...68

Figure 4.14 Fracture surface after the shear-tensile of the Al 6061 welded sample in (a) T6 and (b) O tempers 70

Figure 4.15 Fracture morphologies of the Al 6061-O welded joint after the shear-tensile test 71

Figure 4.16 Fracture morphologies of the Al 6061-T6 welded joint after the shear-tensile test 72

Figure 4.17 Fracture surface after the shear-tensile test of Al 2024 welded sample in (a) T3 and (b) O tempers 73

Figure 4.18 Fracture morphologies of the Al 2024-O welded joint after the shear-tensile test 74

Figure 4.19 Fracture morphologies of the Al 2024-T3 welded joint after the shear-tensile test 75

Figure 4.20 Close-up views of the fracture region in the shear-tensile welded sample of Al 2024-O/Al 6061-O [129] 75

Figure 4.21 Fracture morphology appearances at selected points of failure regions [129].76

Figure 4.22 Fracture surface of the shear-tensile of the Al 2024-T3/Al 6061-T6 welded sample [131] 77

Figure 4.23 Fracture morphologies of the Al 2024-T3/Al 6061-T6 welded joint [131] 78

Figure 5.1 P_{max}-N_f curve of spot-welded specimens of Group 1. 80

Figure 5.2 Macroscopic appearance of fatigue-fractured specimens (Group 1, condition 1): (a) and (b) fracture surfaces at P_{max} = 2500 N observed on the upper and lower sheets (bottom and top view), (c) and (d) at P_{max} = 500 N, respectively, The loading direction vertical 81

Figure 5.3 Macroscopic appearance of fatigue-fractured specimens (Group 1, condition 2): (a), (b) fracture surfaces at P_{max} = 2500 N observed on the upper and lower sheets (bottom and top view), (c) and (d) at P_{max} = 500N, respectively. The loading direction is vertical ..82

Figure 5.4 SEM of fracture surfaces (Group 1, condition 1), upper sheet: (a) P_{max} = 500 N and $N_f = 1.44 \times 10^6$ and (b – e) magnified views at spots B–E in (a), respectively. The loading direction is horizontal 84

Figure 5.5 SEM of fracture surfaces (Group 1, condition 2), upper sheet: (a) P_{max} = 500 N and $N_f = 1.21 \times 10^6$ and (b – e) magnified views at spots B–E in (a), respectively. The loading direction is horizontal 85

Figure 5.6 Illustrations of the fatigue fracture morphology (Group 1). 86

Figure 5.7 P_{max}-N_f curve of spot-welded specimens of group 2 88

Figure 5.8 Macroscopic appearance of fatigue-fractured specimens (Group 2, condition 1) which observed on the upper and lower sheets (bottom and top view), respectively): (a) and (b) at P_{max} = 2000 N, (c) and (d) at P_{max} = 500 N. The loading direction is vertical 89

Figure 5.9 Macroscopic appearance of fatigue-fractured specimens (Group 2, condition 2) which observed on the upper and lower sheets (bottom and top view), respectively): (a) and (b) at P_{max} = 2500 N, (c) and (d) at P_{max} = 500 N. The loading direction is vertical 89

Figure 5.10 SEM of fracture surfaces (Group 2, condition 1), lower sheet: (a) P_{max} = 500 N and $N_f = 1.5 \times 10^5$ and (b – d) magnified views at spots B–D in (a), respectively. The loading direction is horizontal 90

Figure 5.11 SEM of fracture surfaces (Group 2, condition 2), lower sheet: (a) P_{max} = 500 N and $N_f = 9.4 \times 10^5$ and (b – d) magnified views at spots B–D in (a), respectively. The loading direction is horizontal 91

Figure 5.12 Illustrations of the fatigue fracture morphology (Group 2).....92

Figure 5.13 P_{max}-N_f curve of spot-welded specimens of Group 3 94

Figure 5.14 Macroscopic appearance of fatigue-fractured specimens (Group 3, condition 1): (a), (b) fracture surfaces at P_{max} = 2500N observed on the upper and lower sheets (bottom and top view), respectively, (c) P_{max} = 500N. The loading direction is horizontal 95

Figure 5.15 Macroscopic appearance of fatigue-fractured specimens (Group 3, condition 2): (a), (b) fracture surfaces at P_{max} = 2500 N observed on the upper and lower sheets (bottom and top view), respectively, (c) P_{max} = 500N. The loading direction is horizontal 96

Figure 5.16 SEM of fracture surfaces (Group 3, condition 1), lower sheet: (a) P_{max} = 500 N and $N_f = 1.7 \times 10^6$ and (b – d) magnified views at spots B, D in (a) and point C in (b), respectively 97

Figure 5.17 SEM of fracture surfaces (Group 3, condition 2), lower sheet: (a) P_{max} = 500 N and $N_f = 1.05 \times 10^6$ and (b – d) magnified views at spots B–D in (a), respectively 98

Figure 5.18 Illustrations of the fatigue fracture morphology (Group 3).....99

Figure 6.1 The geometry of the thermal model 104

Figure 6.2 The joint geometry of the mechanical model 105

Figure 6.3 Three dimensional coupled-field solid elements [146] 106

Figure 6.4 The mesh generated of IL-FSSW simulation, (a) the thermal model and (b) the mechanical model. 107

Figure 6.5 Typical hardness profiles of different welded samples 109

Figure 6.6 The stress-strain curves assumed for weld regions in the mechanical model for different samples.....110

Figure 6.7 Schematic diagram represent the boundary conditions of the thermal model..112

Figure 6.8 Lap-shear model, geometry and boundary conditions 113

Figure 6.9 (a) Schematic representation of welding set-up, (b) contact area between the tool and upper sheet 114

Figure 6.10 Temperature distribution during the weld processing of the similar Al 6061-T6 sheets, (feed=20mm/min and ω=1200 rpm) 118

Figure 6.11 Temperature distribution during the weld processing of the dissimilar Al 2024-T3 to Al 6061-T6 sheets, (feed=25mm/min, ω=1500 rpm).....118

Figure 6.12 Top view of the welded sheets of the IL-FSSW weld processing model (a) Al 6061-T6 sheets, (b) Al 2024-T3 to Al 6061-T6 sheets.....119

Figure 6.13 Temperature distribution through the weld processing of weld similar Al 6061-T6 sheets (a) ANSYS model results, (b) experimental results 120

Figure 6.14 Temperature distribution through the weld processing of dissimilar Al 2024-T3 to Al 6061-T6 sheets (a) ANSYS model results, (b) experimental results.....121

Figure 6.15 Failure development of Al 2024-O to Al 6061-O dissimilar weld under tensile loading: (a) simulation progress, (b) experimental progress 122

Figure 6.16 Stress state ratio of the weld sample: (a) Al 6061-T6 sheets, (b) Al 2024-T3 to Al 6061-T6 sheets.....122

Figure 6.17 Failure behavior during the simulation of shear-tensile test of different welds 123

Figure 6.18 LSFF-displacement curves of different welds: (a) experimental results, (b) ANSYS model results.....124

Figure 7.1 Welding tool: (a) conventional FSSW, (b) IL-FSSW. 126

Figure 7.2 Macroscopic views of the spot welds (a) IL-FSSW, (b) Conventional FSSW 127

Figure 7.3 Microscopic images of welds cross section (a) IL-FSSW, (b) conventional FSSW. 128

Figure 7.4 The Hv hardness profile of the IL-FSSW welded joint.....129

Figure 7.5 LSFF-displacement curves of the IL-FSSW and conventional FSSW spot welds 130

Figure 7.6 EDS analysis results of the IL-FSSW welded joint.....132

Figure 7.7 X-ray diffraction patterns of the IL-FSSW welds at the weld centerline.....133

Figure 7.8 Microstructure view of the IL-FSSW weld cross section: (a) morphology at low magnification; (b) interlocking of the intermetallic compound with the upper layer; (c) IL traces; (d) and (e) interlocking of the intermetallic compound with the upper layer; (f) primary dendrite of the intermetallic compounds at the upper sheet; (g) localized solidification defect in the transition region; (h) orientated flow of the intermetallic compounds through the grain boundaries of the aluminum crystals; (i) magnified view of the Cu zone. 135

Figure 7.9 Aluminum-copper binary phase diagram [166] 136

Figure 7.10 Fracture morphologies of Al/Pure Cu dissimilar joint weld by the IL-FSSW, and the load direction is vertical.....139

CHAPTER I

INTRODUCTION

1.1 Motivation

The variation of global necessity drives the industry into creating safer and better performing machine components for both producers and customers. This has led to an increase in the competitive advantage in the transport sector and thus, weight reduction of the products is now being pursued. A multi-material joining design takes advantage of the material with the required properties for each part of the product. In automotive and aerospace industries and due to fuel economy and environmental issues, weight reduction has become a very important feature. Light-weight alloys became the important materials to replace heavy materials, which required new joining processes to be able to produce similar and dissimilar joints of high quality. The 6xxx and 2xxx series of aluminum (Al) alloys are generally classified as hard-weldability alloys. As a matter of fact, a lot of difficulties are associated with the joint processes of these kinds of alloys, which are mainly related to the presence of a tenacious oxide layer, high thermal conductivity, high coefficient of thermal expansion, solidification shrinkage, and above all, the high solubility of hydrogen and other gases during the molten state [1]. These alloys are widely used in aerospace industries which need to produce high strength fatigue and fracture resistance joints. Thus, the joining of these alloys by using fusion welding processes was undesirable [2,3].

In industrial applications, joining dissimilar materials with completely different mechanical and physical properties promotes the use of such joints; especially in the electrical components field. Recently, interest in technologies capable of producing dissimilar copper (Cu) to Al joints has strongly increased in order to obtain good mechanical and electrical properties. The weldability of pure copper is influenced by high heat conductivity, the tendency to absorb gas (oxygen, hydrogen, and carbon dioxide, etc.), major thermal expansion, and the transition from liquid to solid and vice versa without a melting interval (solidifying at the melting point). Heat dissipation at 1000 ºC is approximately 10 to 15 times that of steel, so it is normally necessary to preheat the workpiece [4]. Producing a high-quality dissimilar joint of the Al-Cu presents a unique welding problem with the common welding process because of its combined properties such as a high melting temperature and high thermal conductivity of copper when compared to aluminum. Therefore, the welding of dissimilar Al to Cu alloys has become a challenging technique, which needs to be developed [5,6]. Consequently, devising other welding methods is imperative. Subsequently, the welding processes based on friction and stirring, whether to produce linear welds joints (i.e., friction stir welding (FSW)) or spot welds (i.e., friction stir spot welding (FSSW)), have gained considerable attention as explained in detail by Mishra [2] and Wang [7]. However, FSSW is constrained by the problems related to the keyhole, which usually forms on the welded surfaces [8].

In recent years, researchers have attempted to address the keyhole defect because of its negative effects on tensile, shear, and fatigue strength [9]. The keyhole acts as a stress concentration region and reduces the thickness of the weld spot, thereby weakening the weld strength and reducing its mechanical properties. Some researchers have focused on the removal of the pins from welding tools. Other researchers have directed their

efforts toward the refilling of the keyholes to eliminate their negative effects on the weld properties.

It has been noted that the common goal of the previous studies has been to remove the keyhole in the FSSW welds; most of them have focused on removing the keyhole after it has been created. Regardless of the benefits of the methods currently existing to solve this problem, they include some limitations. Most of these methods require a specialist welding tool or machine, which tends to increase the complexity, the difficulty with the equipment, the cost, and the time required to complete the welding process [10,11].

Additionally, there has yet to be an investigation on the avoidance of the keyhole appearance by using a specific method. The current work aimed to eliminate the keyhole appearance by developing the FSSW process through adding an IL part and changing the welding tool to a painless, flat tool. This process is called the Intermediate Layer FSSW (IL-FSSW). The workpiece's materials were sheets of 6061 and 2024 aluminum alloy sheets in treated and annealed thermal conditions, in addition to the pure Cu that is used to fabricate the dissimilar Al to Cu joints.

1.2 Research Objectives

The main objective of this study was to investigate the mechanical behavior of similar and dissimilar spot joints welded of aluminum and copper alloys using a development FSSW process (IL-FSSW). This goal was achieved through the following:

- Designing an effective experimental setup with different configurations to conduct IL-FSSW and conventional FSSW processing.

- Investigating the effect of using the IL part on the mechanical properties of IL-FSSW fabricated welds when compared with that of the welds fabricated by the conventional FSSW process.
- Investigating the influence of the welding parameters on the strength of the IL-FSSW welds and enhancing it by using the design of the experiments (DOE) method.
- Developing finite element models suggested to predict the temperature distribution and weld strength during the welding process and compare the results with the data collected experimentally.
- Carrying out an experiment to measure the axial force and torque of the welding tool under various parameters.
- Evaluating the behavior of the spot-welded joints under fatigue loading will be studied for the aluminum welded specimens. In addition, investigating the heat treatment effects on fatigue life and fracture mechanisms of the welded samples.

1.3 Work Summary

In the current study, friction stir spot welding is used for the synthesis of the similar and dissimilar metallic joints of both the aluminum and copper alloys utilized by the IL part as a novel addition to the conventional FSSW process. Shear-tensile strength enhancement was observed significantly for the Al 2024/Al 6061 IL-FSSW welds when compared with the results from the conventional FSSW. All of the remaining welded samples were conducted with the AWS requirements for the spot welds' tensile quality, except for the similar welds of the Al 2024-T3.

Fatigue tests were employed for the as-received and annealed heat-treated workpieces of the IL-FSSW aluminum welds at ambient temperatures to investigate the effect of the heat treatments on the fatigue life behavior. In the case of the Al 2024 alloy, a notable improvement in the fatigue life was observed in the annealed samples than in the as-received samples.

For dissimilar aluminum/copper welds, in order to see the effect of IL part on the weld nugget, microstructure of samples was observed for weld cross section, scanning electron microscope (SEM), XRD, and EDS examinations results were analyzed. Metallic flow patterns of aluminum in copper and intermetallic compounds with a hardness reaching 575 Hv were observed. Fracture surface observations hinted at the distribution of intermetallic compound phases along the matching surfaces of the welded sheets.

CHAPTER II

BACKGROUND AND LITERATURE REVIEW

2.1 Friction Stir Welding (FSW)

Friction Stir Welding (FSW) is a revolutionary solid-state welding technique invented at The Welding Institute (TWI) in 1991 [2,12]. FSW is an energy-efficient, environmentally-friendly, and multipurpose joining technique that has been classified as one of the most important achievements in the field of joining aluminum alloys [5]. FSW has been widely used in a wide range of applications such as space, aircraft, marine, fuel tanks, and the food storage industry. It is also used to weld Mg alloys, Cu alloys, Ti alloys and steel [13,14].

In FSW, the non-consumable tool serves two primary functions: a) heating the workpiece and b) helping in material movement to produce the joint. The heating of the workpiece is achieved by the friction and the plastic deformation of the workpiece. Figure 2.1 shows a schematic view of the FSW process employed in producing a butt-welded joint. The softened material around the pin moves from the front to the back as a result of the rotational and translational movements of the tool. As a result of this process, a joint is produced in a solid-state [2,15]. No melting occurs during the FSW process, and the temperature of the welded plates is typically about 80-90% of the melting temperature so that better mechanical properties and fewer weld defects of the weld zone are produced when compared with conventional arc welding [16–18].

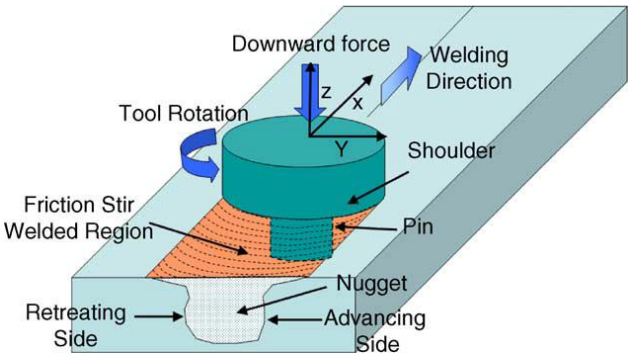

Figure 2.1 Schematic representation of the FSW [2]

Four distinct zones could be recognized in FSW; the base material (BM), the heat affected zone (HAZ), the thermomechanical and heat affected zone (TMAZ), and the nugget or stirring zone (SZ), as shown in Figure 2.2. The SZ consists of fine equiaxed grains smaller than those of the base BM. The TMAZ comprises grains similar in size to that of the base material with a bent morphology due to the induced deformation of the region adjacent to the nugget as a result of the stirring action of the tool [12,19]. The main variables of the FSW process are the welding traverse speed, the tool rotational speed, the tilt angle of the tool, and the tool design [20,21].

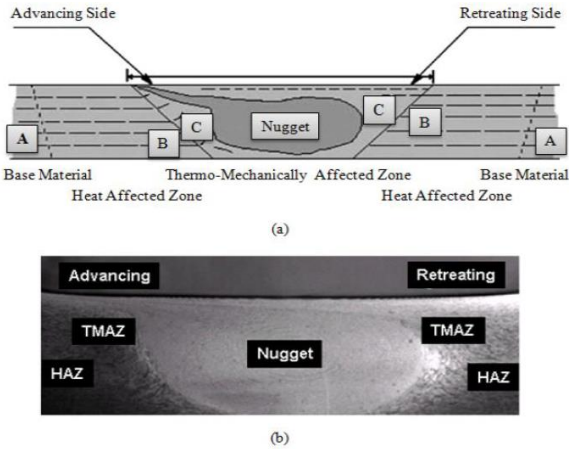

Figure 2.2 (a) Schematic diagram of microstructural zones in friction stir welds of aluminum, (b) micrograph showing various micro-structural zones [22]

2.2 *Friction Stir Spot Welding (FSSW)*

The FSSW process is a development of the "linear" FSW, it is patented by the Mazda Motor Corporation and is used for the production of new RX-8 sports car [23]. FSSW can be a more efficient (significant energy and cost savings) alternate process to electric resistance spot welding, TIG spot welding, and Laser spot welding. Reduced energy consumption and capital costs of approximately 85% and 50%, respectively, have been reported when resistance spot welding (RSW) is replaced by FSSW [24]. In the automotive industries, FSSW has generated enormous interest for directing the replacement of RSW of Al and Cu alloys as well as having better performance than mechanical joining methods such as fastening [25].

In FSSW, a lap-welded spot joint is created without the bulk melting of the workpiece. During this process, the non-consumable rotating tool combined with the pin and shoulder is plunged into the two workpieces to be joined, while the rigid anvil supports the downward force. Figure 2.3 shows the steps of the FSSW process.

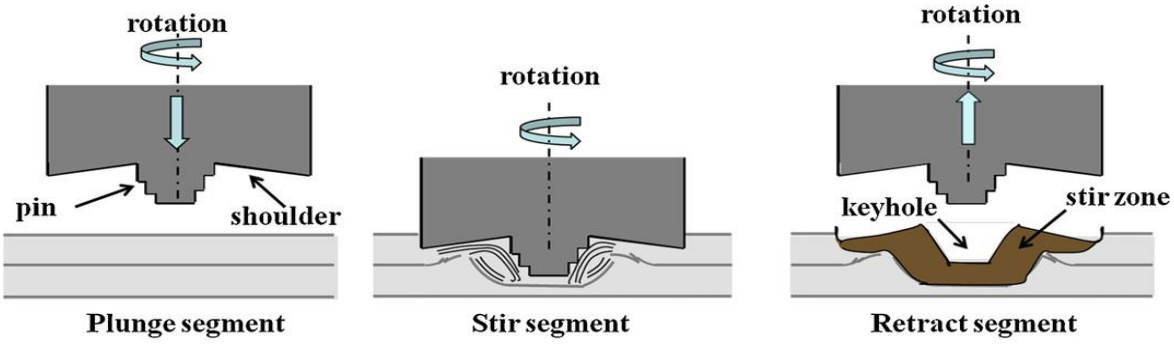

Figure 2.3 Schematic representation of the steps in the FSSW process [26]

The FSSW process starts with the tool rotating at a high angular speed. Then, the tool is forced into the workpieces until the tool shoulder contacts the top surface of the upper workpiece to form a weld spot. The plunging movement of the tool causes the expelling of the materials. After plunging, the stirring stage starts when the tool reaches a predetermined depth. At this stage, the tool keeps rotating in the workpieces. The frictional heat is generated in the plunging and stirring stages and thus, the materials adjacent to the tool are heated, softened, and mixed in the stirring stage, where a solid-state joint will be formed. When acceptable bonding is obtained, the tool is retracted from the workpieces. This welding process involves the following advantages [27,28]:

1. It is a fast process since the cycle times are within a few seconds.
2. There is no need for material melting during the process, which cause high joint strength without porosity, cracks, and contamination.
3. Lower energy consumption. The only energy consumed is the electricity needed to rotate and drive the tool when compared to RSW or fusion welding.
4. Lower equipment investment, approximate 40% reduction in equipment investment when compared to RSW.
5. No preparation and consumables are needed such as surface clean, drilling, rivets or bolts. No hazardous emissions and environmentally friendly.

The limitations of FSSW are the following [29]:

1. Forming of a void in the middle of the spot weld surface after welding, which is called the Keyhole defect [28].

2. Workpieces must be rigidly clamped, and a backing bar is required.

2.2.1 FSSW Versus Other Single Point Joining Processes

The FSSW can be used in place of Resistance Spot Welding (RSW), riveting, clinching, or any other single point joining process in many applications. RSW is one of the most common electrical spot-welding processes, where the electrodes of the copper are equipped on a servo-electric mechanical machine to metal sheets (workpieces) in between. This process is used in a wide range of applications that need spot welded joints. The basic RSW setup is shown in Figure 2.4. The limitations of the RSW process are; the cost of RSW equipment is high, skilled technicians are needed for checks and maintenance, cleaning surfaces of the metals is needed, and thick plates are not easy to weld [30].

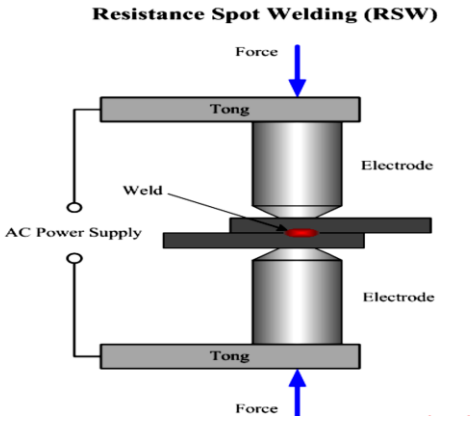

Figure 2.4 Schematic of the resistance spot welding [30]

The Resistance Element Welding (REW) process combines both electrical and mechanical joining procedures, a spot joint is created between an auxiliary element (weld

rivet), and the lower sheet, as shown in Figure 2.5. After a hole is created as a pre-process, the rivet is inserted into the hole. The upper electrode is moved down onto the rivet. An electric current applied cause a weld nugget formation in the contact zone and creates the joint. The limitations of the REW process are similar to that in the RSW process [31].

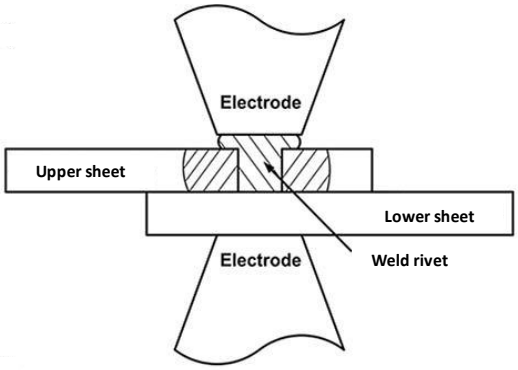

Figure 2.5 Schematic representation the resistance element welding [31]

The FSSW of aluminum has several advantages when compared to the RSW and REW processes; solidification, and liquation cracking in addition to porosity, which are typical in RSW, are eliminated with FSSW due to the solid-state nature of this process [32].

Solid-state welding methods, which are used to join similar and dissimilar metals are attracting a lot of interest because they avoid melting and re-solidification problems, they also appropriate for welding metal combinations that have large differences in melting temperature, such as aluminum and steel [33]. Self-piercing riveting and mechanical clinching are a similar mechanism point joining processes. In self-piercing riveting, the sheets are pierced by a tubular rivet with no need to pre-drilling, as shown in Figure 2.6. The weld rivet is driven through the upper sheet and the skirt of the rivet (the bottom part of the

rivet) and expands to create an interlock for clamping the sheets together. The die and rivet need to be designed according the interlock dimensions. The strength of the joints is dependent on the interlock fixability [34].

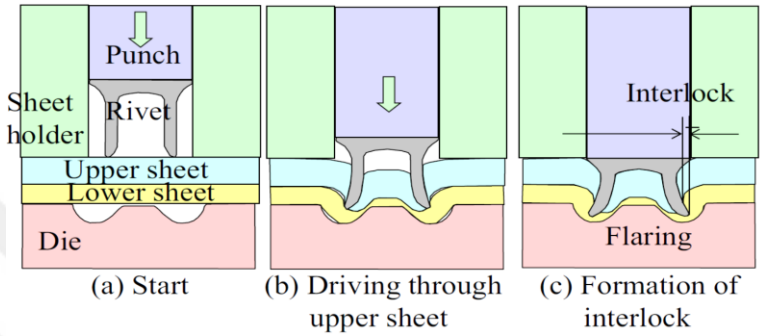

Figure 2.6 Schematic of the joining process of self-piercing riveting [34]

In the mechanical clinching operation, a mechanical interlock is formed by compressing the punch on the sheets into the die with a ring grooved cavity without using a weld rivet, as shown in Figure 2.7.

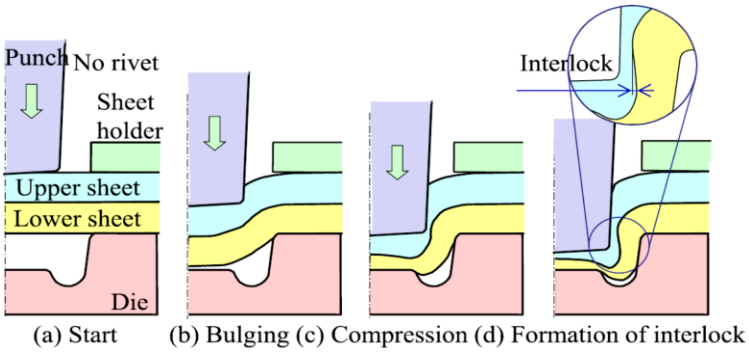

Figure 2.7 Schematic of the joining process of mechanical clinching [34]

The limitations of these processes are; the punch and die needed to form the joint, per-processing is needed, and the weld does not have a flat appearance with a bulge (self-piercing) or cavity (mechanical clinching) in the joint spot [34].

2.2.2 Effect of FSSW Parameters on Welding Quality

The main independent variables used to control the FSSW process are; the tool rotational speed, the plunging feed rate, the tool design, the dwell time, and the plunging depth. These variables strongly affect the generated heat and temperature distribution. Using the appropriate welding parameters leads to a large bonded area, which plays a significant role regarding the fabricated joints' quality [35,36]. However, none of the researchers has settled on an optimal value of the FSSW parameters in general but it depends on each individual case-study.

Sakiyama et al. [37] reported that the rotational speed was the main influencing factor on the shear-tensile strength of the FSSW welds of the coated steel to 6xxx series aluminum alloy sheets. The joint strength was increased from 2.5 to 4.5 kN by increasing the tool rotational speed from 1000 to 3000 rpm. Choi et al. [38] investigated the effect of the rotational speed on the mechanical properties of similar sheets of Al 5454 alloy welded by FSSW. The result showed an inverse relationship between the rotational speed and the joint strength, whereas a positive relationship was found between the rotational speed and the hardness values, as shown in Figure 2.8.

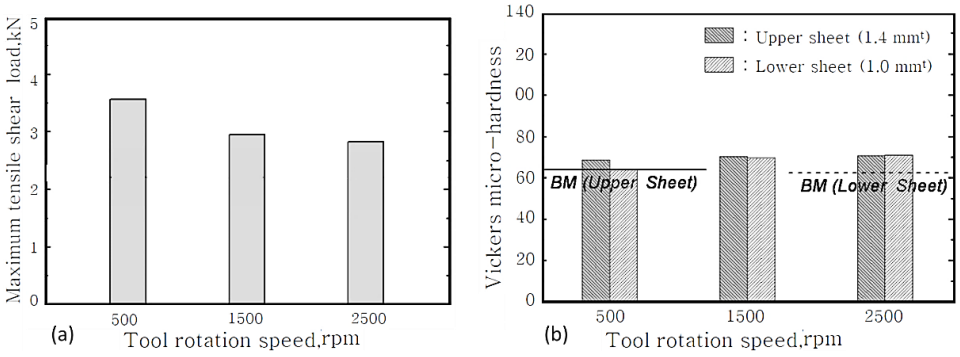

Figure 2.8 Effect of the rotational speed on the FSSW joints properties [38]

The effect of the process parameters on the FSSW welds strength of 3 mm thickness sheets of 2A12-T4 aluminum alloy was studied by Liu et al. [39]. Ranges of 400~1200 rpm, 5~40 mm/min plunging feed rate, and 0.1~0.5 mm plunging depth were used. The results showed that the shear-tensile failure load was directly proportional with both the rotation speed and the plunging depth, but it was inversely proportional to the plunging feed rate.

The welding feed rate effect was investigated by Elangovan and Balasubramanian for the Al 2219 alloy [40]. The experiments revealed that the tensile and hardness values were improved when the feed rate was increased from 0.37 to 0.76 mm/s, and then the properties deteriorated when the feed rate increased from 0.76 to 1.25 mm/s. Tier et al. [41] studied the effects of the feed rate on the refilled FSSW welded joints of 1.5 mm thick Al 5042 alloy. The results showed the shear-tensile failure force was affected by the variations in the feed rate from 0.48 to 1.87 mm/s, but the relationship was not linear.

In terms of the plunging depth effect on the strength of FSSW welds, Merzoug et al. [42] reported that the increase of the plunging depth tends to improve the shear-tensile strength of the FSSW welds of the Al 6060 alloy, but at certain limits only. Thereafter, the strength is negatively affected. Yuan et al. [43] reported that high-plunging reduced the effective thickness of the upper sheet in a welding zone is reduced due to the increases in a keyhole volume of 1 mm thick sheets of Al 6061 alloy. The experiments using two types of tool (conventional pin (CP) and off-center feature (OC)) showed an increase of the joints' strength with the increase in the shoulder plunging depth up to a certain point before decreasing again, Figure 2.9.

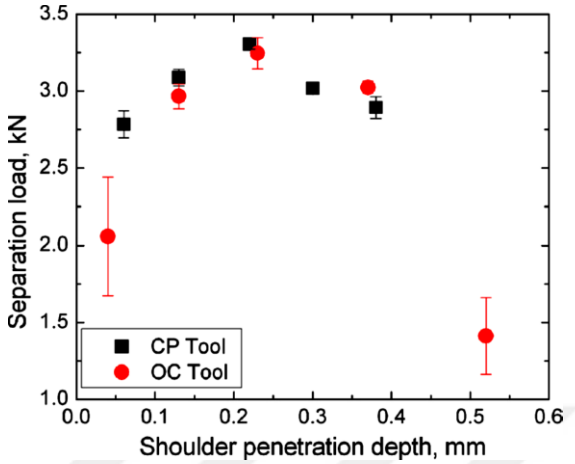

Figure 2.9 Shear separation load as a function of the shoulder penetration depth [43]

2.2.3 The Keyhole Problem of FSSW

Major automakers, such as Mazda and Kawasaki, deploy FSSW in their car production because of its superiority over its predecessor (RSW) [44–46]. However, the keyhole, which usually forms on the welded surfaces at the center of the weld after tool retraction (Figure 2.3), is considered as a critical issue that causes a stress concentration region and reduces the thickness of the upper sheet in the weld nugget, which in turn causes a decrease in the active welding area of the spot weld. Furthermore, it is hard to reach the keyhole areas in cases of body painting. Therefore, corrosion in the keyhole is likely to occur [8].

In recent years, researchers have attempted to address the keyhole defect because of its negative effect on the mechanical properties of the welds [47]. Many publications about refilling or cancelling the keyhole defect problem approaches have been proposed in the literature. Refill FSSW (RFSSW) technology was developed by GKSS Forschungszentrum [48,49] of Germany to fill the keyhole. As shown in Figure 2.10, in the first step, the clamping

ring initially fixes the sheets against a backing plate on the bottom, and the sleeve and pin start rotating and move in the reverse direction to each other. The sleeve plunges into the top surface. The frictional heat plasticizes the materials to occupy the existing space which is formed between the sleeve and the pin easily. In the next step, the sleeve and the pin retract back to the surface of the plate and this pushes the accumulated material to completely refill the keyhole. In the final step, the whole welding tool withdraws leaving a flat surface without any keyhole.

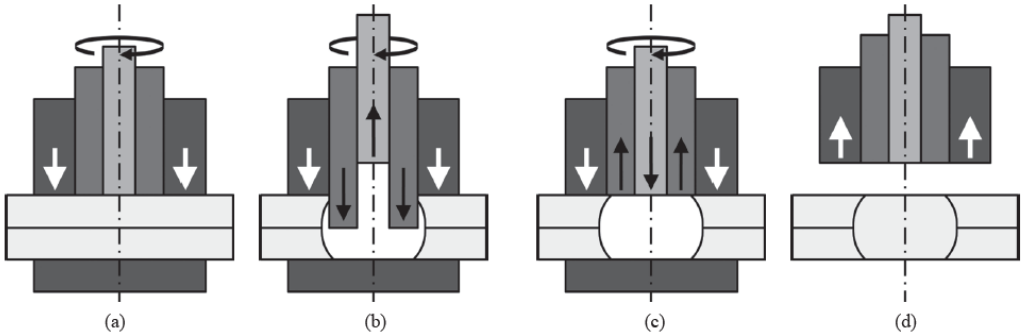

Figure 2.10 Schematic illustration of the RFSSW process [48].

Bozkurt et al. [50] developed a welding method called the pinless FSSW to remove keyholes by using different flat-tip tools with grooves were considered in the material-mixing process to improve the joints mechanical properties. Uematsu et al. [51] studied keyhole refilling as a post-treatment of the welds of the Al–Mg–Si alloy after the FSSW process. Accordingly, the failure force was raised from 2654 N to 3458 N. Sun et al. addressed the keyhole problem through a two-step welding process. They employed similar alloys of the Al 6061 and Al 5052 [52], and dissimilar alloys of the Al 6061 and mild steel [53]. This process is shown in Figure 2.11. In the first stage, a uniquely designed back plate, which contained a rounded dent is used. After the FSSW, a keyhole is formed and causes the flow

of the materials inside the dent. In the second stage, a flat back plate and a pinless tool are used to remove the keyhole successfully.

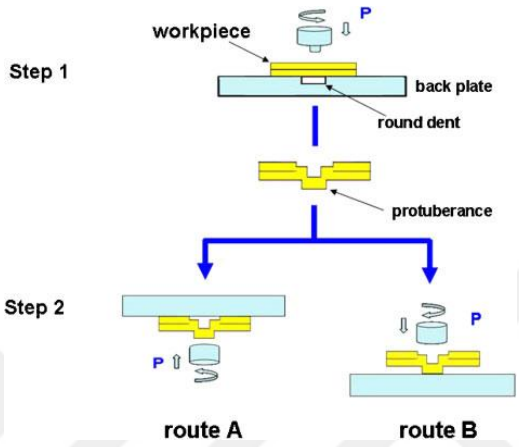

Figure 2.11 Schematic representation of the FSSW developed [52]

Chen et al. [54] reduced the diameter of the original keyhole of the Al 6061/TRIP steel welds, through replacing the welding tool with another that has a smaller pin diameter and offsets it from the center of the weld as shown in Figure 2.12. The joint strength of the treated welds increased about 56%.

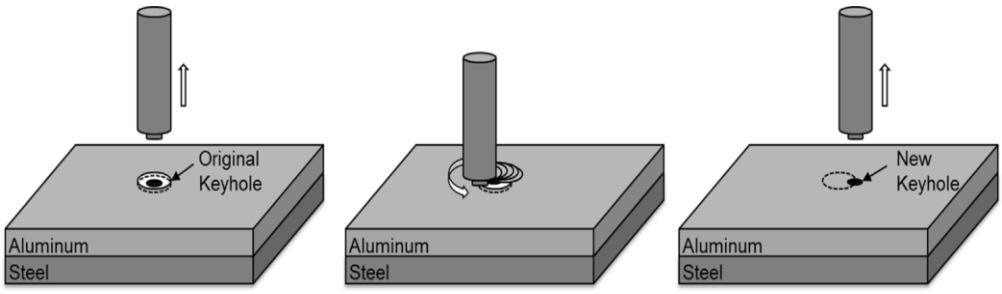

Figure 2.12 Schematic of the keyhole refilled FSSW process illustration [54]

Tozaki et al. [55] utilized a new development tool has a scroll groove to force out the material in a vertical direction instead of the conventional FSSW tool. The results revealed

that the new tool gives similar or better results in comparison with the typical FSSW tool with a shoulder and pin. The schematic of the suggested tool is shown in Figure 2.13.

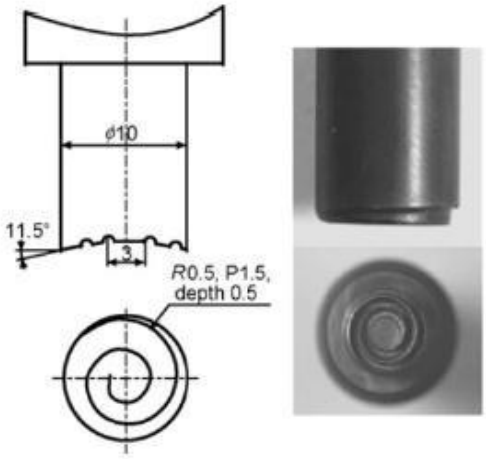

Figure 2.13 The dimensions and tool design developed [55]

2.3 Weldability of Al 6061 and Al 2024 Alloys, and FSSW Applications

Aluminum and its alloys are used in a wide variety of manufacturing industry. The low density, good thermal conductivity, high corrosion resistance, fabricability, good mechanical properties, and high strength/weight ratio are all properties found in aluminum alloys, which are the most economical and attractive materials for automotive applications [56].

The high thermal coefficient of aluminum together with the protective layer of oxide makes it tricky to weld with traditional electrical welding processes. The oxide layer should break and be removed, and the heating must be rapid during the process in order to avoid the unnecessary thermal expansion in the products. With friction stir welding, these problems

can typically be avoided. Figure 2.14 shows the weldability of various wrought aluminum alloys by fusion and friction welding processes [57,58].

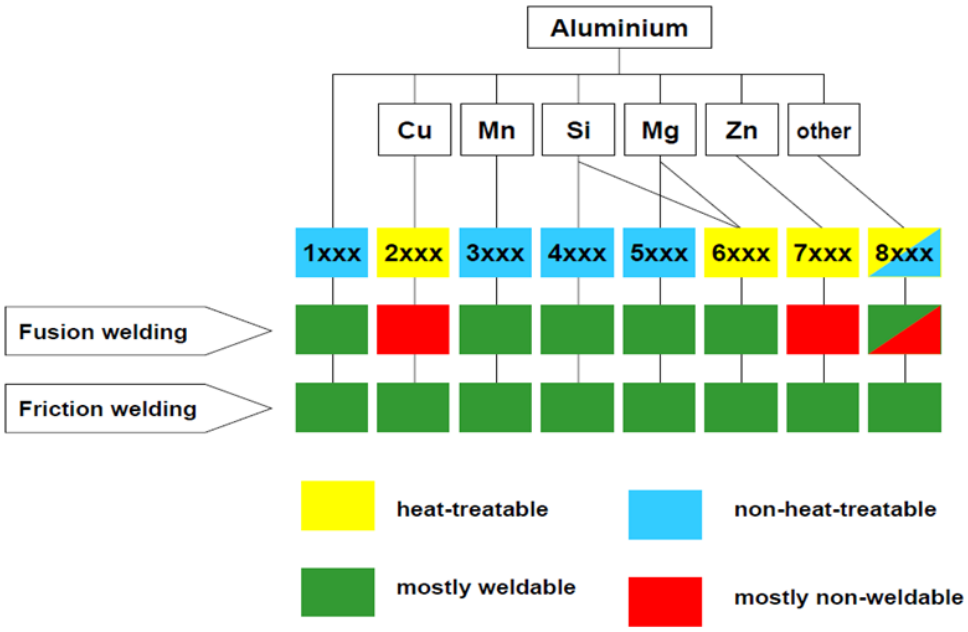

Figure 2.14 Weldability of various wrought aluminum alloys [57,58]

Friction stir welding processes can be used as solid-state welding to join aluminum sheets or plates without any filler wire or shielding gases needed. Up to date, the materials that have been successfully friction stir welded were all aluminum, copper, magnesium, lead, zinc, and their alloys [59].

The 6061 series of aluminum alloys contain silicon and magnesium, making them a heat treatable alloy. This alloy is widely used as a medium-strength structural alloy. The weldability, corrosion resistance, and formability make this alloy the best candidate material for automobile body sheet applications [60,61]. The Al 6061 alloy is well-known for its superior mechanical properties, but the primary reasons for selecting the Al 6061 are its

acceptable mechanical properties coupled with its relative ease with which it can be cast, extruded, rolled, and machined, etc. [62]. The standardized products of the Al 6061 include sheets, plates, foils, rods, bars, wires, tubes, pipes, and structural forms.

Tashkandi et al. [63] used the Al 6061 alloy of 3 mm thick to investigate the of the welding parameter's effects on the lap-shear force of the spot welds equipped by the FSSW process. The parameters analyzed were rotational speed, dwell time, pin, and shoulder sizes of the welding tool. They found that the lap-shear force increases with an increase in the welding parameters within a limited value before the decreases with a further increase as shown in Figure 2.15. The maximum lap-shear force recorded was 2900 N.

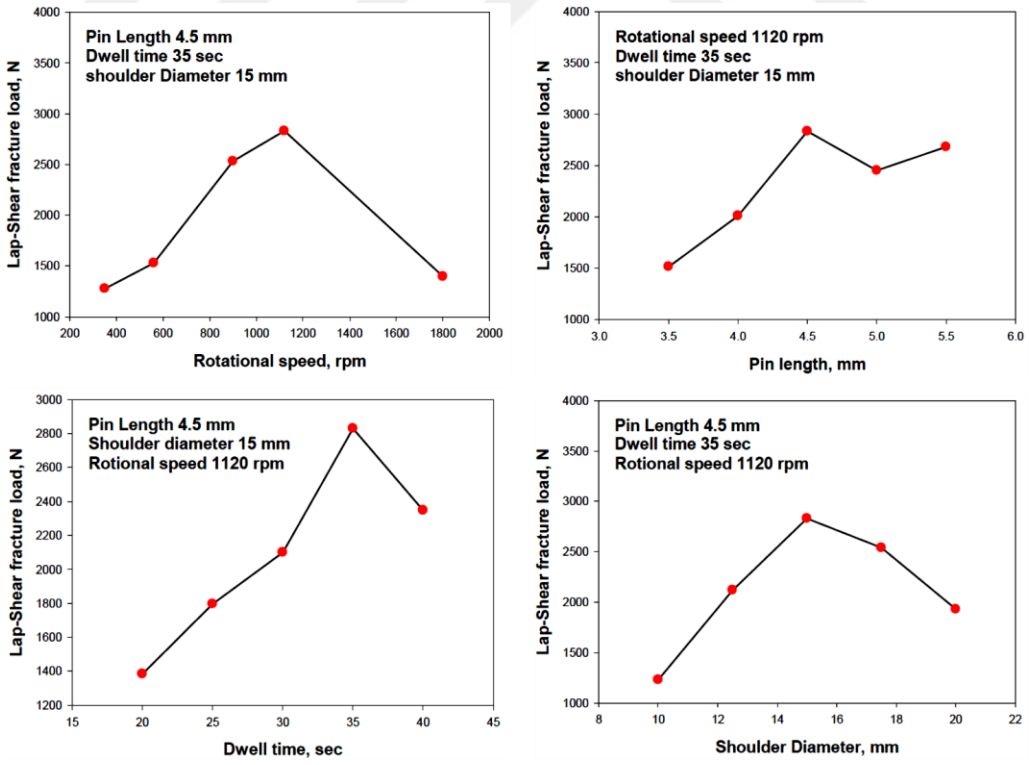

Figure 2.15 Lap-shear force for different welding parameters [63]

Cox et al. [64] canvassed the different welding parameters effect on similar sheets of 1 mm thickness Al 6061-T6 alloy used in FSSW. The effect of the two types of welding tool, both with and without a pin (flat), were investigated regarding the mechanical properties of the welds. They identified three distinct failure modes when the weld is placed under tensile loading; shear modes, mixed modes, and nugget pullout mode. The relationship between the pin length and the tool rotational speed on the tensile strength is shown in Figure 2.16. Unlike most publications in this regard, it is evident that the weld strength decreases linearly with the increasing rotation speed.

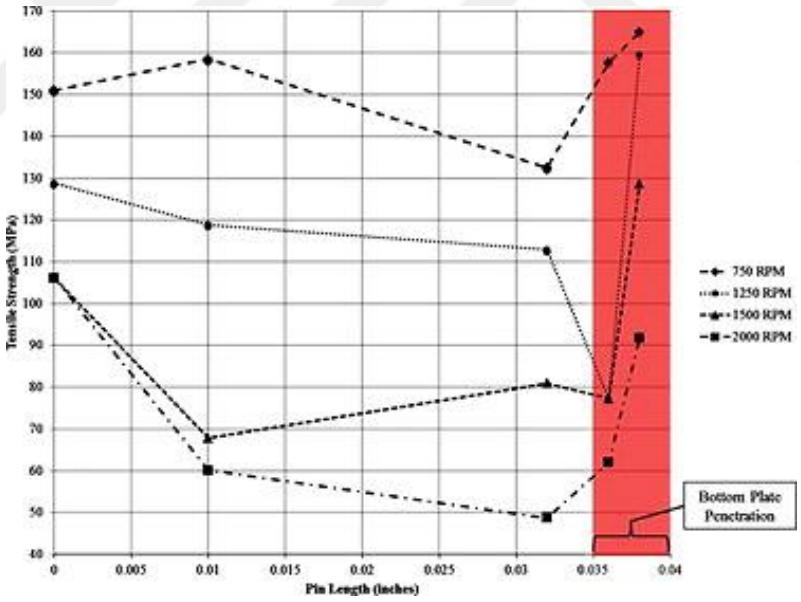

Figure 2.16 Effect of pin length and rotation speed on the spot welds strength [64]

Chi-Sung et al. [65] studied the material mixing in the SZ of 3 mm thick similar Al 6061-T6 alloy by using an electron probe micro analyzer (EPMA) and an electron back scattered diffraction (EBSD). The mechanical properties of the FSSW welds were

investigated as a function of the different process parameters. The maximum lap-shear force was 3618.7 N at a 0.92 mm displacement.

The 2024 series of aluminum alloys are also heat treatable, and they possess good combinations of toughness and high strength, especially at high temperatures. This series is not resistant to atmospheric corrosion, it is usually painted or cladded in such exposures. Because of the high strength of this series, it is mainly used for truck bodies and aircraft applications. Because of the slightly hard weldability of these types of aluminum alloys, the riveting joining process is usually used in its applications [59].

Abbass [66] investigated the effect of the aging time on the mechanical properties of welds made by 1.5 mm sheets of Al 2024 alloy. FSSW was carried out using the optimum conditions of the welding parameters via a drilling machine. The solution heat treatment and aging at 190 ºC for different times were performed. It was found that the maximum shear-tensile force and hardness values were at a 190 ºC aging temperature and for 5hr and 3hr respectively as shown in Table 2.1.

Table 2.1 Aging effect on weld strength and hardness of Al 2024 [66]

Condition	Aging time (hr)	Shear-tensile force (N)	Hardness Hv (Kg/mm^2)
As weld at 750 rpm and 60 s	-	2400	80.6
S.T. at 520 For 30 min and aging at 190 °C	S.T.	3300	84
	1	3350	92
	3	3400	116
	5	3600	106
	7	2700	100
	10	2600	95
	15	2300	87

Paidar et al. [67] performed FSSW on 2024-T3 Al alloy to study the effect of different pin and shoulder geometry on welded samples characterization and mechanical properties. The process was conducted at a constant dwell time of 5 s and shoulder plunging depth of 0.3 mm. The rotational speed range was 630–1600 rpm. The observations revealed that the area of SZ changed with each shape of the tool, which led to changes in the mechanical properties of the joints as seen in Figure 2.17.

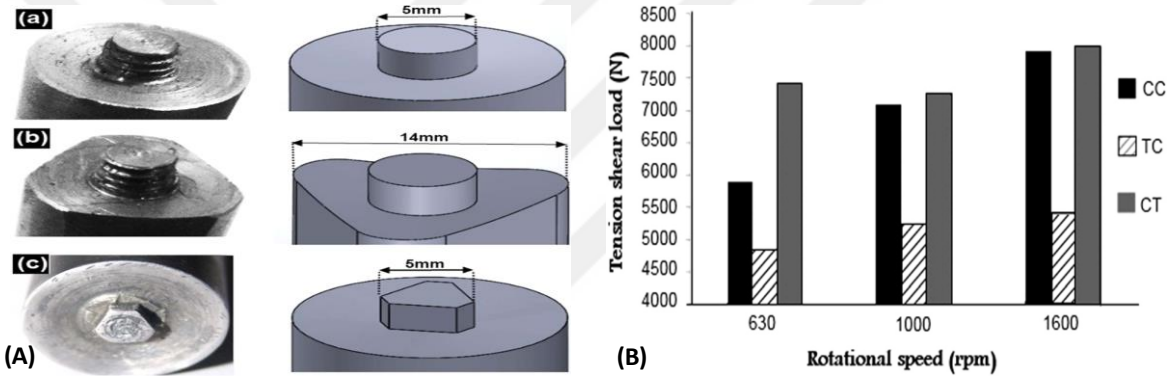

Figure 2.17 (A) tools geometries: (a) cylindrical shoulder and pin (CC), (b) triangular shoulder and cylindrical pin (TC), (c) cylindrical shoulder and triangular pin (CT); (B) shear-tensile force as a function of rotational speed & tool geometry [67]

The silicon carbide (SiC) nanoparticle effects on the metallurgical and mechanical properties of the Al 2024-T3 spot welds made of 1.5 mm thickness sheets were discussed by Paidar and Sarab [68]. The FSSW process was conducted at 1000 rpm. The results showed that the shear-tensile force and wear resistance increased with the addition of the SiC nanoparticles, which was attributed to the nanoparticles role as barriers disallowing the grain growth in the SZ, Figure 2.18. Sergio et al. [69] studied the welds fabricated from Al 2024-T3 alloy (rolled sheets) by using the FSSW process. The Design of Experiment and Analysis of Variance statistical methods were employed to evaluate the joint shear strength under static

loading. Sound joints with evaluated shear strength were achieved and the influence of the main process parameters on the joint strength was investigated.

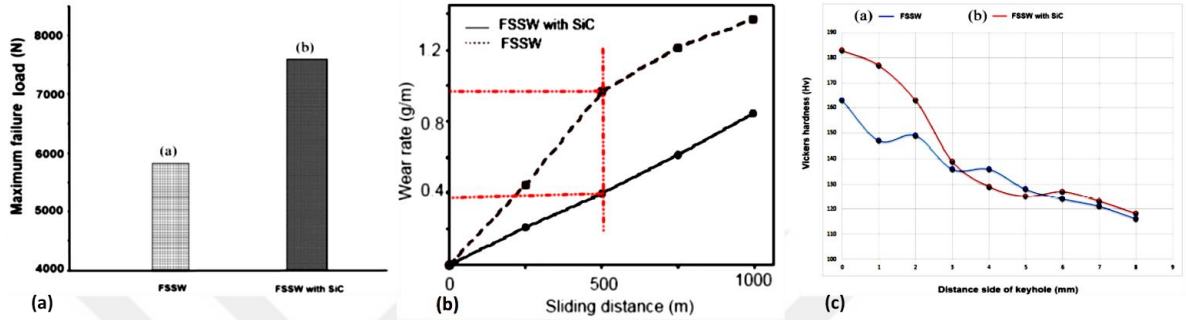

Figure 2.18 The effects of SiC nanoparticles of FSSW joints: (a) tension-shear force, (b) wear rates, (c) hardness profile [68]

Dissimilar joining between Al 6061 and Al 2024 alloys is considered as a challenging one when compared to similar welds due to the variation in the chemical composition and mechanical properties of these alloys. To our knowledge, no efforts have been made to produce dissimilar spot welds between Al 6061 to Al 2024 alloys by using the FSSW process, and only one case had the same joint pair as in this study. Handyside et al. [70] used an industrial robot with a "C-Frame" end to fabricate spot welds on Al 2024-T3 (0.81 mm) / Al 6061-T6 (1.6 mm) using FSSW. The pin temperature and anvil sticking issues are addressed after optimizing the process parameters and tool geometry. The maximum joints' shear force was found to be 1.92 kN after the experimental tests.

2.4 Weldability of Aluminum to Copper Alloys, and FSSW Applications

Copper and its alloys are widely used in a variety of products because they have excellent thermal and electrical conductivities, exhibit good strength and formability, have

outstanding corrosion and fatigue resistance, and are nonmagnetic. Pure copper, in an unalloyed state provides high thermal and electrical conductivity, it is soft and has excellent corrosion resistance. There are several grades of unalloyed copper (pure copper), which vary in the amount of impurities they contain. Oxygen-free coppers are used specifically in applications requiring exceptional ductility and high conductivity. It is used extensively in electrical applications [71]. The joining processes between aluminum and pure copper promoted the use of such joints in industrial applications, especially in regard to the aspects of the electrical components [72,73].

Recently, the interest in aluminum/copper joints has been related to future electrical vehicles. The electrical vehicles' batteries require the connections of individual cells. Since the two electrodes of the cell are based on aluminum and copper foil current collectors, many aluminum/copper joints are required for this application [74]. Due to the difference in the chemical and mechanical properties between these two metals, the high-quality aluminum/copper dissimilar joint is hard to produce by fusion welding techniques due to the difference in the melting points and crack formation [75]. While conducting this investigation, it was noticed that not many studies are available in the literature on the welding of aluminum to copper utilizing FSSW process. Özdemir et al. [76] have successfully produced welds of a 3 mm thickness Al 1050 to pure Cu via FSSW. They used three different plunging depths 2.8, 4, and 5 mm, and the welding tool consisted of 20 mm and 5 mm diameters of the shoulder and pin, respectively. The other parameters were a 1600 rpm rotation speed and a 10 s dwell time. The spot welds produced were free of defects with fine grains on the weld nugget close to the Al/Cu interface. Moreover, the EDS analyses

revealed the formation of hard intermetallic compounds of the AlCu, Al_2Cu and Al_4Cu_9 formed within the nugget. The results of the shear-tensile test displayed that a 2.8 mm plunging depth formed poor joint strength (1.85 kN) whereas in the case of the 4 mm plunging depth, the weld strength values were the highest (3.95 kN) [76].

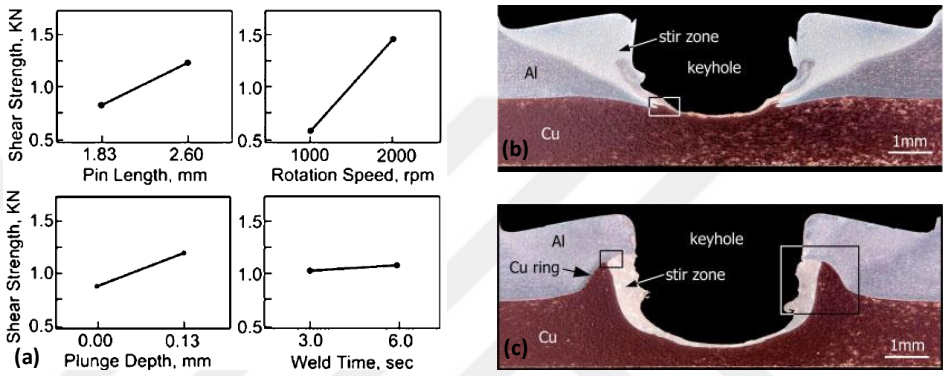

Figure 2.19 (a) welding parameters effect on welds, (b) cross-section of weak weld strength (500 N), (c) cross-section of strong weld strength (1900 N) [77]

Heideman et al. [77] studied the welds of the FSSW process made from 1.5 mm thickness oxygen free pure copper to the Al 6061-T6 alloy. They utilized the design of an experiment (DOE) to determine the impact of the welding parameters on the strength of the welds. As constant parameters, they used a tool with a 4 mm diameter of a threaded pin made of a pre-hardened H13 tool steel, with a shoulder of a 10 mm diameter. The variables were zero and 0.13 mm plunging depths, 1.83 and 2.60 mm pin lengths, 3 and 6 s dwell times, and varying tool rotational speeds within the range of 1000 to 2000 rpm. The results showed that the weld strength is most affected by the rotation speed as shown in Figure 2.19(a). The microstructure analysis investigation showed the welds are stronger when the Cu ring is extruded upwards from the Cu sheet (lower sheet) into the Al sheet (upper sheet). The depth of the Cu ring helped to strengthen the bonding between the two sheets, Figure 2.19(b) and

(c). The SEM images revealed that no intermetallic compounds were found at the interface between the welded sheets.

2.5 FSSW Applications of Other Materials

A full understanding of the FSSW process is needed to respond to the massive request in the included manufacturing industries. This section shows a review of the published studies in terms of various aspects of the FSSW welds applications.

Shen et al. [78] performed the FSSW welds of the AZ31B magnesium alloy. They discussed in detail the relationships between the pin diameter, the microstructure, and the mechanical properties. The microstructure properties studied in detail were the interface region in the welds and the grain size of all, the stir zone, the thermo mechanical zone, and the heat affected zone. The shear-tensile force of the spot welds increased with the pin diameter increasing because of the effect of the latter on the increase in the height and width of the hook interface, which dominate in the failure of welds according to their conclusions.

Bilici et al. [79] investigated the weldability of high density polyethylene using FSSW. They welded sheets of 4 mm thickness and tested the weld strength of the joints under shear loading conditions. To analyze the results, the design of the experiments was utilized by the welding parameters. Two fracture types were observed, pull out and cross nugget failure modes as shown in Figure 2.20. The optimum parameters were a 700 rpm rotational speed, a 6.2 mm plunging depth, and a 60 s dwell time, which was the dominant welding parameter on the strength.

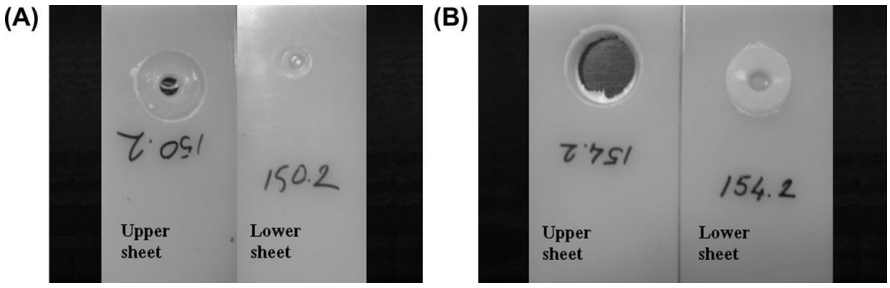

Figure 2.20 (A) cross nugget failure, (B) pull nugget failure [79]

Bozzi et al. [80] welded Al 6016 alloy of 1 and 2 mm thickness to an IF-steel sheet of 2.0 mm thickness using a tool of tungsten-rhenium alloy. A linear relationship was found between the tool rotational speed and the plunging depth, and the thickness of the intermetallic compounds. They also observed the existence of intermetallic compounds (within a limited thickness), which is important to improve the joint strength. However, if the intermetallic layer is too thick, this tends to easily crack the initiation in the welds through the intermetallic layer.

The FSSW process investigation on the sheets of 1 mm thickness Zr-based bulk metallic glass via an apparatus to control the friction time and plunging depth was conducted by Shin and Jung [81]. The process profile and test variables used are shown in Figure 2.21(a).

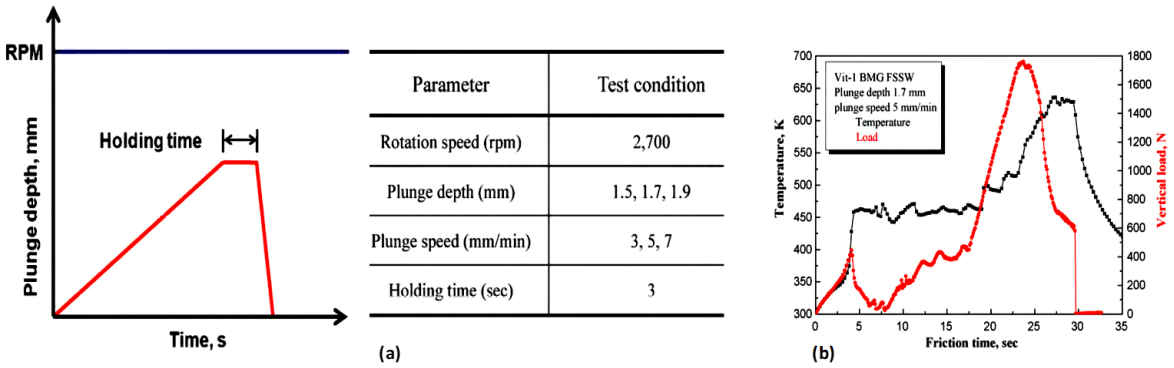

Parameter	Test condition
Rotation speed (rpm)	2,700
Plunge depth (mm)	1.5, 1.7, 1.9
Plunge speed (mm/min)	3, 5, 7
Holding time (sec)	3

Figure 2.21 (a) process profile and test conditions, (b) vertical load and temperature history [81]

The pressing of the vertical load on the specimens and temperature history were measured. The oscillation of the vertical load showed an interesting phenomenon, it initially increased up to ~600 N with the temperature before decreasing suddenly to 50 N until the 18 s. After the 18 s, the vertical load increased again, and the peak value was different depending on the test variables, Figure 2.21(b). The data showed was closely related to the behavior of the bulk metallic glass deformation in the supercooled liquid region. The shear-tensile test observation describes the behaviors of the FSSW of bulk metallic glass sheets. The load–displacement curves obtained records of 1.2 kN as a maximum failure force.

The FSSW joints of the lap welds were formed between the sheets of 1.4 mm thickness martensitic hot-stamped boron steel (HSBS) by Hovanski et al. [82]. The material of the tool was polycrystalline cubic boron nitride (PCBN) of a 2.3 mm pin length and a 10.2 mm shoulder diameter. Using different parameters led to variance in the joint strength from 6 to 12 MPa. The effect of changing the dwell time was emphasized, and the increasing of the dwell time led to a 40% to 90% direct increase in the welds' strength. The shear-tensile test for several samples was terminated before the ultimate failure load to understand the

failure mechanisms. The cross-section of a partially failed sample is shown in Figure 2.22(a) presenting a crack propagation at the sheets' interface along the softened, zigzag, and thin ferritic region within the weld nugget.

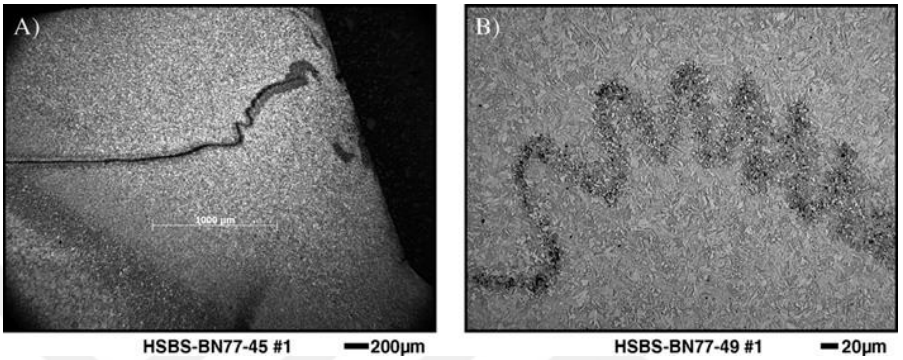

Figure 2.22 A sample pulled to partial failure: (A) crack propagation along the ferritic region in the weld nugget, (B) close view of the zigzag, thin ferritic region [82]

2.6 Design of Experiment (DOE) Applications in FSSW

The Design of an Experiment (DOE) is an experimental strategy in which the effects of multiple factors are studied simultaneously by running tests at various levels of the factors. The levels to be taken, the combination of levels, and the number of experiments to be run are given in the DOE [83]. The guidelines for the DOE:

1- Recognition and statement of the problem.

2- Choice of the factors, levels, and ranges.

3- Selection of the response variable.

4- Choice of the experimental design.

5- Performing the experiment.

6- Statistical analysis of the data.

7- Conclusions and recommendations.

All the DOE methods can eliminate the need for performing experiments on the basis of the traditional trial and error methods which is economically unjustifiable and time consuming [84,85]. In the FSSW applications, the optimum welding conditions will be obtained based on the DOE results. This statistical method is aimed at distinguishing the most affected significant parameters and rate contribution of each of these parameters on the responses of the welded joints by directing the least number of the tests utilizing the Taguchi orthogonal array (OA). The selection of an OA is an important stage in conducting the DOE. The number of parameters and the levels of these parameters are the points which are to be considered before using an OA [86]. The ANOVA investigation is a part of the DOE, which is performed to identify the process parameters that are statistically significant [87]. The purpose of the ANOVA test is to investigate the significance of the process parameters which affect the strength of the joints. It compares the response variable means at the different levels of the welding factors to evaluate the importance of one or more of them on the quality of the welded joints.

The quality of the FSSW welded joints was evaluated by Bozkurt and Bilici [88]. They investigated the effect of plate positioning on the quality of the fabricated joint of the dissimilar sheets of 1.6 m Al 2024-T3 and 1.5 mm Al 5754-H22 alloy. The welding variables optimization was done based on Taguchi's L9 OA and their contribution percentages were estimated by applying ANOVA. The experimental results displayed the plates positioning

importance on the strength of the spot welds produced. Figure 2.23 displays the results of the ANOVA in case1 (Al 2024-T3 sheet was above) and case 2 (Al 5754-H22 sheet was above). According to case 2, the most important parameter effect on the shear-tensile force was the rotational speed, which explains the 57.60% contribution of the total variation. Therefore, other parameters were selected according to the rotational speed.

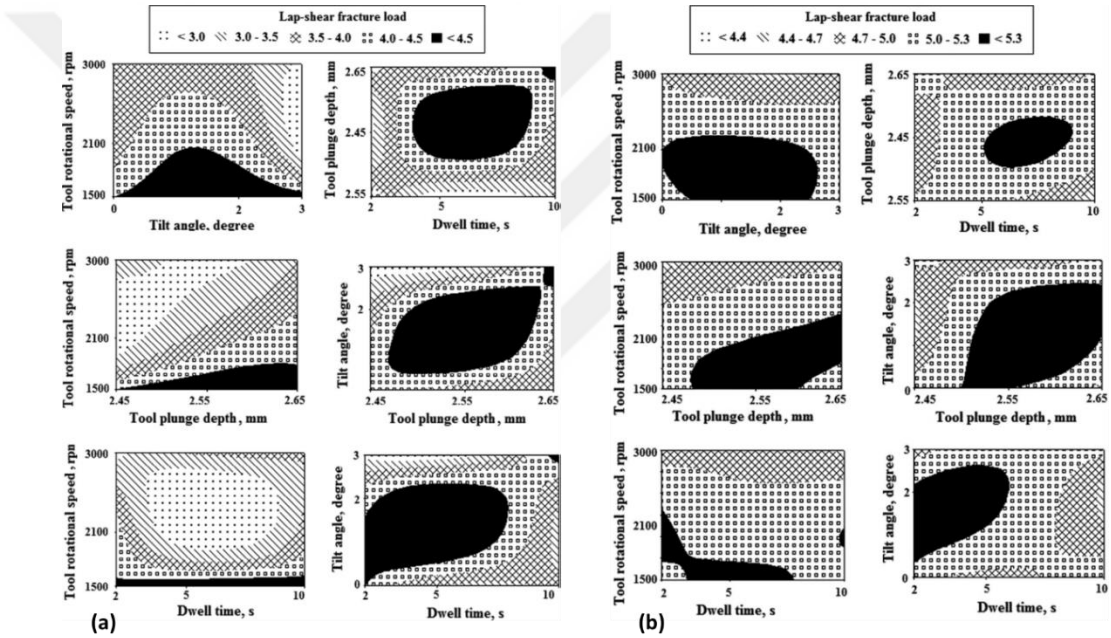

Figure 2.23 ANOVA analyses results for shear-tensile force of (a) case 1 and (b) case 2 [88]

Verastegui et al. [89] fabricated the spot joints between the plates of the Al 6181-T4 alloy and DP600 steel, which were used both with and without galvanized surface by using the Refill FSSW. The Taguchi statistical method was utilized to find the optimal welding variables, which led to producing the joint with the best mechanical properties. The results of the shear-tensile tests showed that the galvanized surface did not have any effect on the joint strength (6580 N for the galvanized surface in front of 6360 N for non-galvanized

surface), although different joining mechanisms were observed. Figure 2.24 shows the analysis results of the Taguchi method in this study.

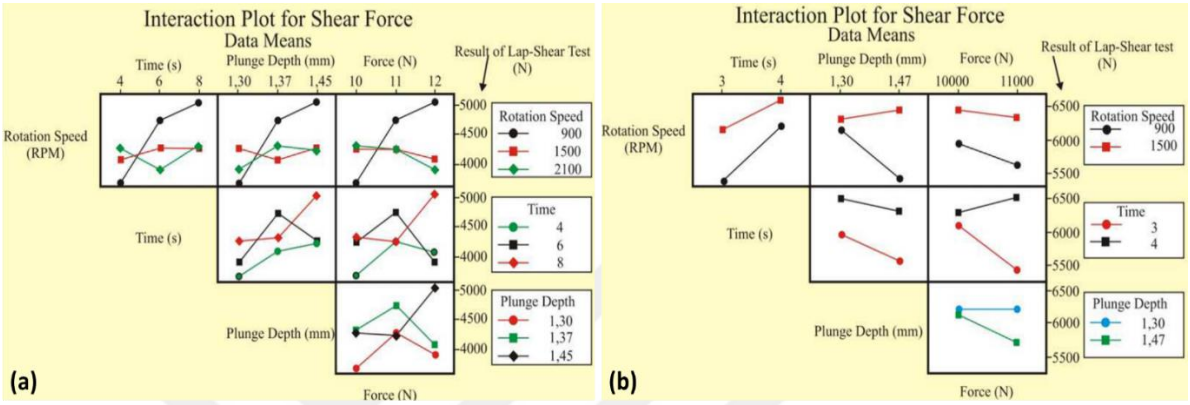

Figure 2.24 Taguchi optimized parameters for joints produced for (a) galvanized steel and (b) non-galvanized steel [89]

2.7 Finite Element Analysis of FSSW

The finite element method is a powerful numerical technique, it was developed in 1956 for the analysis of aircraft structural problems. Today, it is considered as one of the best methods for solving a wide range of practical problems efficiently [90]. Although much of finite element analysis is used to verify the structural integrity of designs, more recently, it has been used to model manufacturing processes [91,92].

An explicit finite element code was modeled by Awang et al. [93] to present a FSSW process model. The material (Al 6061-T6) flow and temperature distribution were simulated. Figure 2.25 shows the separation of the workpiece's edges in the simulation, which is similar to the deformed shape observed experimentally. Although the experimental measurement of the temperature was not available in this study, the maximum temperature was 948 ^{o}C theoretically, which is practically high and unrealistic in such models.

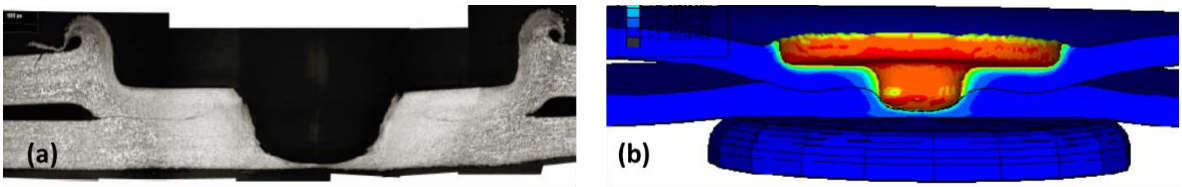

Figure 2.25 The deformed shape of the weld cross-section (a) practically and (b) theoretically [93]

The coupled thermo-mechanical viscoelastic finite element model, which was based on the character of FSSW, was used to study the temperature history of the FSSW joints by Gao et al. [94]. The model was calibrated by comparing the temperature history obtained from the experimental data that was recorded at 3 and 5 mm distance at the edge of the tool shoulder. The matching between the predicted and experimental temperature is shown in Figure 2.26. The reason for the slow increasing temperature at the beginning was due to the small friction area as well as the large distance to the thermocouple point before increasing rapidly once the shoulder came into contact with the sheet.

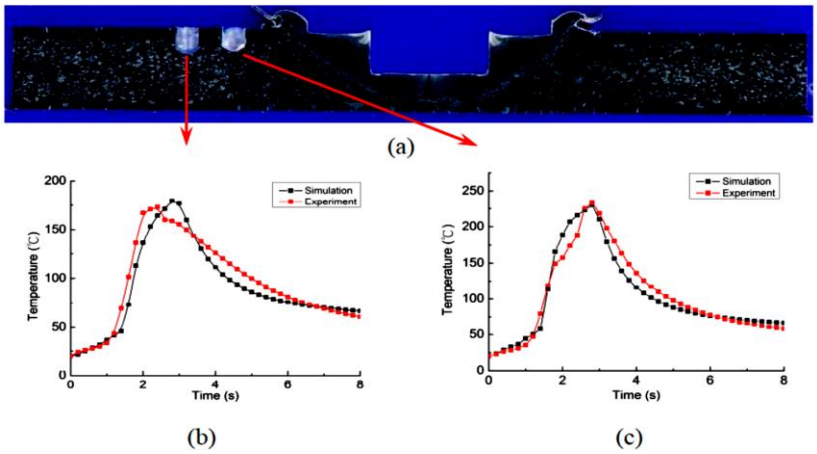

Figure 2.26 Temperature verification: (a) thermocouple insertion points, (b) and (c) comparison of temperature history between model and experiments data [94]

The Finite Element model for the plunging phase effect on the forge force of FSSW was developed by Khosa et al. [95]. A three dimensional, transient, thermal-stress analysis

was used to obtain the thermo-mechanical responses of the 3 mm thickness welded workpiece. In this model, there were multiple steps to allow the mesh remapping between each step. The mechanical and thermal properties for the Al 6082-T6 alloy were used in this investigation. The results from the theoretical and experimental investigations are shown in Figure 2.27. The tool rotational speed effect on the forge force was also observed in these results. It is clear that results did not match any of the forge force increases and drop behavior. The reason was assumed to be due to the difference in the plunge rates of the computational study (72.0 mm/min) and experimental study (11.3 mm/min) in the respective observations.

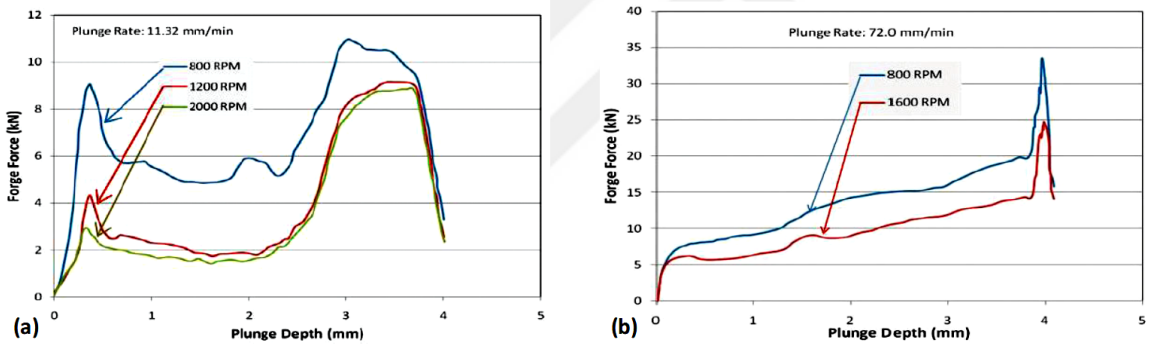

Figure 2.27 The output of forge force vs time at rotational speeds (a) experimentally and (b) Theoretically [95]

2.8 Fatigue Behavior of FSSW Joints

The fatigue test is considered as one of the important mechanical tests to evaluate the fatigue properties of the joints in the welding applications. The welding strongly affects the material by the process of heating and subsequent cooling. The damage of the welded joints begins in the weaker crystalline zones and becomes visible in the advance stage by plastic deformation, formation of micro-cracks on slip bands, coalescence of micro cracks, and finally the propagation of a main crack. Many factors have an influence on the fatigue of the

friction stir welded joints, the different behavior of the materials used, the behavior of the loading applied, and the effect of the welding process parameters used. For this reason, fatigue analyses are of high practical interest for all cyclic loaded welded structures, such as ships, offshore structures, cranes, bridges, vehicles, and railcars etc. [96,97]. There are some studies which have focused on the fatigue and cracks' behavior of the FSSW welded joints [98–100].

The fatigue lives of the friction stir spot welds of the Al 6061-T6 lap shear specimens were investigated. It was noticed that under cyclic loading conditions, the fatigue crack was initiated near the possible original notch tip in the stir zone and propagated along the circumference of the nugget zone, and then through the sheet thickness before the final fracture was caused [101].

There are few studies that have worked on keyhole refilling as a post treatment after the FSSW process, especially the fatigue behavior of these welded joints, which is an important issue for ensuring safe and reliable applications. Uematsu et al. [51] reported that the FSSW welds' quality was achieved using a specially designed tool, which could refill the keyhole of the spot welds made of the Al 6061-T4 alloy sheets of a 2 mm thickness. Figure 2.28 shows the relationship between the loading and life in both the joints with a probe hole and the re-filled one in addition to the joints fabricated by a conventional concave FSSW tool. The results showed that the tensile strength of the welds that were refilled was higher than that with the keyhole by 30%, whereas the fatigue strength was nearly the same as that of the refilled welds and the welds with the keyhole.

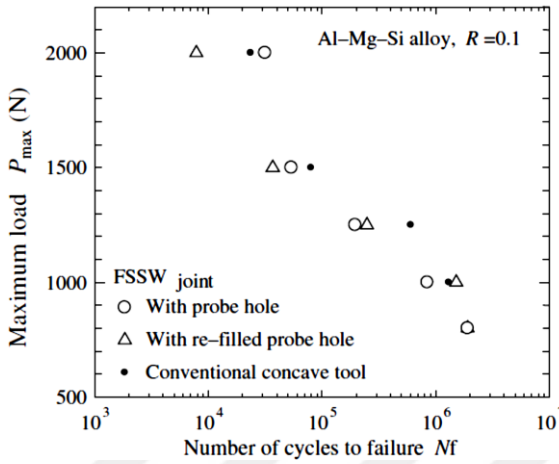

Figure 2.28 Fatigue results for the FSSW welds under cyclic loading [51]

Lin et al. [102] detected different failure modes between the quasi-static loads and the fatigue loads for the FSSW of the Al 6061-T6 sheets, in which under the quasi-static loads, the upper nugget pullout failure mode was seen, whereas under the fatigue loads, both the upper and lower nugget pullout were observed. Figure 2.29 shows the experimental results for the spot welds under the cyclic loading conditions.

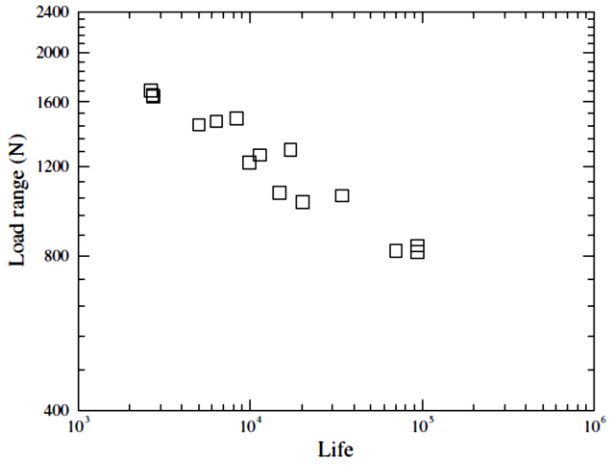

Figure 2.29 Fatigue results for the FSSW welds under cyclic loading [102]

Hassanifard et al. [103] introduced a new FSSW process to the weld Al 7075-T6 plates by using a localized plasticity to enhance the strength and fatigue life of the welded joints. However, the keyhole in the weld center transferred to an open hole according to their work. The applied load versus the number of cycles to failure are presented in Figure 2.30. As illustrated, the cold expanded samples have longer fatigue lives at lower load levels than that with higher levels. However, the life improvement is not appreciable at the low cycle regimes.

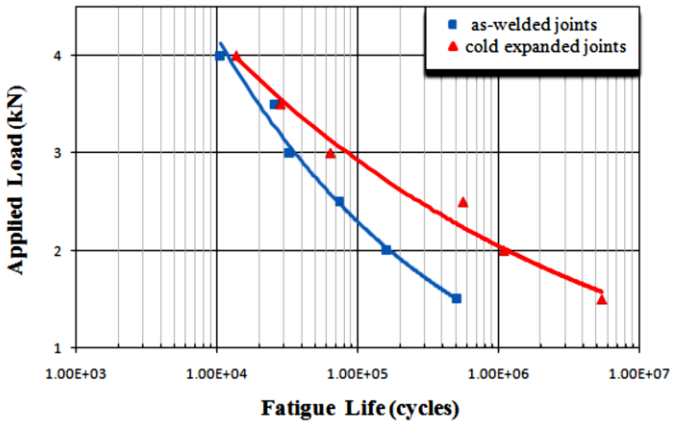

Figure 2.30 Experimental data obtained from the fatigue test [103]

2.9 The Intermediate Layer Friction Stir Spot Welding (IL-FSSW)

The conventional FSSW is developed by using an intermediate material layer, which is placed at the center between the sheets to be welded. Because of this layer, the upper sheet is elevated. When the shoulder presses the upper sheet to affix it with the IL and the lower sheet, a convex protrusion enclosing the intermediate layer is forms. This protrusion plays a significant role due to the contact at the interface between itself and the welding tool at a level higher than the upper sheet with a distance almost equal to the thickness of the

intermediate layer itself. The stationary shoulder also prevents the moving of the sheets during the process.

When the welding tool begins to rotate and descends simultaneously, the frictional heating occurs at the top of the protrusion. The temperature increases as the tool moves downwards, resulting in the stirring and plastic deformation of the upper and lower sheets with the IL. This helped to reduce the required plunging force and depth to achieve the flowability needed for the material during the stirring action to make the weld nugget. A flat welding spot was created after the welding tool reached the base of the protrusion at the original surface level of the upper sheet. The absence of a keyhole does not require any post-weld processing and the principle of this operation is further explained in Figure 2.31.

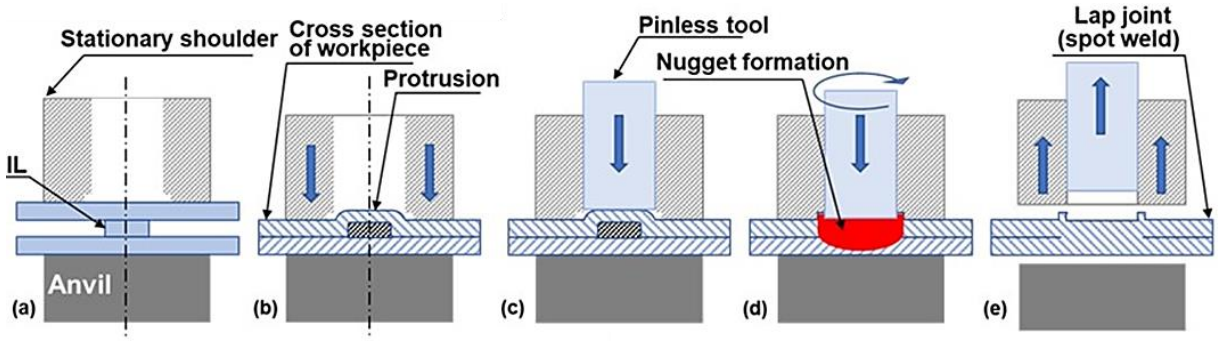

Figure 2.31 Schematic illustrations the IL-FSSW process

CHAPTER III

EXPERIMENTAL METHODS

3.1 As Received Materials Characterization

3.1.1 Al 6061 Aluminum Alloy

The standard and actual chemical composition of the as-received 1 mm thickness sheets of the Al 6061-T6 are given in Table 3.1. Two heat treatment tempers of this alloy, solution heat-treated and artificially aged (T6), and annealed (O) were used in this study to fabricate similar and dissimilar joints using the IL-FSSW process.

Table 3.1 Standard and actual chemical compositions of Al 6061-T6 alloy (wt %)

Element	Si	Fe	Cu	Mn	Mg	Ti	Zn	Cr	Al
Standard value [56]	0.4-0.8	<0.7	0.15-0.4	<0.5	0.8-1.2	<0.25	<0.15	0.04-0.35	Balance
Actual value	0.75	0.43	0.23	0.13	0.87	0.05	0.03	0.18	Balance

The Al 6061 material was received in a T6 temper (solution heat-treated and having undergone a precipitation heat treatment, which is also called artificial aging [104,105]). In order to apply the IL-FSSW on the Al 6061 alloy sheets in the O temper, an annealing treatment was performed on the as-received Al 6061-T6 by heating the sheets to 400 °C for

3 hours inside a furnace and then cooling at 10 °C per hour from 400 °C to 260 °C [106]. Annealing is a thermal treatment that is used to soften metals by reducing the yield strength and relieving stresses induced by cold or hard work from the solid solution state [105]. Al 6061 sheets in both treatment conditions, T6 and O were cut by a wire cut electro-discharge machining (EDM) to dimensions of 100×25 mm.

3.1.2 Al 2024 Aluminum Alloy

One mm thickness of Al 2024 sheets in two temper designations, solution heat-treated (T3) and O, were used for the IL-FSSW in order to fabricate similar and dissimilar joints. The as-received material was received in T3 temper (solution heat-treated, cold-worked, and naturally aged to a substantially stable condition) [104,105]. The chemical composition of the commercial Al 2024-T3 alloy is given in Table 3.2.

Table 3.2 The standard and actual chemical compositions of the Al 2024-T3 alloy (wt %)

Element	Si	Fe	Cu	Mn	Mg	Ti	Zn	Cr	Zr	Al
Standard value [56]	<0.5	<0.5	3.8-4.9	0.3-0.9	1.2-1.8	<0.1	<0.25	<0.1	<0.2	Balance
Actual value	0.08	0.12	4.48	0.53	1.49	0.036	0.04	<0.01	<0.01	Balance

Prior to applying the IL-FSSW on the Al 2024 alloy sheets in O temper condition, the annealing treatment was performed on the as-received Al 2024-T3 at 400 °C for 3 hours inside the furnace and cooled at 10 °C per hour from the annealing temperature to 260 °C [106]. This treatment was necessary not only for removing the effect of the previous heat

treatment, but also for homogenizing the microstructure of the as-received Al 2024-T3 alloy. The Al 2024 sheets in both the T3 and O tempers were cut by using a wire cut EDM to dimensions of 100 × 25 mm.

3.1.3 Pure Copper Alloy

The as-received commercial pure copper alloy that was used in this study was a 1 mm thickness sheet to fabricate dissimilar IL-FSSW joints of pure Cu to Al 6061-O. The chemical composition of the pure Cu sheets, which were used in this study, is summarized in Table 3.3. The sheets were cut by using a wire cut EDM to dimensions of 100×25 mm.

Table 3.3 The Standard and actual chemical compositions of the pure Cu alloy (wt %)

Element	Al	Fe	Cr	Te	Zn	As	O_2	P	Pb	Si	Cu
Standard value [107]	-	-	-	<0.001	-	-	0.002-0.003	<0.0003	-	-	99.9
Actual value	0.005	0.005	0.0003	0.29	0.004	0.007	0.0002	0.002	0.002	0.009	Balance

3.2 Design of the Fixture and Welding Tool

Figure 3.1 illustrates the fixture which was used for this study for the IL-FSSW processing. The fixture was made of mild steel, which was used to clamp the sheets to be welded with the IL part. It was designed to be universal, i.e., to be used with different tool diameters by changing the stationary shoulder part only. Moreover, it was designed to be able

to place in the special rig that used to measure the torque and axial load values of the tool through the welding process.

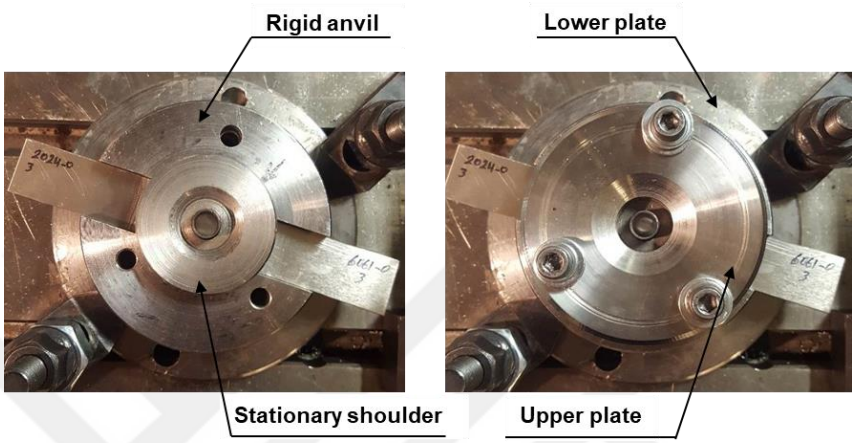

Figure 3.1 Schematic representation of the fixture of the IL-FSSW processing

The welding tool that used in this study was made of high-speed steel. The dimensions of the tool in the present experiment had a shoulder diameter of 10 mm with a flat tip (without pin) as shown in Figure 3.2.

Figure 3.2 The flat tip welding tool used in this study

3.3 IL-FSSW Process Parameters

The IL-FSSW parameters were selected based on an experimental design incorporating an L16 OA test matrix with LSFF selected as the response factor [108,109].

Finding the ranges of each parameter is very important for conducting the DOE. To find the range of each parameter, a number of trial runs were carried out with different combinations. Based on the quality of the joint obtained, the working limits were finalized. Hence, the range of the processing parameters in all the cases used are listed in Table 3.4.

Table 3.4 IL-FSSW processing parameters with their ranges and levels

Levels	Rotational Speed (N) rpm	Plunging feed rate (S) mm/min	Plunging depth (D) mm
Range	900-1800	15-30	0.6-0.9
1	900	15	0.6
2	1200	20	0.7
3	1500	25	0.8
4	1800	30	0.9

3.4 Design of Experiment (DOE) Based on Taguchi Method

As is listed in Table 3.5, an L16 OA test matrix with 3 parameters of rotational speed (N), plunging feed rate (S), and plunging depth (D) were applied to the response factor of the average LSFF in order to decrease the number of experiments from 64 to 16. To make sure of both the accuracy and repeatability of the results, three shear-tensile tests were performed on every welded sample for each set of parameters, and then the mean LSFF value of the obtained results was reported.

The main effect plots of the welding parameters on the LSFF values of the welds are shown in Figure 3.3. The comparison of their relative magnitudes helps to selecting the optimum parameters for each case of the welds.

Table 3.5 The welding parameters used and output responses of the average LSFF based on the Taguchi method

S.No.	Parameters			Average of LSFF(N)						
	N (rpm)	S (mm/min)	D (mm)	Al 6061-O	Al 2024-O	Al 6061-T6	Al 2024-T3	Al 2024-O /Al 6061-O	Al 2024-T3/Al 6061-T6	Pure Cu/Al 6061-O
1	900	15	0.6	2219.23	2289.52	509.52	512.36	2152.15	595.16	1907.49
2	900	20	0.7	2201.50	2385.11	1736.45	674.44	2242.03	785.46	1934.24
3	900	25	0.8	2211.77	2438.43	1588.96	947.11	2392.12	985.33	2022.20
4	900	30	0.9	**2326.04**	2496.81	1610.51	876.95	2417.01	122.51	2044.67
5	1200	15	0.7	2065.47	2621.95	1868.49	727.16	2464.63	1812.06	2094.37
6	1200	20	0.6	1761.17	2552.00	2216.24	654.81	2398.88	1206.59	2124.66
7	1200	25	0.9	2136.01	**2783.85**	**2875.14**	1418.12	**2616.82**	3929.43	2416.86
8	1200	30	0.8	1975.71	2655.30	2411.91	1374.28	2495.98	3465.37	2355.89
9	1500	15	0.8	1883.71	2548.82	1625.74	1343.96	2355.89	3836.71	2392.12
10	1500	20	0.9	1985.98	2581.77	1939.26	**1762.76**	2476.86	**4150.43**	2417.00
11	1500	25	0.6	1483.12	2228.05	1104.35	1245.66	2094.37	2845.36	2312.00
12	1500	30	0.7	1545.39	2239.00	1469.72	1125.39	2104.66	3125.87	2172.15
13	1800	15	0.9	1705.94	2217.73	1793.68	1047.92	2184.67	2954.46	**2564.35**
14	1800	20	0.8	1555.65	2202.34	1463.53	1245.72	2070.2	2766.34	2525.98
15	1800	25	0.7	1355.35	1961.96	1253.69	1102.40	1944.24	2403.57	2518.88
16	1800	30	0.6	1155.06	1901.58	1685.27	1024.97	1917.49	2241.38	2324.63

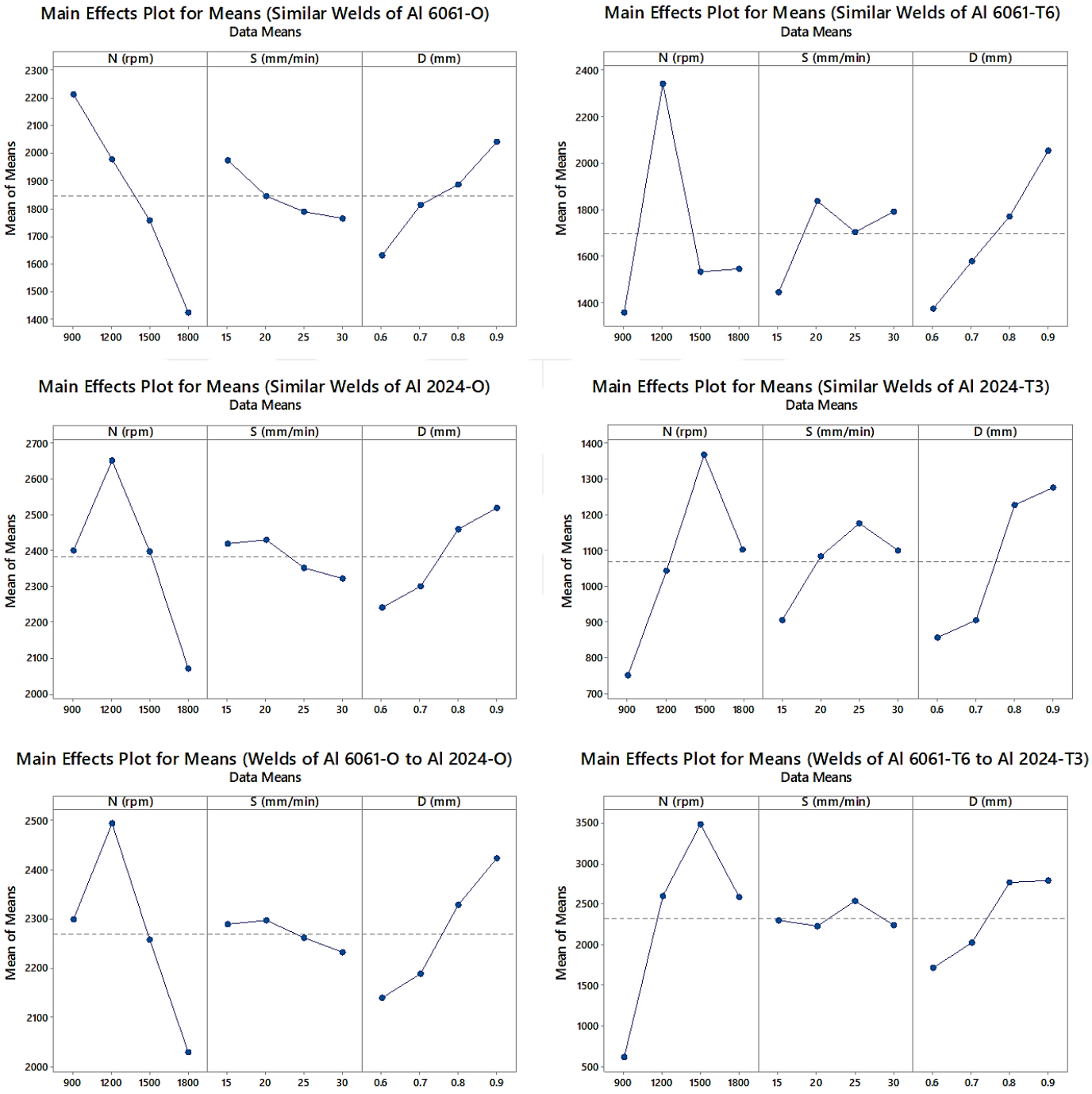

Figure 3.3 The main effect plots of the welding parameters on the LSFF values

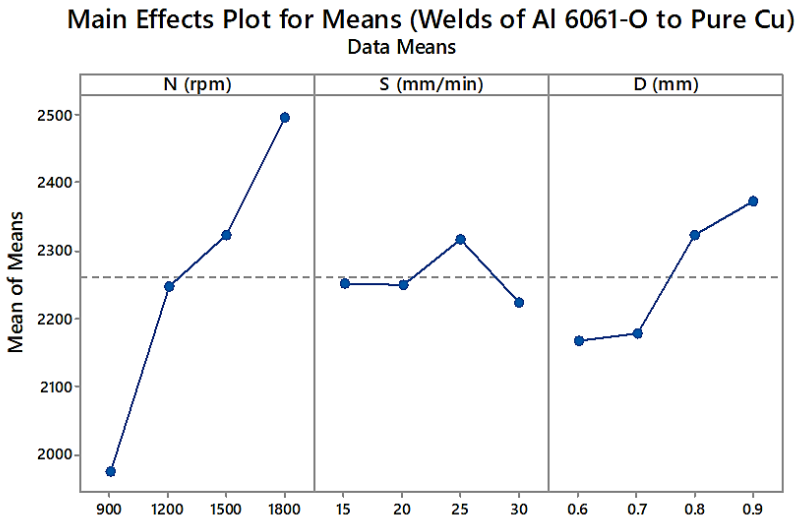

Figure 3.3 (Continuing)

In respect to Figure 3.3, it can be understood that increasing the plunging depth caused the improvement of the LSFF linearly. This trend made the plunging depth an important factor that contributed to obtaining the higher strength of the welds produced. Therefore, 0.9 mm was selected as plunging depth for all welding cases that were used in this study. Based on the results of the experiments and to gain the optimized strength of the welds, a rotational speed and plunging feed rate of 900 rpm and 15 mm/min were selected, respectively, for the case of the welding similar sheets of the Al 6061-O, whereas for the case of welding similar sheets of the Al 6061-T6, similar sheets of Al 2024-O, and dissimilar sheets of Al 6061-O/Al 2024-O, the rotational speed and plunging feed rate of 1200 rpm and 20 mm/min were selected, respectively, with a plunge depth of 0.15 mm. In the case of welding similar sheets of Al 2024-T3 and dissimilar sheets of Al 6061-T6/Al 2024-T3, the selected rotational speed and the plunging feed rate were 1500 rpm and 25 mm/min, respectively. Finally, for the

dissimilar welding case of pure Cu/Al 6061-O, 1800rpm and 25 mm/min were selected as the rotational speed and the plunging feed rate, respectively.

3.5 Mechanical Testing

Mechanical testing was used to evaluate some of the mechanical properties for the welded joints in addition to the evaluation of the macro and microstructural changes of the welding zones. This section involved the standard procedures and techniques that were used to prepare the IL-FSSW welded samples as well as a brief definition of the tests used and their purpose.

3.5.1 Shear-Tensile Test

The shear-tensile welded samples of a rectangular, overlap shape, were prepared according to the AWS standard [110]. The samples were prepared in a direction in which the extension direction was parallel to the rolling direction, and the dimensions were 25×175 mm with an overlap area of 25 mm^2, Figure 3.4.

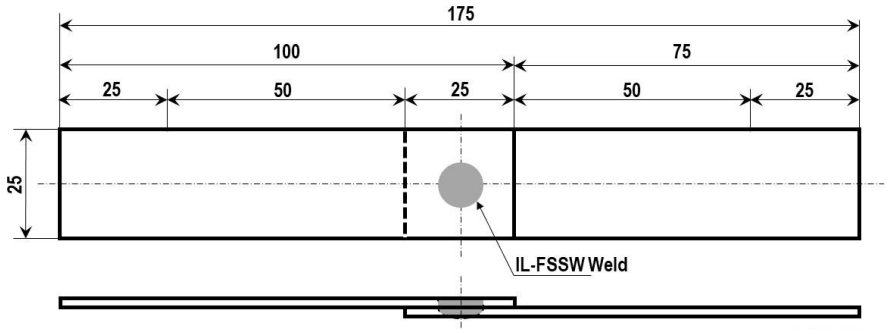

Figure 3.4 Lap shear-tensile test sample

Shear-tensile tests were carried out by using an Instron mechanical testing frame at an ambient temperature and at a displacement rate of 0.025 mm/s. The force and displacement values of the samples were measured and recorded consequently during test the processing until the occurrence of a fracture.

3.5.2 Hardness Measurement

The samples of the welds' cross-sections were prepared for the hardness test according to the ASTM standard for hardness [111]. The grinding process was conducted with up to 2500 grits papers before polishing the samples utilizing the 6, 3 and 1 μm diamond suspension. The microhardness of the samples after grinding and polishing was measured using a micro-hardness tester (FM-300e) with a force of 100 gf for 15 s indentation at an ambient temperature.

3.5.3 Axial Load and Torque Measurement

A special rig was constructed for the purpose of measuring the axial load and torque of the tool through the weld processing. This rig consisted of two 320 mm×180 mm×25 mm plates of mild steel (the upper one was sliding), and two guide columns and bushes at the center of the plate, Figure 3.5. The welding fixture was assembled with a rotating disc constructed in thrust bearing to withstand the axial load and rotatable free to help in measuring the torque of the tool, and this assembly was equipped with the upper surface of the sliding plate. The load cell, (1000 kg capacity, R.O:2.000 mV/V) was fixed to the center of the lower plate of the rig to support the upper sliding plate with the welding fixture assembly. Another load cell (1000 kg capacity, R.O:2.003 mV/V) was fixed horizontally at

the upper plate and normal to the welding fixture at 45 mm perpendicular distance in order to measure the maximum torque of the tool by convert the load values to torque through multiply the force value (F) times the lever arm ($r \sin\theta$) using Equation (3.1):

$$T_{max} = F \times r \sin\theta \quad \text{.....(3.1)}$$

where r is the (the radius from axis of rotation to point of application of the force, which is equal to 45 mm, and θ: is equal to 1 since θ=90 (maximum torque).

The signals from the load cells were amplified and sent to the 6 channels data acquisition (DAQ) which in turn was connected to a personal computer. Using LabVIEW software, the data of the axial load and torque were measured online during each weld processing and recorded in some worksheet files.

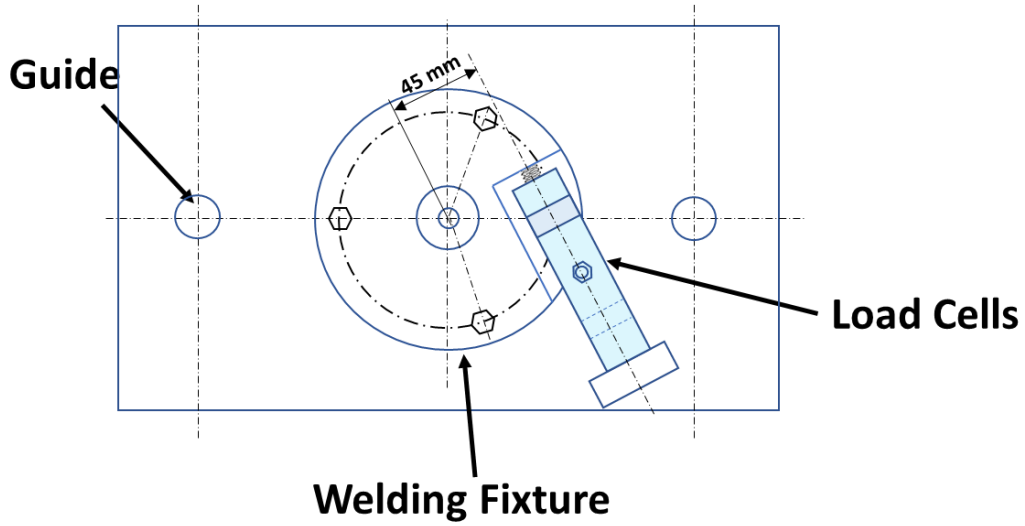

Figure 3.5 Schematic representation the top view of the rig designed to measure the axial load and torque of the welding tool

3.5.4 Fatigue Test

Fatigue samples were conducted using an electro-mechanical fatigue testing machine operating at a sinusoidal frequency of 15 Hz. The samples were subjected to constant amplitude sinusoidal loading with the loading ratio R=0.1 (P_{min}/P_{max}). The maximum load for the fatigue test was 2.5 kN, and this value corresponded to approximately three-quarters of the average LSFF (3203.5 N) of all the types of the welded joints that were fabricated and tested in this study. The fatigue tests were conducted at seven levels of applied load, ranging from 500 to 2500 N (500, 1000, 1250, 1500, 1750, 2000, and 2500 N). The tests were repeated three times for each level of load applied to ensure repeatability, and the load versus cycles relationship was showed by plot P-N curves.

The fatigue sample used is identical to the lap shear-tensile sample, but with 6 mm holes diameter drilled into the extremities of the samples to ensure compatibility with the clamping system of the fatigue machine that was used.

3.6 Temperature Distribution Measurement

The temperature distributions on the welded joints were measured during the IL-FSSW processing. Three thermocouples of the K (Ni-Cr) type with a temperature range of (-100 ºC - 1200 ºC) were inserted in the bottom side of the lower sheet at three different locations as shown in Figure 3.6. The first thermocouple was attached under the center of the nugget zone, and the second and third thermo-couples were attached at a distance of 10 mm and 15 mm distance from the first one, respectively. All the thermocouples were isolated to ensure intimate contact with the workpiece and to prevent contact with the backing plate (the

anvil). The temperature distribution history was recorded simultaneously through the welding processing.

Figure 3.6 Temperature distribution measurement

3.7 Microstructure Evaluation Methods

3.7.1 Optical Light Microscopy

The welded samples were sectioned at the centerline of the spot weld by the EDM, and then the samples were cold mounted by using a mixture of resin epoxy and hardener. A conventional metallographic preparation technique was applied. According to the ASTM E3-01 standard [112], the grinding process using water as a lubricant in order to cooling and prevent damage in the microstructure was conducted with 500, 800, 1200, 1500, and 2500 grits emery paper, and then the cloths of 6, 3, and 1 μm were used for polishing by diamond suspension by universal grinding and the polishing machine. The ground and polished samples were rinsed in ethanol and water after the grinding operation. Finally, the cross-sections of the welded samples were chemically etched to reveal the grain boundaries using two different etching solutions, which were provided for the Al 6061 and Al 2024 aluminum

alloys. The Weck's reagent (100 ml H_2O, 4 g $KMnO_4$ and 1 g NaOH) was used with the Al 6061 alloy. On the other hand, the Al 2024 alloy was etched immersing in the Keller's reagent (190 ml H_2O, 5 ml HNO_3, 3 ml HCl and 2 ml HF) [113]. A microscope attached to a camera was employed to reveal the grains in different magnifications.

3.7.2 Scanning Electron Microscopy (SEM)

In order to observe the fracture morphology of the different welds produced, a scanning electron microscopy (SEM) was performed for some failed samples after the shear-tensile and fatigue tests in high magnifications. The SEM studies, which aimed to recognize the microstructure surfaces and fracture mechanisms, were conducted in a JEOL SEM equipped with an energy dispersive spectroscopy (EDS) detector at an accelerating voltage of 20 kV (Figure 3.7). The EDS analysis was used to obtain evidence for the metallurgical bond that occurred between the copper and aluminum in the case of the pure Cu/Al 6061-O welds.

Figure 3.7 JEOL scanning electron microscope (SEM).

3.8 X-Ray Diffraction Examination (XRD)

X-Ray diffraction measurement was carried out at room temperature using a X'Pert Pro diffractometer with Cu Kα radiation anode (λ = 1.54 Å). The accelerating voltage of 45 kV and emission current of 40 mA were performed. In the current study, XRD is used to investigate the existence of the intermetallic compounds in the microstructure of the dissimilar pure Cu/Al 6061-O welded joints. The samples for the XRD were ground, polished, and then located on an inclining stage termed a goniometer. The dimension of the samples for the XRD were 10×5×2 mm, which is an effective area for measurements according to the operator recommendations. The exact position of the peaks was firstly measured, then the location of the source and detector was changed from one single set of planes to an individual pole. The reflected ray is utilized to obtain the concentration of the chemical compounds that were captured by the ray scan [114].

CHAPTER IV

THE CHARACTERIZATIONS OF Al 6061 AND Al 2024 SIMILAR AND DISSIMILAR WELDS FABRICATED BY THE IL-FSSW PROCESS

4.1 Microstructure and Hardness Characterizations

The welds produced by the IL-FSSW process showed an excellent appearance as seen in Figure 4.1. Regardless of whether similar or dissimilar aluminum sheets were used, the appearances of all the spot welds were comparable. The top side of the weld spot showed a smooth surface with no large distortion resulting in the welded sheets, and it is considerable that no keyhole was formed when comparing conventional FSSW welds in other studies [88,115,116].

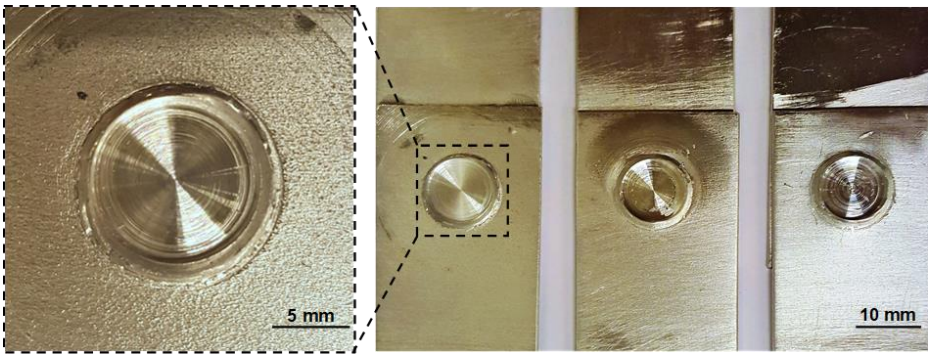

Figure 4.1 The IL-FSSW welds surface's appearance of the aluminum sheets

4.1.1 Similar Welds of Al 6061

Figure 4.2 shows the macroscopic views of the top and the cross section sides of the weld joints made by using the IL-FSSW for Al 6061 in both O and T6 tempers. These views

showed that sound spot joints with no keyhole were fabricated. However, some kissing bond regions [117,118] were found in the cross-section of the T6 welds at the interfaces of the sheets, which was because the Al 6061 alloy in the T6 temper was harder when compared to the O temper case.

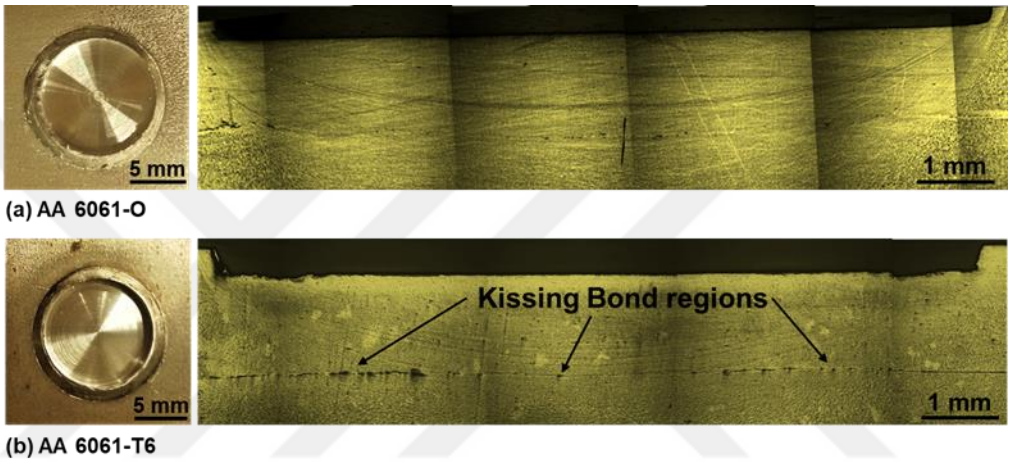

Figure 4.2 Top and cross section views of the weld's macroscopic appearance: (a) Al 6061-O and (b) Al 6061-T6

Figures 4.3 and 4.4 (a-d) specify the microstructures of the weld regions. These regions are the base material (BM), the heat affected zone (HAZ), the thermomechanical affected zone (TMAZ), and the stir zone (SZ) respectively. Figures 4.3 and 4.4 (b-e) show the average grain size (AGS) for the weld regions. The SZ region always shows finer grains than that in the BM region due to the dynamic recrystallization during the stirring process because of the forceful plastic deformation and high temperatures as shown in Figures 4.3 and 4.4. For the O condition, the AGSs in the BM, the HAZ, the TMAZ, and the SZ were ≈22 μm, ≈28 μm, ≈14 μm, and ≈3 μm, whereas for the T6 condition, the AGSs in BM, HAZ, TMAZ, and SZ were ≈15 μm, ≈23 μm, ≈12 μm, and ≈4 μm, respectively.

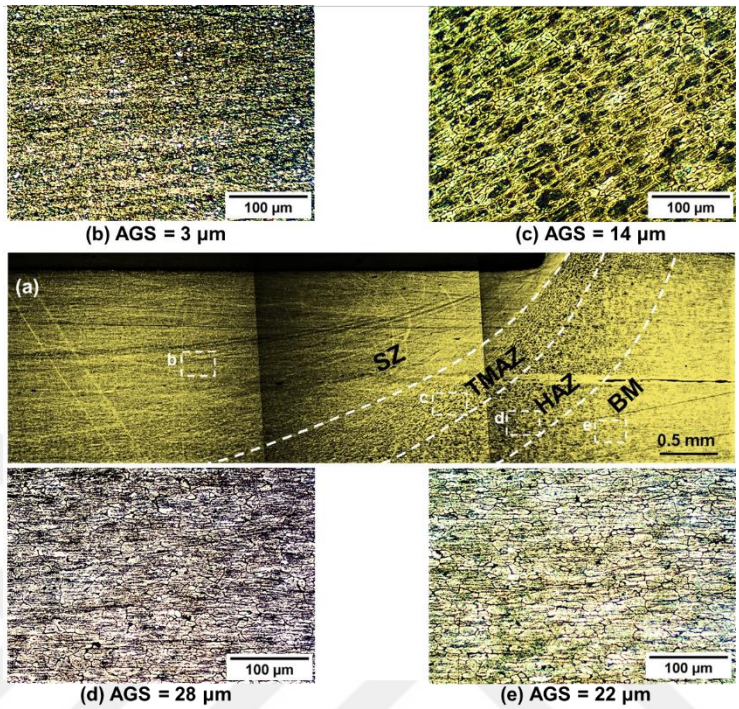

Figure 4.3 (a) Microstructures of the Al 6061-O joint: (b) SZ, (c) TMAZ, (d) HAZ, and (e) BM

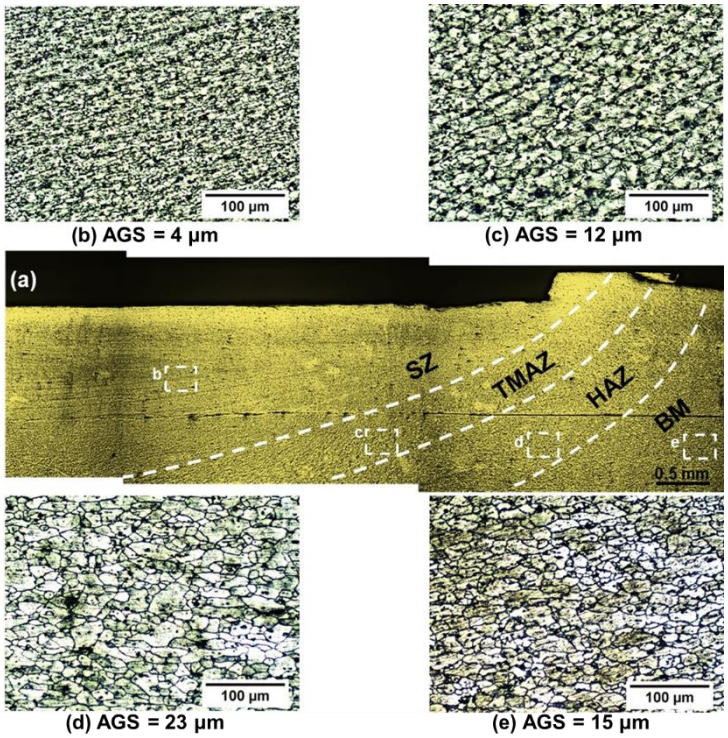

Figure 4.4 (a) Microstructures of the Al 6061-T6 joint: (b) SZ, (c) TMAZ, (d) HAZ, and (e) BM

Based on Figures 4.2, 4.3, and 4.4, it is clear that the joint was successful where the upper, lower sheets, and the IL were mixed rigorously, the SZ was considered to be the effective nugget zone of the IL-FSSW joint. The boundaries of the IL-FSSW weld regions were distinguished similarly to that recognized in the FSSW joint made by using the traditional FSSW [98,119,120]. A little flash can be seen on the top surface of the weld around the weld spot, which is because of the rotation movement of the tool. The interface between the upper and lower sheets, and the IL was difficult to observe, which indicated the proper mixing of these metallic parts in the SZ region. However, the presence of the kissing bond regions at the interfaces of the T6 sheets caused some areas to partially weld within the weld nugget.

The Vickers microhardness tests were conducted along four parallel lines on the cross-section, laterally from the weld center of the joint. Along each line, the test was done with a spacing of 0.25 mm between each indent as shown in Figure 4.5.

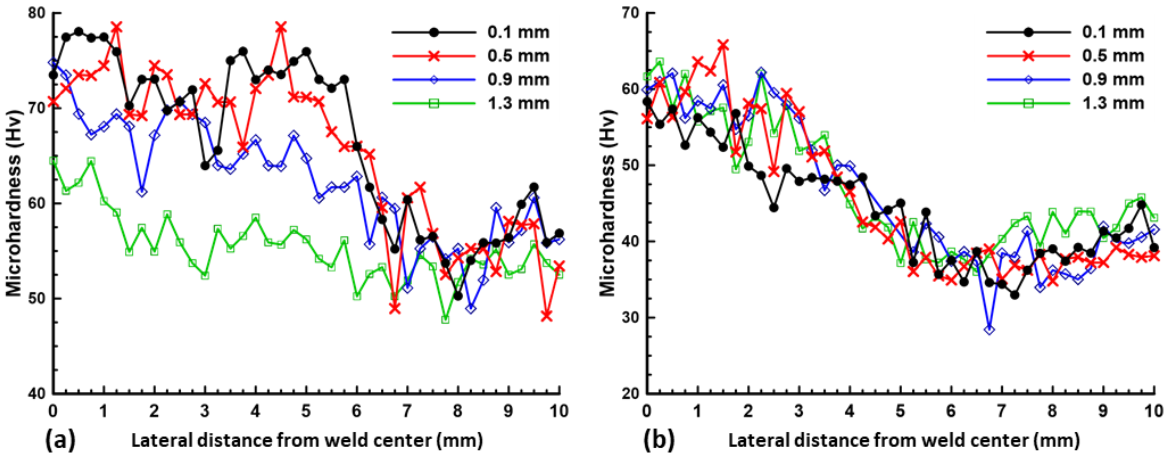

Figure 4.5 Hardness distribution of the Al 6061 welded joints in (a) T6 and (b) O tempers

According to Figures 4.5 (a) and (b), the hardness values of the Al 6061-T6 weld joint were higher than that in the Al 6061-O weld. This is because the Al 6061-O is softer and has low strength due to the annealing heat treatment effect when compared to the T6 condition. This explains why there was little difference in the hardness between the BM and the SZ regions of the 1.3 mm line of Al 6061-T6 hardness profile, Figure 4.5 (a). At this distance, the stirring effect was poor due to the alloy strength when compared with the same line of the weld in the O temper, Figure 4.5 (b).

Regardless of the temper type of the workpiece, the hardness at the weld center within the SZ was higher than the other weld regions. Far from the center of the weld, the hardness values gradually decreased through the TMAZ towards the HAZ, where it reached the minimum value [121]. After that, there were further increases towards the BM region exhibiting a concave shaped profile appearance. The low hardness in the HAZ was due to over aging, wherein a coarsening of the precipitates takes place. The SZ is associated with a very high temperature and severe plastic deformation as a result of the direct contact with the welding tool surface in this region, which leads to dynamic recrystallization and a very fine grain structure [122,123].

4.1.2 Similar Welds of Al 2024

Figures 4.6 and 4.7 show the transverse sections of the welds for the Al 2024 in both the O and T3 tempers. In these figures, visual inspections were unable to reveal any observable defects. Moreover, different regions of the welds were denoted as BM, HAZ, TMAZ, and SZ, respectively. The microstructures of the selected sections of these regions

are shown. As can be seen in these figures, the grain structure in the base metals are; slightly increased in the HAZ, elongated in the TMAZ, and significantly recrystallized in the SZ.

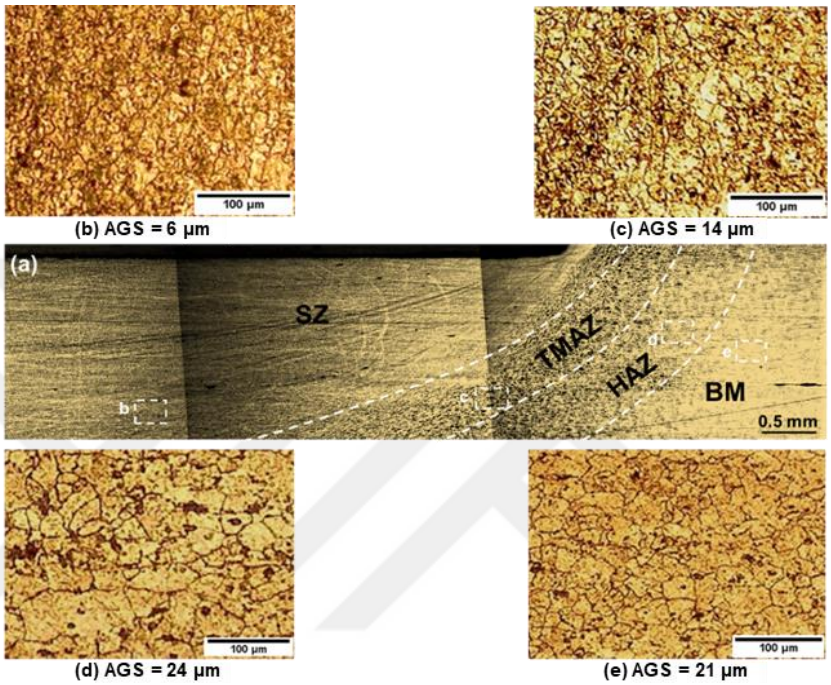

Figure 4.6 (a) Microstructures of Al 2024-O joint: (b) SZ, (c) TMAZ, (d) HAZ, and (e) BM

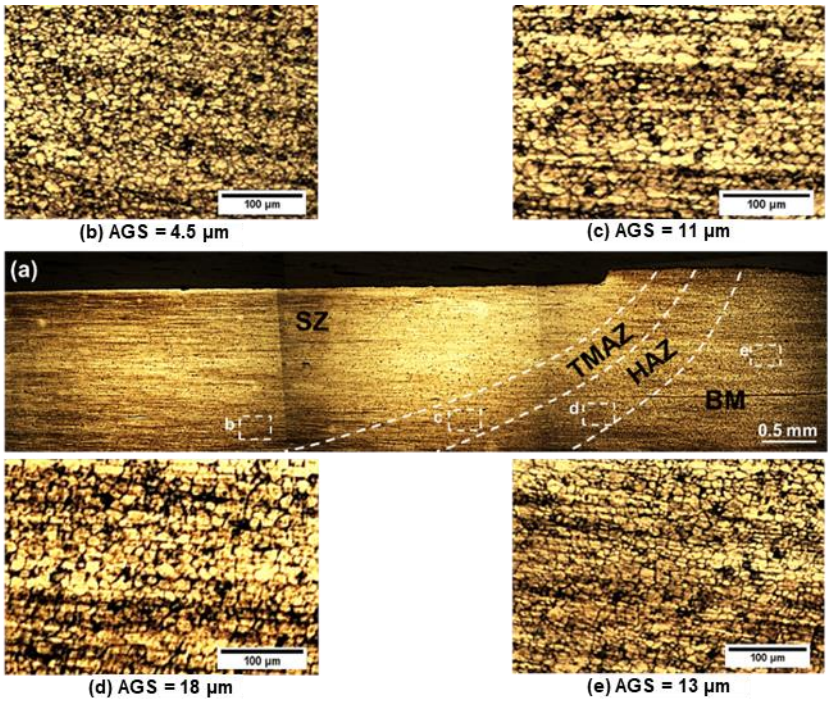

Figure 4.7 (a) Microstructures of Al 2024-T3 joint: (b) SZ, (c) TMAZ, (d) HAZ, and (e) BM

The largest plastic strain was realized in the SZ, which experienced a high temperature as 334 °C as measured experimentally. Consequently, the microstructure was entirely dynamically recrystallized [124]. Many authors have reported the occurrence of continuous dynamic recrystallization during the friction stir welding processes of aluminum alloys [125,126]. Hence, continuous dynamic recrystallization could take place in the nugget zone of the welded joints. The AGS within the nugget zone of both the O and T3 joints were about 6 μm and 4.5 μm, whereas the AGS of the BM were within 21 μm and 13 μm for the case O and T3 samples, respectively.

The hardness profile of the similar Al 2024 welded joints with the O and T3 conditions at the optimum process conditions are shown in Figures 4.8 (a) and (b). The hardness was measured along four parallel lines through the weld cross-section with a spacing of 0.1, 0.5, 0.9, and 1.3 mm starting from the top surface of the weld. The results observed some variation of microhardness in the BM, the HAZ, and the TMAZ regions between the welds of the T6 and O tempers. However, a similarity in the hardness was observed in the SZ. The hardness of the precipitation of the Al 2024 alloy depends greatly on the precipitate distribution, but slightly on the structure grain size [127]. In the case of the 2024-T3, the SZ showed a significant decrease of hardness in the weld nugget compared to the BM due to the over aging of the precipitates. However, grain refinement and precipitation occurred within the weld nugget as a result of the dynamical recrystallization, which led to an increase in the hardness values of the SZ. For the Al 2024-O welded sample, the microhardness values in the weld nugget were greater than those in the BM, the HAZ, and the TMAZ indicating that the SZ was strengthened by the weld processing through the grain

refinement caused by the dynamic recrystallization. Almost similar microhardness values in the SZ of both the T6 and O samples can be attributed to the same microstructures in these regions.

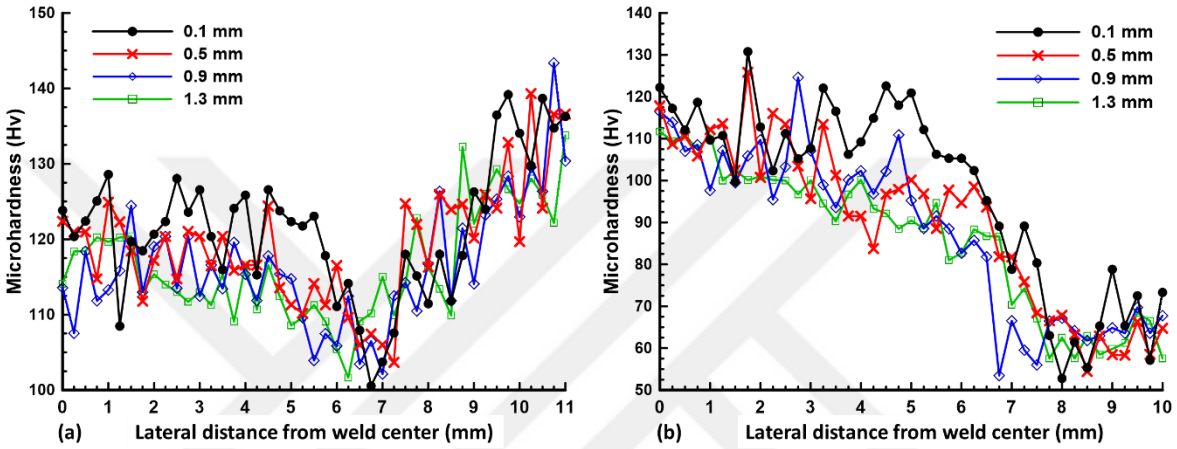

Figure 4.8 Hardness distribution of the Al 2024 welded joints in (a) T3 and (b) O tempers

4.1.3 Dissimilar Welds of Al 2024 to Al 6061

Figure 4.9 shows the cross-section of the Al 2024-O to the Al 6061-O dissimilar welds. The interface between the IL, the upper sheet, and the lower sheet is visible. No bond defect or cavity can be observed along the interface, which established that good metallurgical properties of the joint produced can be achieved. Additionally, the problem of the thickness reduction of the upper sheets in conventional FSSW [128] is discarded because the tool plunging distance in the IL-FSSW process in this study is not recommended to be any larger than the upper sheet thickness. As seen in Figure 4.9, the weld cross section was divided into four zones: BM, HAZ, TMAZ, and SZ, in which the SZ consists of the IL inside after the weld processing and hooks' formation. The grains structure of the BM is shown in

Figure 4.9(i), the AGS were ≈ 11 μm and 21 μm for the upper sheet and the lower sheet, respectively [129].

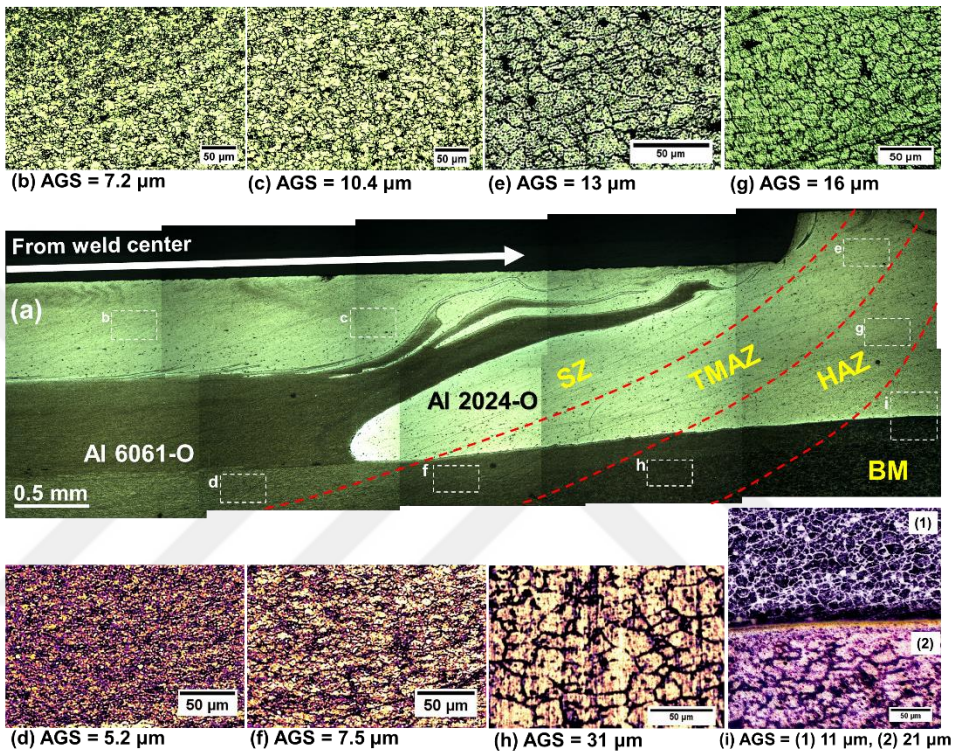

Figure 4.9 Microstructure images of the dissimilar Al 2024-O/Al 6061-O welds [129]

Figures 4.9 (g) and (h) shows the AGSs of the HAZ, which were ≈16 μm and 31 μm for the upper sheet and the lower sheet, respectively [129]. During the weld processing, there was no mechanical stirring effect on the aluminum grains in the HAZ, only the thermal cycle was affected, which tended to coarsen the grain sizes in this zone. Next to the HAZ, the TMAZ was characterized by deformed and elongated grains because of the impact of the mechanical and high temperature, Figures 4.9(e) and (f). The SZ was located in the center of the weld, Figures 4.9(b), (c), and (d). The minimum AGS in this zone was ≈ 5.2 μm. The SZ is characterized by fine, homogenous, and equiaxed microstructure because of the intensive

plastic deformation and high temperature in the border of the welding tool, which leads to the dynamic recrystallization of the grains in this zone [115,130].

Figure 4.10 shows the microstructure of the dissimilar Al 2024 to Al 6061 welds in the T6 temper. The weld cross section indicates that a strong joint without voids is present. The grain refinement in the SZ can be observed as shown in Figures 4.10(f) and 5(g) dues to exposure to the intense plastic deformation caused by the stirring. In addition, the partial recrystallization, due to the elevated process temperature, may also be essential in aiding the microstructural refinement. The characterization of the interface region between the IL and the lower sheet provides evidence of the bonding character. Although there are regions of partial bonding, the extended hook formation provides joint strength. As can be seen in Figures 4.10(c) and (d), the IL material flows along the pathway of the hook generation.

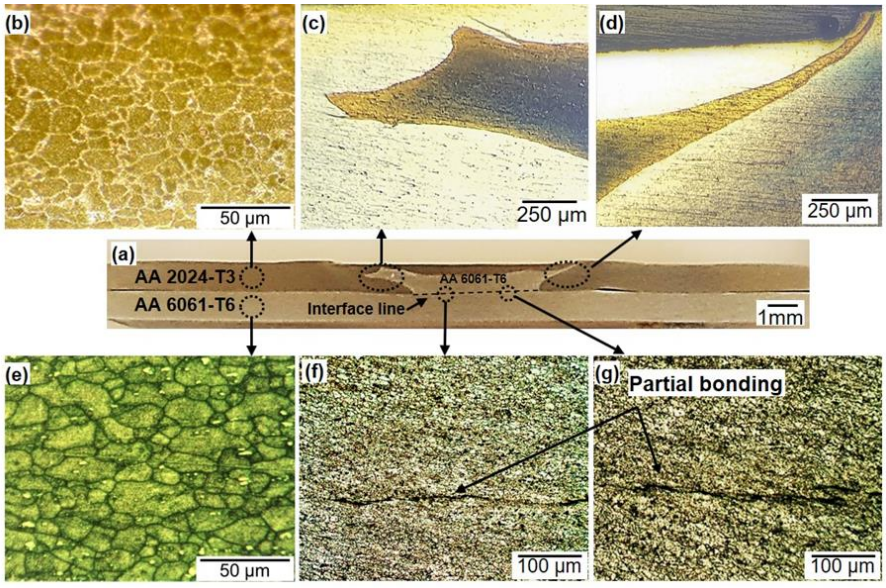

Figure 4.10 View of the hook formation and material distribution around the nugget zone in the dissimilar welds of Al 2024-O to Al 6061-O [131]

The most distinctive characteristic of the Al 2024/Al 6061 welds, in both tempers O and T6, fabricated by the IL-FSSW process is the presence of the extended hooks in the SZ, which is mainly responsible for the improved quality of the welds. Figures 4.9(a) and 4.10(a) reveal that the IL mostly penetrated the upper sheet (Al 2024) and the hooks with long branches were formed between the upper sheet and the top side of IL. The hooks were multi-layered in the O temper case when compared to the T6 case, which is probably because the sheets were much softer in the O temper condition when compared to the T6 condition. In contrast, the hooks between the lower sheet and the IL are smaller than that between the upper sheet and the IL. The difference can be attributed to the variation of the thermal effects on the hardness of the sheet material. Since the IL diameter (6 mm) is smaller than the tool diameter (10 mm), the heat input to the IL through the upper sheet was sufficient for the growth of the extended hooks. In the meantime, the lower sheet was in direct contact with the anvil, which also resulted in the quick loss of heat from the bottom side of the IL. This causes less softening and thus, eliminates the hook formation in this region, if there are any.

Figures 4.11(a) and (b) [129] show the hardness profile of the dissimilar Al 2024/Al 6061 welded joints in the T6 and O tempers condition. The hardness was measured along four parallel lines as mentioned above. The hardness values showed a slight decrease in the HAZ when compared to the measurements within the BM due to the relatively large grain size of the former. In the HAZ, the hardness increases gradually towards the direction of the weld center, passing through the TMAZ and finally peaking at the SZ. The grains located in the SZ are much finer due to the dynamic recrystallization leading to an increased hardness [47]. The curves in Figure 4.11 shows an almost identical distribution of the hardness along

both the Al 2024 and the Al 6061 sides. The Al 6061 side profile measurements exhibit smaller hardness values. Additionally, it is observed that the hardness values changed in the ranges of 70 Hv to155 Hv (in O temper case) and 86 Hv to168 Hv (in T6 temper case) in the SZ, which is uncommon in the conventional FSSW and can be linked to the utilization of an IL in the process presented herein.

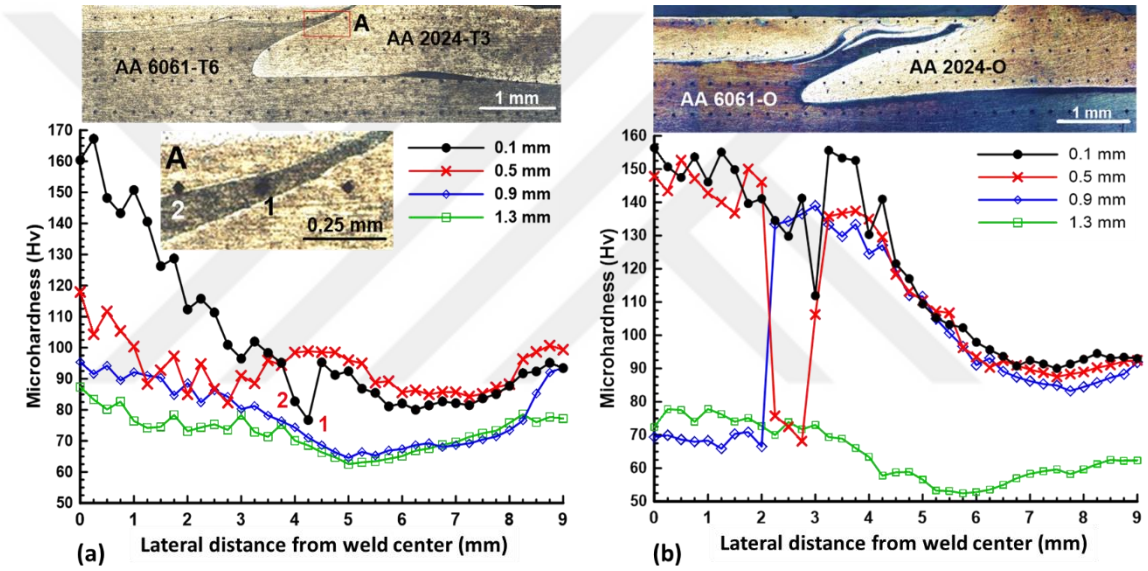

Figure 4.11 Hardness distribution of Al 2024/Al 6061 welded joints in (a) as received condition and (b) O tempers [129]

Fluctuation in the hardness values was apparent within the SZ area as can be explained by the spread of the softer hook structures (Al 6061) within the harder base metal (Al 2024) as indicated in magnified region (A) of the interdiffusion of the Al 6061 alloy from the IL part into the Al 2024 side, Figure 4.11(a).

4.2 Mechanical Characterizations

Figure 4.12 shows the LSFF-displacement curves of the IL-FSSW similar and dissimilar aluminum welded samples, which were manufactured in this study, during the lap

shear testing. According to Pan, the recommended minimum shear failure load of the friction stir spot welds should be on par with the AWS standard [132]. The shear failure force (ST) for the spot welds can be calculated according to the AWS using the following equation [110]:

$$ST = \frac{(-6.36\times10^{-7}\times S^2 + 6.58\times10^{-4}\times S + 1.674)\times S\times 4\times t^{1.5})}{1000} \quad \text{.....(4.1)}$$

where S and t are the tensile strength (the softer one in dissimilar case) and the sheet thickness, respectively. The tensile strength value was taken based on the experimental tensile results for the workpieces used as shown in Figure 4.13.

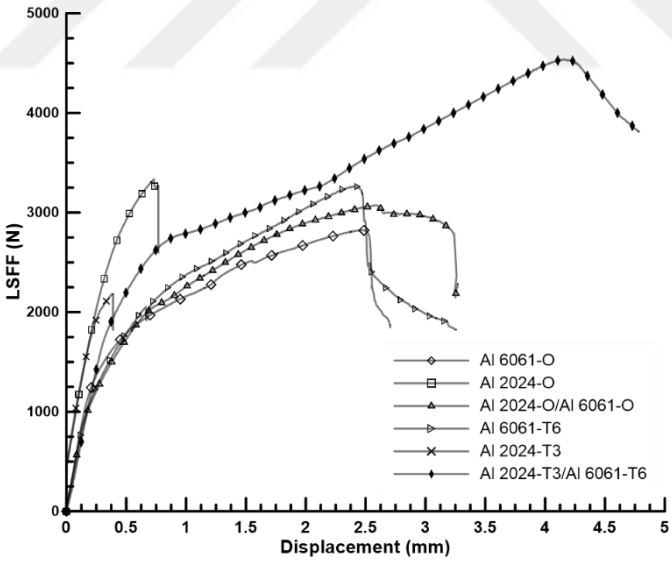

Figure 4.12 LSFF-displacement curves of the IL-FSSW welded joints

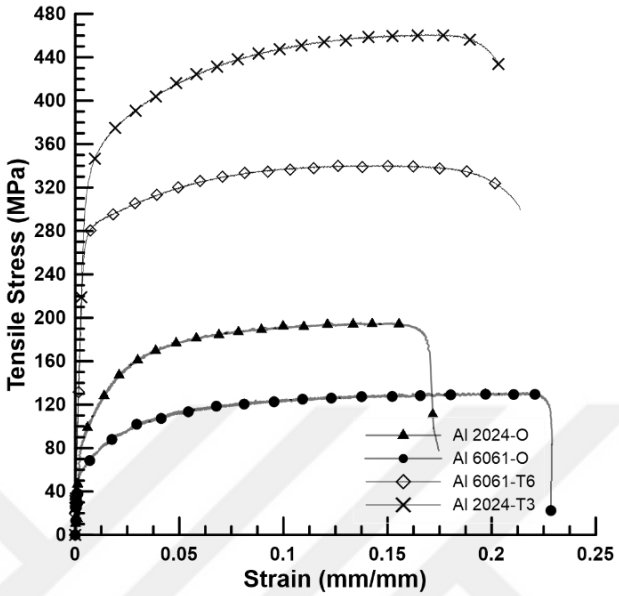

Figure 4.13 The tensile curves of the workpieces before the IL-FSSW weld processing

Table 4.1 shows the ultimate tensile strength (UTS) obtained experimentally from the tensile test of the base metals used.

Table 4.1 UTS of the base metals used

Base Metals Used	UTS (MPa)
Al 2024-T3	461.5
Al 6061-T6	340.7
Al 2024-O	195.4
Al 6061-O	131.0

Accordingly, all the welds should possess a minimum joint force where the calculation is based on the AWS standard (Equation 4.1). Comparing these values with the failure load of the IL-FSSW joints, one can make an estimation on the level of improvement

in the IL-FSSW process as a new spot-welding process. As shown in Table 4.2, the experiment values of the failure force were higher than the AWS requirement for the spot welds in the range of 1.32 -3.35 times. The Al 2024 similar welds could not possess an acceptable failure force value according to the AWS standard in a received case (T3 temper) even though it exceeded the standard value in the case of the O temper after doing the annealing heat treatment on the received sheets.

Table 4.2 Comparison of the LSFF values between the AWS standard and experimental results

The IL-FSSW welded joints	LSFF Values		Experimental/Standard
	AWS standard (N)	Experimental (N)	
Al 2024-T3, similar	3400	2184	0.64
Al 2024-O, similar	1400	3336	2.38
Al 6061-T6, similar	2480	3261.7	1.32
Al 6061-O, similar	916	2825.4	3.08
Al 2024-T3/Al 6061-T6	2480	4561	1.84
Al 2024-O/Al 6061-O	916	3073.5	3.35

Accordingly, the weld samples produced by this novel welding process exhibited considerable tensile properties when compared to the tensile result of the base metal used, excluding the Al 2024-T3 similar welds, which had a failure force value lower than the AWS requirements.

4.3 Fracture Morphology Analysis

4.3.1 Similar Welds of Al 6061

Figure 4.14 shows a close-up view of the Al 6061 fractured samples after the shear-tensile test. A mixed fracture mode of the nugget pullout and the shear fracture types was observed in the O temper sample. The failure occurred along the periphery of the spot in the upper sheet at the flash zone before going transversely through the BM, whereas for the T6 sample, the nugget pullout fracture mode was observed, the upper plate did not separate completely from the weld zone, and the nugget remained in the lower sheet.

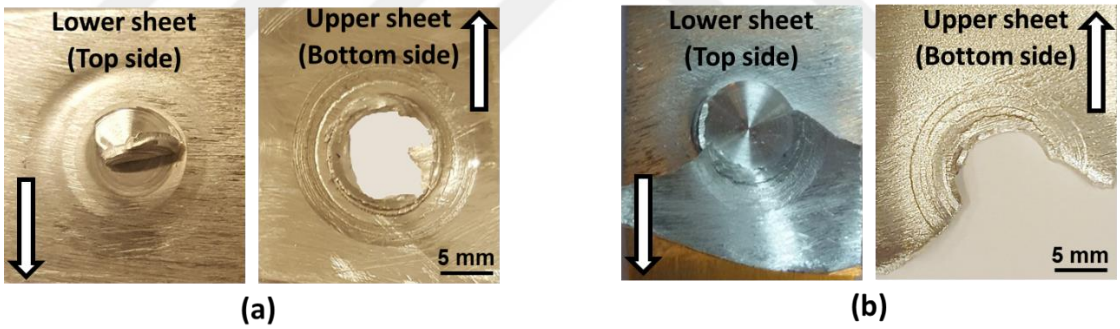

Figure 4.14 Fracture surface after the shear-tensile of the Al 6061 welded sample in (a) T6 and (b) O tempers

The T6 welded joint failed along the periphery of the IL within the TMAZ/HAZ region due to the stress concentration and low strength in this region as explained in the hardness results analysis. Before the full fracture, the weld nugget was partially peeled away revealing the interface in between. The reason for this is the presence of the kissing bond regions in the interface in between the sheets, which caused some partially welded areas in the weld nugget to remain, Figure 4.14 (a).

Based on Figure 4.14, the fracture modes indicate that better bonding is achieved in the O temper weld when compared with that of the T6 welded joint. Regardless of the workpiece temper type, it can be seen that Figure 4.14 showed excellent mixing of the upper sheet, the lower sheet, and the IL materials in the weld nugget of the welded samples.

Figure 4.15 shows a fracture morphology of the selected section of the Al 6061-O shear-tensile tested sample that was examined by the SEM. Two different regions were observed in the swirl area beneath the welding tool: a sheared unwelded region in the outer weld of the nugget (Figure 4.15(c)) and a sheared welded one in the inner of the weld nugget (Figure 4.15(d)). The unwelded region was characterized by a flat deformed area, while the sheared region was evidenced by dimples elongated in the direction of the applied load, which indicated a ductile fracture [133].

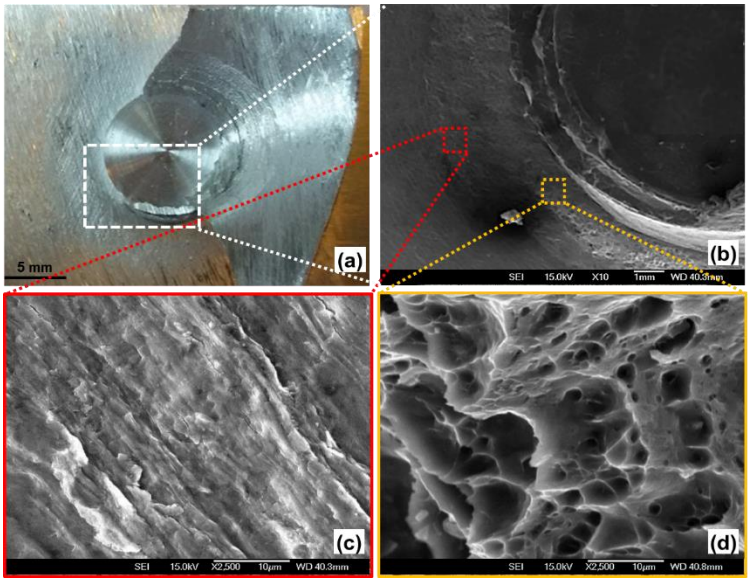

Figure 4.15 Fracture morphologies of the Al 6061-O welded joint after the shear-tensile test

The fracture surfaces examination of the Al 6061-T6 tensile tested joint is also characterized using the SEM. The SEM images are taken from the center regions of the SZ under the pulled-out weld plug of the tested sample and far from the weld center at the kissing bond regions as presented in Figures 4.16(a) and (b). As seen in Figure 4.16, the fracture is mainly trans-granular, an array of randomly fine microscopic voids and a population of varying shallow dimples are found covering the kissing bond region (Figure 4.16(d)). Consequently, the size of the dimples in the center of the fracture surface of the joint (the SZ center) was large, which suggests a large plastic zone and high ductility in the center of the SZ as shown in Figure 4.16(c) [134].

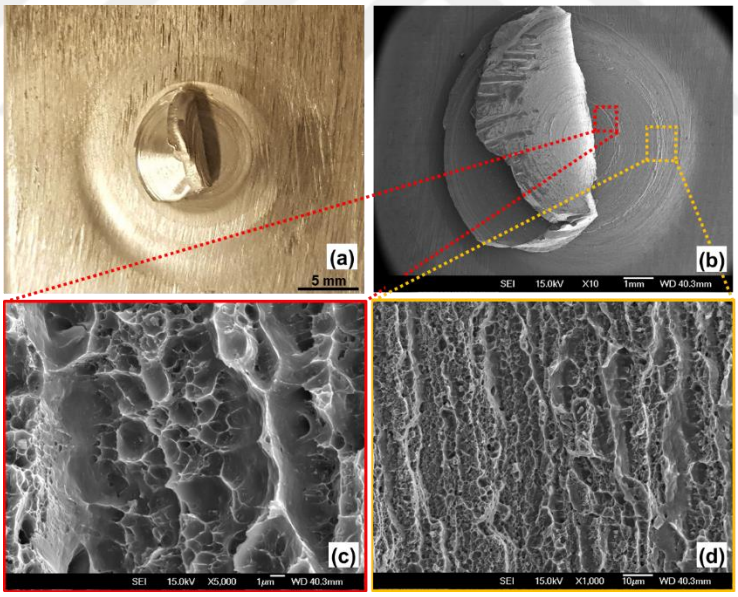

Figure 4.16 Fracture morphologies of the Al 6061-T6 welded joint after the shear-tensile test

4.3.2 Similar Welds of Al 2024

Figure 4.17 shows the fracture surfaces of the Al 2024 welded joint that failed in the shear-tensile test. It is clear from these figures that the regions underneath the tool suffered

from softening due to frictional heat and forces exerted by the rotational tool. The weld nugget suffers from severe plastic flow during the welding process, especially in the case of the O temper sample as shown in Figure 4.71(b). This swirl like pattern flow, breaks the oxide film and mixes the metals together to achieve the weld. The swirl pattern is a result of forcing the metal particles to stick to the contacted surface of the tool and rotate with it as a swirl, i.e., both the upper and lower sheets, and the IL, between the tool and the rigid anvil were sheared by the tangential reaction force exerted by the rotating action of the tool.

A shear fracture mode was observed in the fracture surfaces in both the O and T3 tempers. The failure occurred started from the sheets interfaces before going through the weld nugget before the complete separation occurs.

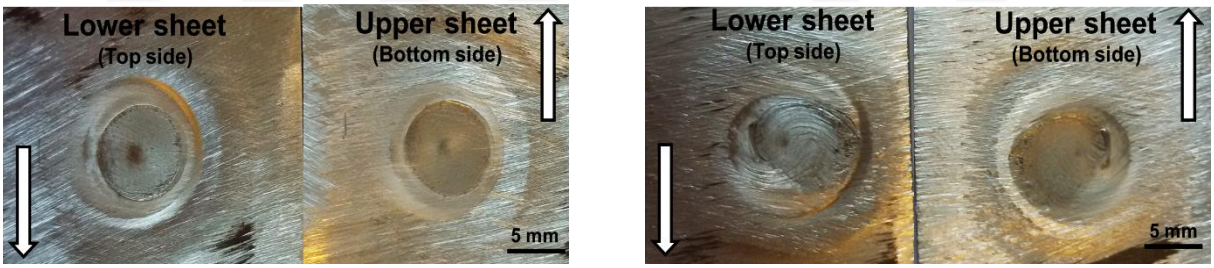

Figure 4.17 Fracture surface after the shear-tensile test of Al 2024 welded sample in (a) T3 and (b) O tempers

The SEM images of the Al 2024 sheared-tensile fracture samples revealed that the Al 2024 metal suffered from severe plastic deformation in the weld nugget verified by the swirl shape on the surfaces of the fracture as shown in Figures 4.18 and 4.19, (a) and (b). This shape was not very clear in the T3 temper Al 2024 sample when compared to the sample in the O temper due to the softening effects of the annealing treatment on the Al 2024 alloy. This swirl shape deformation is typical for the sheets welded by the IL-FSSW process, which

results from the use of the IL part, i.e. the presence of the IL makes the initial contact area smaller than the tool diameter. The contact area increased with the descending of the tool downward, and the increase in the contact area was accompanied by increasing the temperature that affected the mechanical properties of the welded sheets at the matching surfaces. This swirl flow means that the deformation and flow is transferred from the upper sheet to the lower sheet through the IL part, which diffused completely in the weld nugget.

Comparing the fractured surfaces of Al 6061 samples, a brittle fracture morphology was concluded from the fine dimples that are shown in Figures 4.18 and 4.19, (c) and (d). This is expected to be due to the hardness and low ductility of the 2024 aluminum alloy.

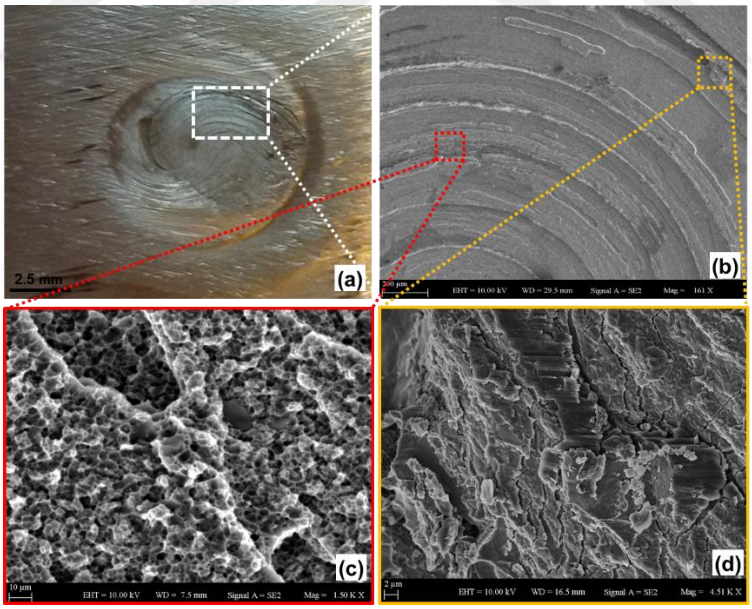

Figure 4.18 Fracture morphologies of the Al 2024-O welded joint after the shear-tensile test

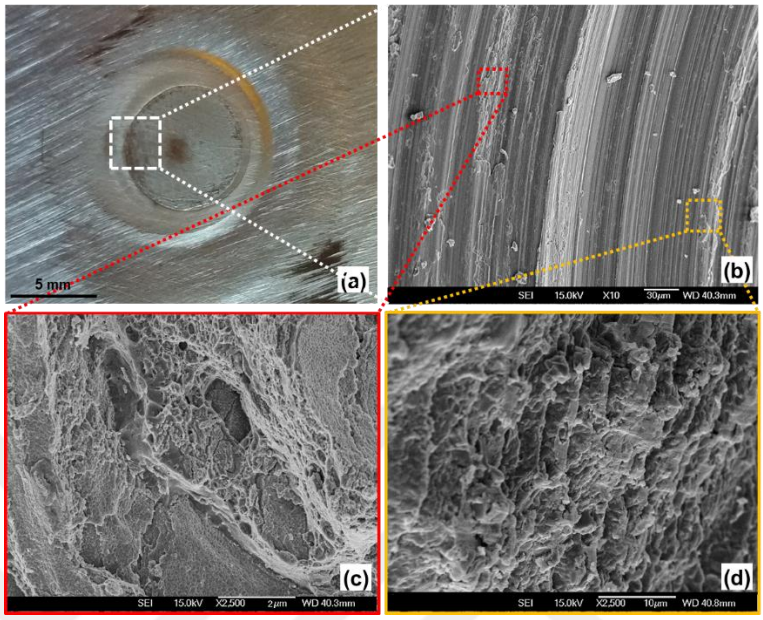

Figure 4.19 Fracture morphologies of the Al 2024-T3 welded joint after the shear-tensile test

4.3.3 Dissimilar Welds of Al 2024 to Al 6061

Figure 4.20 displays the nugget zone of the Al 2024-O to the Al6061-O welds and the fracture region at the top side of the lower sheet [129]. The failure mode appears to be of the sheet tearing-nugget pull out type, as related to better mixing between the boundaries of the materials under stirring [135]

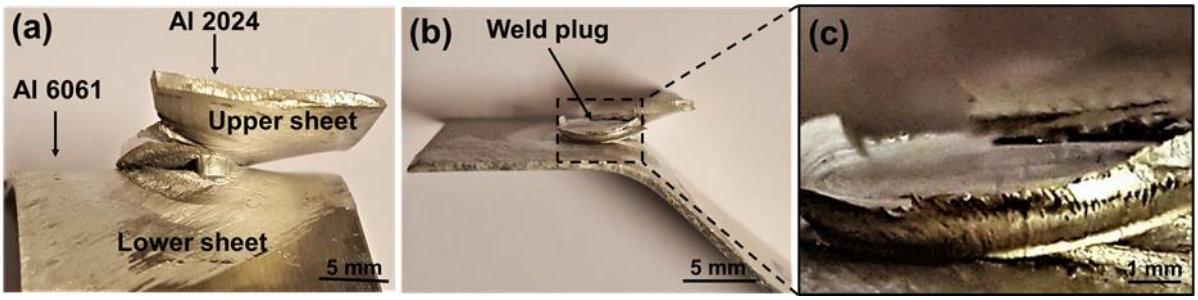

Figure 4.20 Close-up views of the fracture region in the shear-tensile welded sample of Al 2024-O/Al 6061-O [129]

The failure behavior is elaborated in more detail by examining the fracture surface morphologies from the failure regions shown in Figure 4.20 (c). Regions A to C in Figure 4.21(a) display the progress of failure [129]. Dimples of various sizes and depths can be observed at region A on Figure 4.21(b), referring to decent joint quality [72]. Elongated dimples can also be seen, which may have formed due to the movement of the interface during straining. Additionally, the weld nugget debonding is clear in this image. Region B presents larger dimples in Figure 4.21(c) indicating a ductile fracture and extensive plastic deformation [136,137]. In region C, the morphology concerning the later stage of the fracture is demonstrated. The existence of the deep dimples along with the flat-like dimples and quasi-cleavage features proposes a failure with a mixed character [115], as shown in Figure 4.21(d).

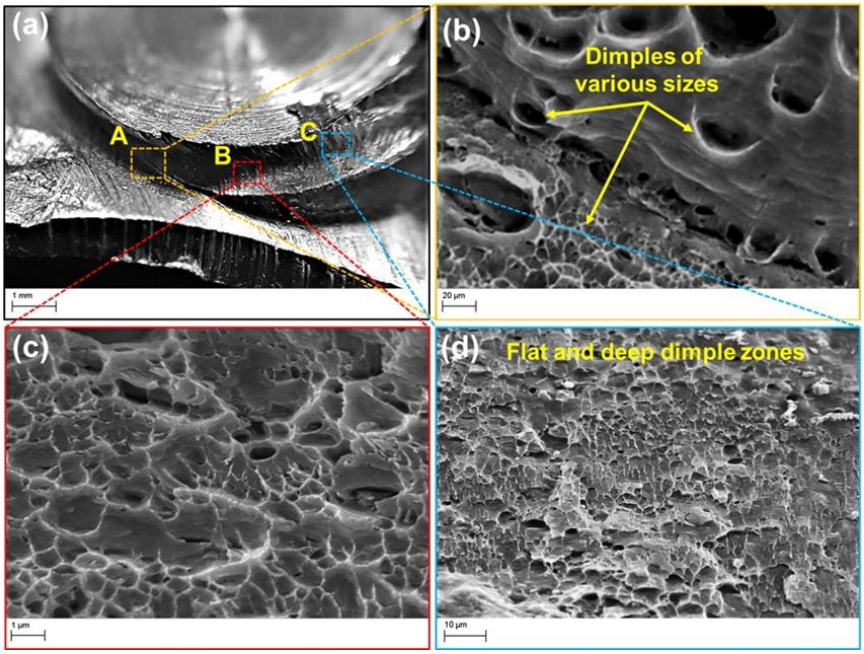

Figure 4.21 Fracture morphology appearances at selected points of failure regions [129]

The shear-tensile fracture surface of the Al 2024-T3 to the Al 6061-T6 welded joint is shown in Figure 4.22. The bottom surface of the upper sheet (Al 2024-T3) and the top

surface of the lower sheet (Al 6061-T6) complement the fracture surface, where arrows indicate the direction of the loading. Since bonding between the sheets primarily relies on the additional layer introduced, cracks propagate along the periphery located outside the IL region. After fracture, a large amount of material from the softer lower sheet adheres to the bottom surface of the harder upper sheet as indicated in Figure 4.22.

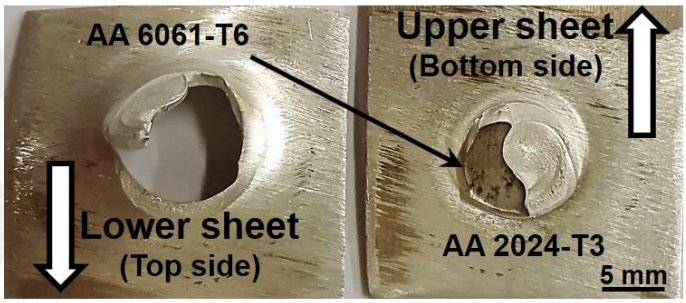

Figure 4.22 Fracture surface of the shear-tensile of the Al 2024-T3/Al 6061-T6 welded sample [131]

Further exploration of the fracture morphologies in Figure 4.22 was carried out by SEM examinations. Figure 4.23(a) demonstrates the nugget zone and the failure region at the bottom side of the upper sheet. The accumulation of the Al 6061-T6 is clearly seen here also. As indicated in Figure 4.23(b), the ductile fracture is dominant at the center since both the IL and the lower sheet are highly ductile, whereas, a mixed type fracture gradually developed at the IL interface. Outside the interface (Figure 4.23(c)), the surface contained a composite structure formed by the stirring of Al 6061-T6 and Al 2024-T3 alloys, and the latter displayed a brittle deformation. Still, the macroscopic failure behavior is mainly governed by the relatively more ductile constituents of the IL and the lower sheet. In Figure 4.23(d), the presence of numerous fine dimples reveals a shear type fracture as consistent with the ductile response.

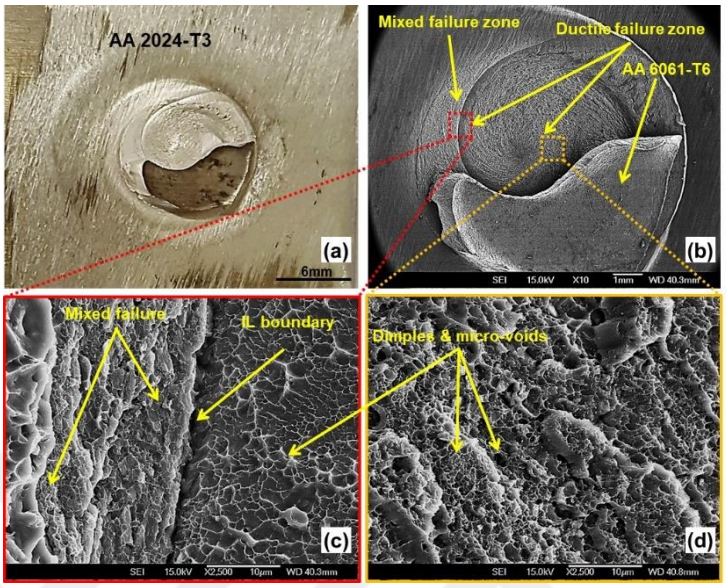

Figure 4.23 Fracture morphologies of the Al 2024-T3/Al 6061-T6 welded joint [131]

4.4 Summary on Fabrication of Al 6061 and Al 2024 Welds by IL-FSSW

All the similar and dissimilar aluminum sheets that were welded by the IL-FSSW in this work show a flat surface appearance of defect free welds with a uniform spot appearance with no keyhole achieved. The IL is affected significantly by the stirring action and tool force, it was completely transformed to form the NZ region after the hooking formation inside the upper and lower sheets. Except for the Al 2024-T3 welds, the shear-tensile tests showed that the failure forces of the welds were higher than expectable values according to the AWS standard and that most of the welded joints fractured in a ductile mode despite the existence of some partially bonded regions. The microstructure analysis observed grain refinement in the SZ of the weld's joint when compared to the grain size of the BM, which was aided by the simultaneous effects of severe plastic deformation and dynamic recrystallization. The failure analysis of the fabricated welds revealed different failure mode formations, while the fracture surfaces contained dimples in various sizes and depths.

CHAPTER V

THE FATIGUE PROPERTIES OF Al 6061 AND Al 2024 SIMILAR AND DISSIMILAR WELDS FABRICATED BY IL-FSSW PROCESS

5.1 Fatigue Test of Similar Al 6061 Welds (Group 1)

Table 5.1 shows the results obtained for the different values of the maximum load applied on similar Al 6061 welds fabricated by IL-FSSW, in terms of the number of cycles to failure.

Table 5.1 Results of fatigue testing (Group 1)

Workpieces (Treatment Condition)	*Welded Samples*	*Applied Load P_{max} (N)*	*Avg. Cycles (N_f)*
Condition 1 (as received)	Similar Al 6061-T6	2500	19,505
		2000	65,281
		1750	144,260
		1500	319,586
		1250	445,082
		1000	652,854
		500	1,448,249
Condition 2 (annealed)	Similar Al 6061-O	2500	2,755
		2000	30,763
		1250	51,598
		1500	113,902
		1250	120,568
		1000	372,627
		500	1,210,162

5.1.1 Wohler Diagram

Figure 5.1 shows the relationship between the maximum load P_{max} and N_f in the welds of Group 1 (Table 5.1)

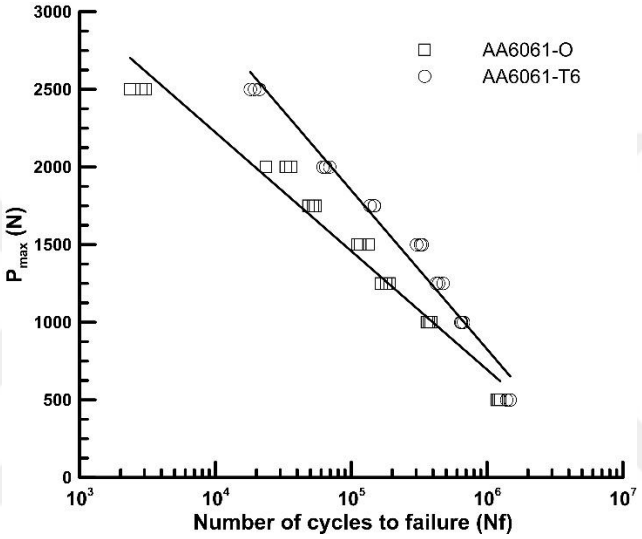

Figure 5.1 P_{max}-N_f curve of spot-welded specimens of Group 1.

From Figure 5.1, it is clear that there is no difference between the N_f of the welded specimens in conditions 1 and 2 at low load (P_{max} = 500 N), indicating that the annealing treatment has no effect on the fatigue strength at lower cyclic loads. However, there was a significant difference in N_f when seen at high load (P_{max} = 2500 N) and this difference decreased gradually with the load decreasing. This is related to the LSFF of the metals used in which the LSFF of specimens in condition 1 was 3261.7 N, which is much more than the high load (2500 N) applied in fatigue test, whereas for the specimens in condition 2, the LSFF was 2825.4 N, which is near to 2500 N applied on the specimens in condition 2, and this tends to decrease in the fatigue life of the specimens in condition 2 when compared with the specimens in condition 1.

5.1.2 Appearance of Fracture

Typical fracture surfaces of the welds in Group 1 tested at P_{max} both 2500 N and 500 N are revealed in Figure 5.2 and Figure 5.3. The fatigue crack grew into the upper sheet at a high applied load (P_{max} = 2500 N) (Figures 5.2 and 5.3(a)), and the final fracture occurred due to the fatigue crack growth around the nugget irrelevant to the applied load direction. This final fracture, which was caused by the pull out of the nugget, could be denoted as a plug type fracture [51].

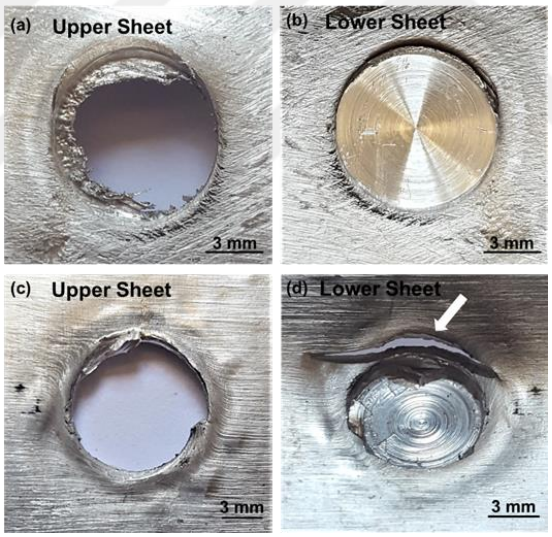

Figure 5.2 Macroscopic appearance of fatigue-fractured specimens (Group 1, condition 1): (a) and (b) fracture surfaces at P_{max} = 2500 N observed on the upper and lower sheets (bottom and top view), (c) and (d) at P_{max} = 500 N, respectively, The loading direction vertical

When the applied load is low, the fatigue crack is initiated in the lower sheet as indicated by the arrows in Figures 5.2 and 5.3(d). As can be understood from the photograph of the fracture surface obliquely from the above, it can be clearly observed that the crack has propagated circumferentially around the nugget and that most of the nugget remains in the lower sheet.

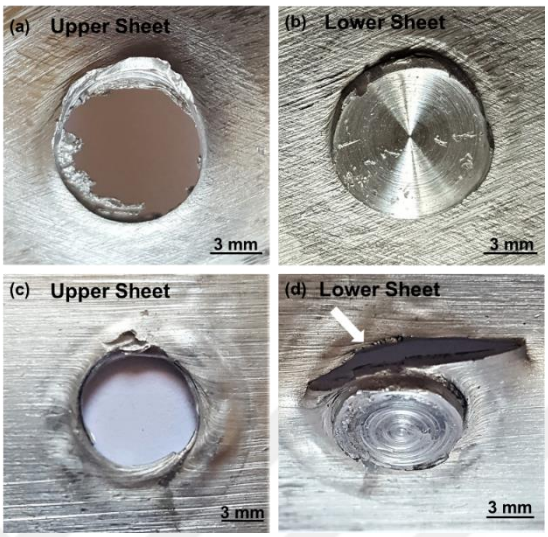

Figure 5.3 Macroscopic appearance of fatigue-fractured specimens (Group 1, condition 2): (a), (b) fracture surfaces at P_{max} = 2500 N observed on the upper and lower sheets (bottom and top view), (c) and (d) at P_{max} = 500N, respectively. The loading direction is vertical

This explains that the fatigue failure was caused by the crack initiation in the TMAZ and HAZ due to the significant microstructural changes and the lower hardness in these regions before it propagates along the bonding ligament what is called, shear-plug fracture mode [135]. In the end, the upper and lower sheets were sheared off from each other, which was similar to that static fracture of the specimens in condition 1 (shear-tensile test). As shown in the close-up views in Figures 5.2 and 5.3, the crack was initiated at the boundary between the upper and lower sheets in the joint region due to the stress concentration and tended to grow through the upper sheet under fatigue loading. Since this plug type fracture is mostly governed by the thickness of the upper sheet, the increase of the effective cross-sectional area of the nugget, which was considered as one of benefits of the IL-FSSW process, shows its effectiveness. Therefore, the similarity of the N_f of joints in both conditions 1 and 2, at low applied loads could be attributed to the similar crack growth direction and

crack length of both joints at the low applied load (P_{max} = 500 N) as shown in Figures 5.2 and 5.3(d).

Figure 5.4 and Figure 5.5 imply the SEM micrographs of the fracture surface observed in the upper sheet of the Al 6061 joints in the as-weld metal (condition 1) and annealed metal (condition 2), respectively, where P_{max} = 500 N. From Figures 5.4 and 5.5(a) it can be observed that the crack had propagated circumferentially around the nugget. It can also be observed from both that most of the nugget remains in the lower sheet. The enlargements of the points indicated by arrows B–E in Figure 5.4(a) are given in Figure 5.4(b) – (e). The typical fatigue fracture surfaces with striation such as the patterns that are seen at spots B, C and D, while the static fracture surface with dimples was recognized at spot E. The presence of the signs of the fatigue striations that spread in several directions in Figure 5.4(b) – (d) are probably due to the local stress state changes. The crack initiated at the boundary between the upper and lower sheets, at the edge of the nugget, and grew in the direction parallel to the loading direction through SZ as shown by the arrows in Figure 5.4(a).

Figure 5.5 shows the SEM micrographs of the fracture surface observed on the upper sheet of the Al 6061 joint in condition 2, where P_{max} = 500 N. Figure 5.5(b) – (e) are the magnified views at the spots B–E in Figure 5.5(a), respectively. It is clear from the figures that B, C, and D that the striated fracture surfaces and the spot E is a static fracture surface. As that in condition 1 case, the crack initiated at the boundary between the upper and lower sheets and grew through the upper sheet.

It should be noted that the growth of the fatigue crack moves away from the SZ center with the increasing applied load. Based on these findings, it is believed that crack initiated at the IL boundary and grew around the nugget, which finally led to the plug-off fracture type and that most of the nugget remains in the lower sheet. Additionally, there were no observable changes in the fracture mechanism due to the annealing.

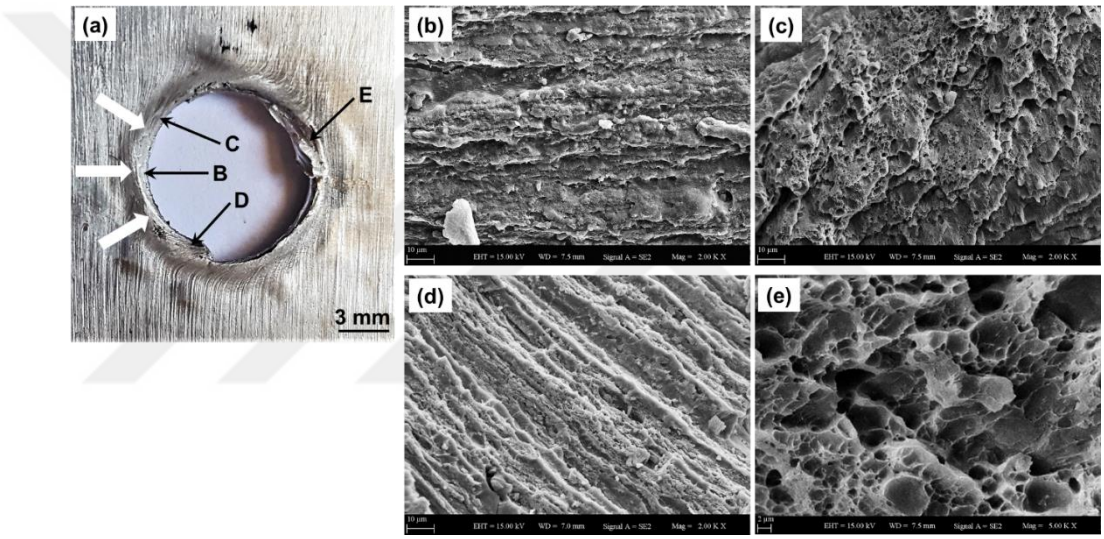

Figure 5.4 SEM of fracture surfaces (Group 1, condition 1), upper sheet: (a) P_{max} = 500 N and $N_f = 1.44 \times 10^6$ and (b – e) magnified views at spots B–E in (a), respectively. The loading direction is horizontal

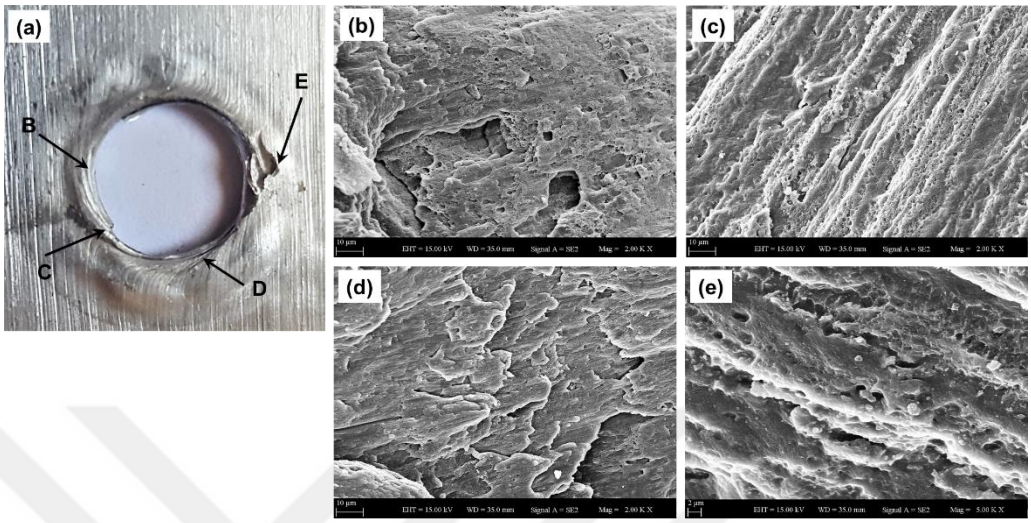

Figure 5.5 SEM of fracture surfaces (Group 1, condition 2), upper sheet: (a) P_{max} = 500 N and $N_f = 1.21 \times 10^6$ and (b – e) magnified views at spots B–E in (a), respectively. The loading direction is horizontal

5.1.3 Fracture Morphology

Figure 5.6 shows the schematic illustrations of the fracture morphology of the welds in group 1 under the fatigue conditions, based on the macroscopic and microscopic appearance of the fracture. At the P_{max} = 2500 N applied load, the fracture mode was the plug type. At a low load applied (P_{max} = 500 N), the fracture mode was the shear-plug type. The crack mainly propagates along two paths: one at lower point of the nugget through the BM of the lower sheet, perpendicular on the load direction, and the other is starting from the TMAZ weld region through the perimeter of weld plug on the upper sheet.

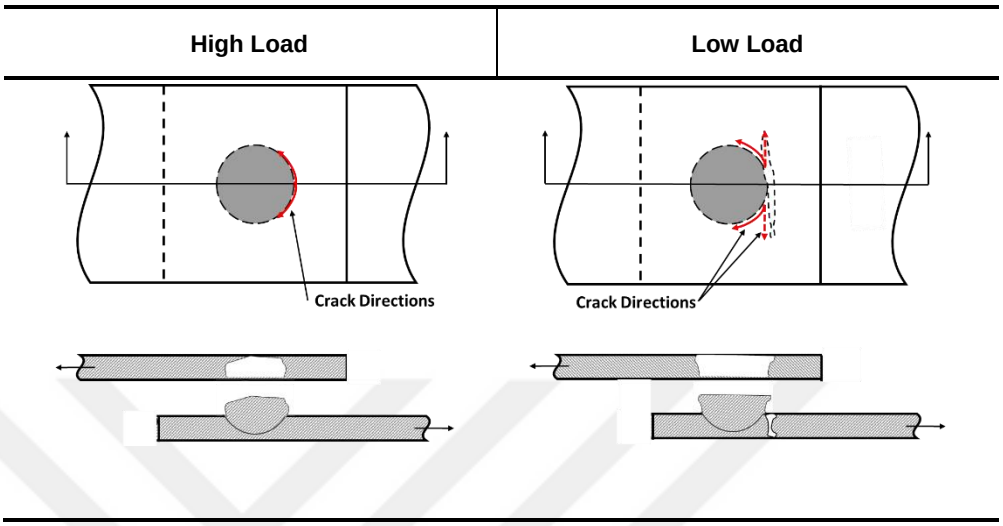

Figure 5.6 Illustrations of the fatigue fracture morphology (Group 1).

5.2 Fatigue Test of Similar Al 2024 Welds (Group 2)

Table 5.2 shows the results obtained for the different values of the maximum load applied on similar Al 2024 welds fabricated by the IL-FSSW, in terms of the number of cycles to failure.

Table 5.2 Results of fatigue testing (Group 2)

Workpieces (Treatment Condition)	*Welded Samples*	*Applied Load P_{max} (N)*	*Avg. Cycles (N_f)*
Condition 1 (as received)	Similar Al 2024-T3	2500	48
		2000	458
		1750	1,966
		1500	7,137
		1250	9,486
		1000	18,052
		500	150,241

Condition 2 (annealed)	Similar Al 2024-O	2500	2,757
		2000	23,850
		1750	48,155
		1500	125,262
		1250	217,607
		1000	448,120
		500	942,010

5.2.1 Wohler Diagram

Figure 5.7 shows the relationship between the maximum load P_{max} and N_f in the welds of group 2 (Table 5.2). The dashed line represents the transition of the fatigue crack growth behaviors from the low cycle to the high cycle fatigue [138]. As seen from Figure 5.7, most of the fatigue results of the samples under condition 1 failed at the low cycle zone, and the reason for that was the properties of the Al 2024-T3 (condition 1), which is harden alloy, and has poor weldability properties. The welds made by the specimens in condition 2 were much stronger. Among all the welds, the welds in condition 2 had the highest N_f of 9.3×10^5 at a low applied load (P_{max} = 500 N), indicating that the annealing treatment had a good enhancement effect on the fatigue strength. This fact is identical to the shear-tensile test results, in which there was a clear enhancement of the LSFF values of the welded joints of this alloy in condition 2 when compared with that in condition 1. Comparing the results of group 2 with that of groups 1 and 3, the results of the welds in group 2 showed a lower N_f among all the groups due to the hardness and the low weldability of this type of alloys (Al 2024-T3).

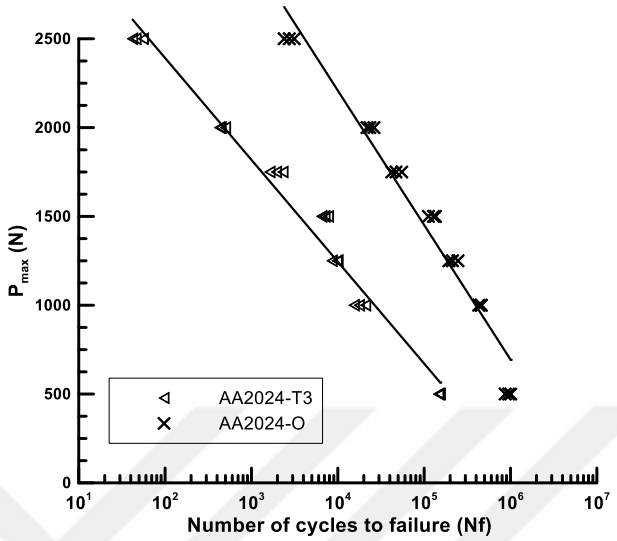

Figure 5.7 P_{max}-N_f curve of spot-welded specimens of group 2

5.2.2 Appearance of Fracture

Based on the experimental results, the failed spot friction welds under the cyclic loading conditions show one failure mode as seen in the close-up views in Figure 5.8 and Figure 5.9. The weld samples failed with the nugget shear fracture. However, other than the shear cracks, even transverse cracks can also be seen from the lower plate as indicated by the arrows in Figures 5.8 and 5.9(d). However, failure occurs only because of the shear cracks and not because of the transverse cracks. The shear fracture was observed at all the loads applied. In the shear fracture, the material gets sheared off at the periphery of the nugget as shown in the group 2 specimens (Figures 5.8 and 5.9). This type of fracture is observed due to the insufficient material mixing at the center through the stirring action. The crack propagated through the SZ, and some part of the nugget remained in the lower and upper sheets. From Figures 5.8 and 5.9, it can be clearly observed that the mixing effect of all the upper, lower sheets, and IL is very clear in the condition 2 welds. This indicates that better

bonding is achieved in condition 2, Figure 5.8, when compared to the condition 1, Figure 5.9. Hence, it can be considered that the weld joints made by the condition 2 specimens had better fatigue strength than those made by the condition 1 specimen.

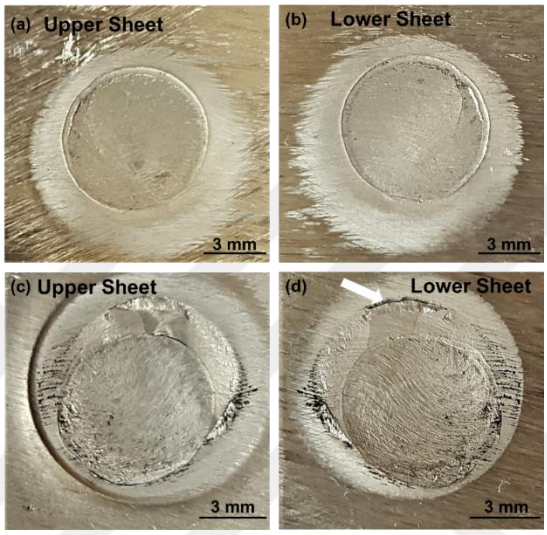

Figure 5.8 Macroscopic appearance of fatigue-fractured specimens (Group 2, condition 1) which observed on the upper and lower sheets (bottom and top view), respectively): (a) and (b) at P_{max} = 2000 N, (c) and (d) at P_{max} = 500 N. The loading direction is vertical

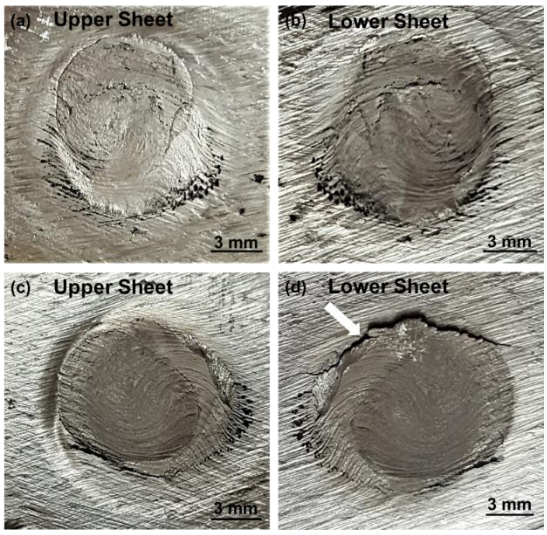

Figure 5.9 Macroscopic appearance of fatigue-fractured specimens (Group 2, condition 2) which observed on the upper and lower sheets (bottom and top view), respectively): (a) and (b) at P_{max} = 2500 N, (c) and (d) at P_{max} = 500 N. The loading direction is vertical

Figure 5.10 indicates the SEM images of the fractured surface observed on the lower sheet of the IL-FSSW welds made of Al 2024-T3 (condition 1). Figure 5.10(b) – (d) shows the magnified views of spots B–D in Figure 5.10(a) respectively. Spots B and C share some similarities in the fracture mechanism, which occurred due to cleavage fracture accompanied by the microscopic traces of the local plastic deformation. The cleavage fracture represents a quasi-brittle component of the fracture process. The quasi-brittle fracture morphology consists of a mixture of intergranular facets and transgranular cleavage. A static fracture surface with dimples is recognized at spot D. This indicates that the crack grew around the nugget at the sheets interface, and the final fracture occurred at spot D.

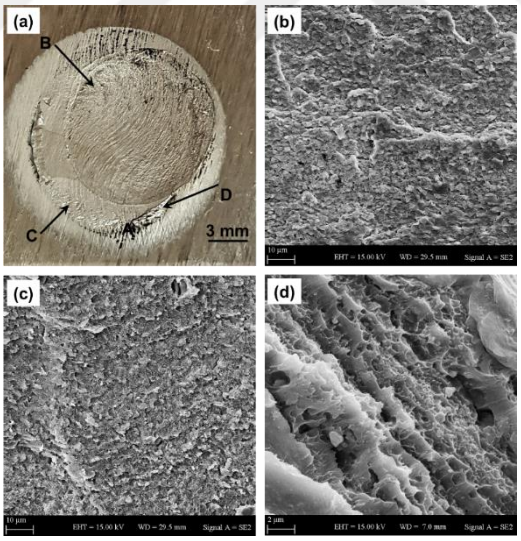

Figure 5.10 SEM of fracture surfaces (Group 2, condition 1), lower sheet: (a) P_{max} = 500 N and $N_f = 1.5 \times 10^5$ and (b – d) magnified views at spots B–D in (a), respectively. The loading direction is horizontal

Figure 5.11 shows the SEM images of the fatigue fracture surface observed on the lower sheets of the group 2 weld specimens in condition 2, where the P_{max} is 500 N. Figure 5.11(b) – (d) shows the magnified views of the spots B-D in (a) respectively. The first crack

initiated near the boundary of the SZ and propagated until the end of the fracture. The second crack then originated from the crack tips along the periphery of the nugget zone at the sheets interface, and finally, the lower sheet was torn off with some transvers cracks near the nugget. The close-up view of spots B and C shows signs of cleavage fracture with the particularity that the cracks propagated in different planes and a scarce intergranular fracture occurred. They also composed of a dimpled surface, although there were signs of a local cleavage fracture. This observation of the presence of a mixed dimpled and intergranular fracture surface suggested that not only a ductile fracture occurred in this region, but also a localized brittle failure [139].

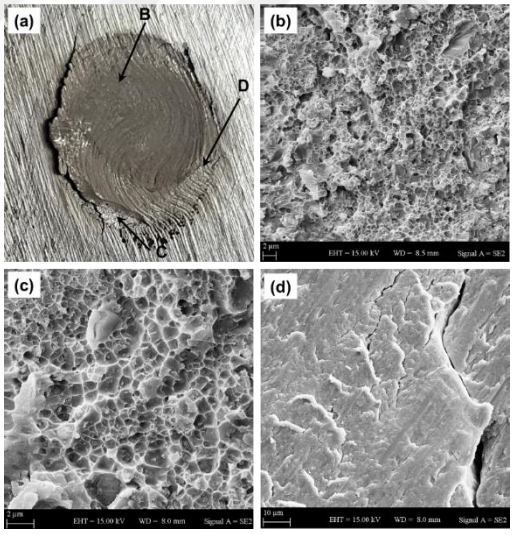

Figure 5.11 SEM of fracture surfaces (Group 2, condition 2), lower sheet: (a) P_{max} = 500 N and $N_f = 9.4 \times 10^5$ and (b – d) magnified views at spots B–D in (a), respectively. The loading direction is horizontal

5.2.3 Fracture Morphology

Figure 5.12 shows the schematic representation of the fracture morphology of the group 2 welded joints under low and high cycle loading conditions, based on the macroscopic

and microscopic appearance of the fracture. Under the high cycle loading, the welded samples failed by shear mode only, and no transverse cracks could be seen. Under low cycle loading, the cracks tip originates from the sheets interface near the nugget and propagates in two directions; one along the joint interface through the SZ, and the other transversally, with a little distance into the lower sheet before the upper and lower sheets sheared off from each other. However, failure occurs only because of the shear cracks and not because of the transverse cracks.

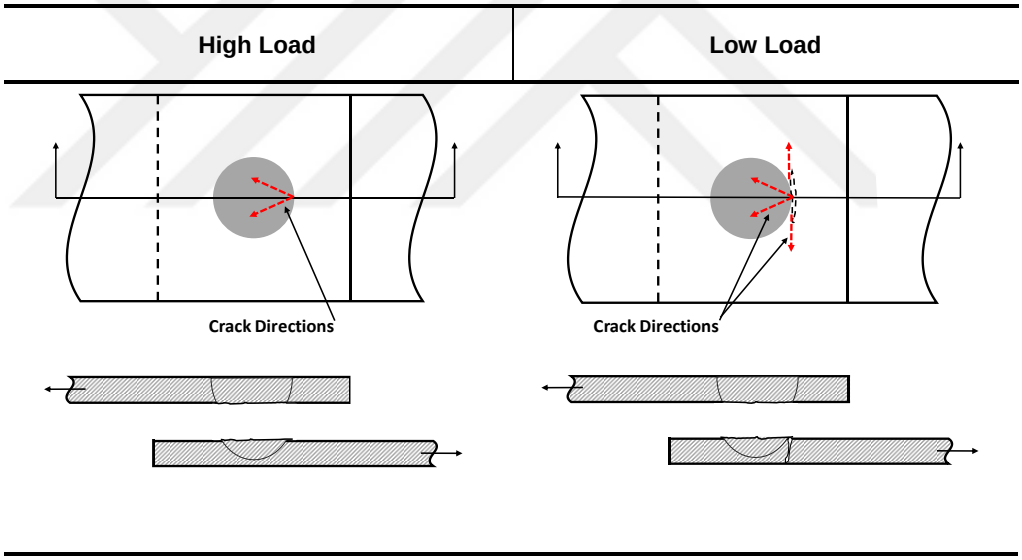

Figure 5.12 Illustrations of the fatigue fracture morphology (Group 2)

5.3 Fatigue Test of Dissimilar Al 2024/Al 6061 Welds (Group 3)

Table 5.3 shows the results obtained for the different values of the maximum load applied on the dissimilar Al 6061/Al 2024 welds fabricated by the IL-FSSW in terms of the number of cycles to failure.

Table 5.3 Results of fatigue testing (Group 3)

Workpieces (Treatment Condition)	*Welded Samples*	*Applied Load P_{max} (N)*	*Avg. Cycles (N_f)*
Condition 1 (as received)	Dissimilar Al 6061-T6 to Al 2024-T3	2500	92,893
		2000	293,595
		1750	347,512
		1500	638,773
		1250	749,287
		1000	953,020
		500	1,704,873
Condition 2 (annealed)	Dissimilar Al 6061-O to Al 2024-O	2500	13,724
		2000	53,942
		1750	108,490
		1500	236,201
		1250	332,045
		1000	601,844
		500	1,058,612

5.3.1 Wohler Diagram

Figure 5.13 shows the relationship between the maximum load P_{max} and N_f in the welds of Group 3 (Table 5.3).

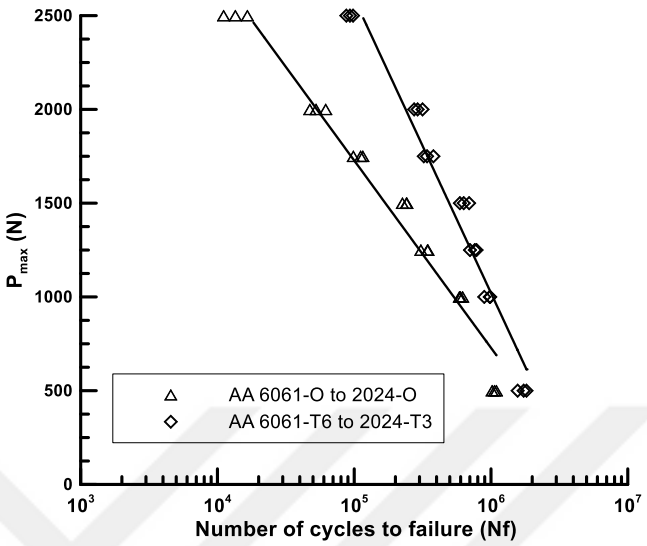

Figure 5.13 P_{max}-N_f curve of spot-welded specimens of Group 3

Although the fatigue strengths of both treatment conditions, 1 and 2, are almost the same at low applied loads (P_{max} = 500 N), it was higher for the specimens of condition 1 than that in condition 2 at the high applied load (P_{max} = 2500 N). Similar to the group 1 results, it should be noted that the joint with condition 1, which has higher tensile strength, had high fatigue strength at low applied loads, which is discussed in section 5.1.1.

5.3.2 Appearance of Fracture

There were some differences in the fracture appearance, and load dependence was noted for the conditions 1 and 2 fatigue specimens. Figures 5.14 and 5.15 show close-up views of the macroscopic appearance of the fractures in the joints under a high (P_{max} = 2500 N) and low (P_{max} = 500 N) loads. Under a high load, it is clear from the fracture surfaces on the upper and lower sheets that there is no difference in the fracture mechanism between condition 1 (Figure 5.14(a) and (b)) and condition 2 (Figure 5.15 (a) and (b)), and the dominated fracture mode that occurred was a shear mode in the SZ in each case. In Figures

5.14 and 5.15, the loading direction is horizontal. As shown, the opened part indicated by the white arrow was formed by deformation. This opening occurred along the lower sheet boundary surface. Here, the alloy type of the lower sheets is Al 6061, which is softer than the upper sheets alloy (Al 2024), and since the strength of the sheets is nonequivalent, the load causes an opening to be made just in the lower sheets.

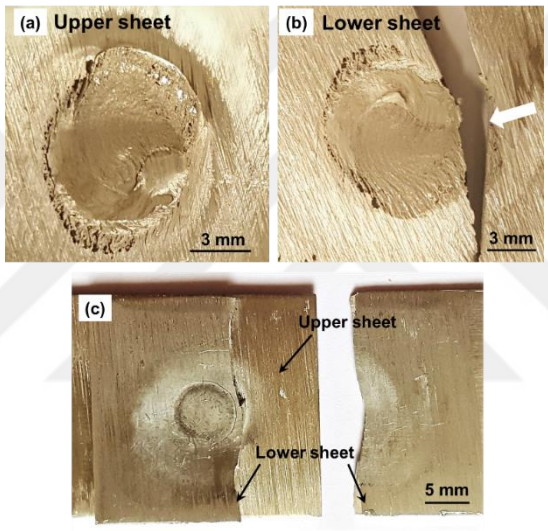

Figure 5.14 Macroscopic appearance of fatigue-fractured specimens (Group 3, condition 1): (a), (b) fracture surfaces at P_{max} = 2500N observed on the upper and lower sheets (bottom and top view), respectively, (c) P_{max} = 500N. The loading direction is horizontal

Under the low load, on the other hand, the fracture occurred in all the cases out of the NZ in the BM of the sheets. The final fracture occurred in the lower sheets of the metal (Al 6061) in both conditions 1 and 2 (Figures 5.14 and 5.15(c)). The reason is, the comparison between 2024 and 6061 aluminum alloys, the Al 2024 sheets can withstand higher loads at a low cycle fatigue.

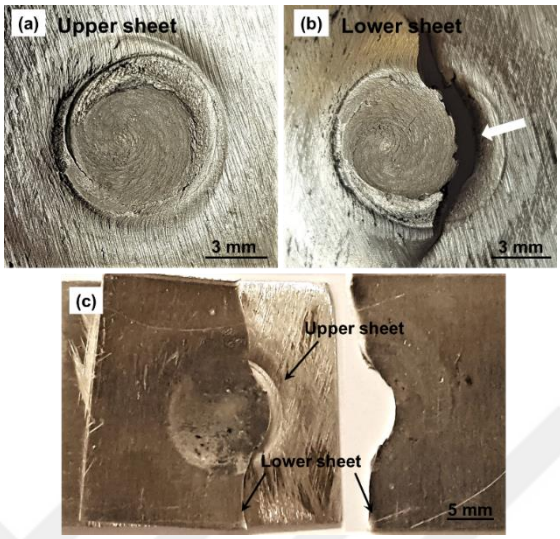

Figure 5.15 Macroscopic appearance of fatigue-fractured specimens (Group 3, condition 2): (a), (b) fracture surfaces at P_{max} = 2500 N observed on the upper and lower sheets (bottom and top view), respectively, (c) P_{max} = 500N. The loading direction is horizontal

Figure 5.16 shows the SEM micrographs of the fatigue fracture surface of the welds in group 3, condition 1 under low load (P_{max} = 500 N). Figure 5.16(a) shows the close-up photograph of the fracture cross-section surface. Figure 5.16(b) and (d) are the magnified views of spots B, D indicated by the arrows in (a) and spot C indicated by the arrows in (b). Figure 5.16(b) is thought to be the points of the cracking initiation, which occurred on the top side of the lower sheet. As is clear in (d), it reveals the V shape fracture area, each side of a 45° inclination from the plane of the load, which indicates failure due to severe plastic deformation [140]. Also, this is clearly the development of the crack in the transverse direction across the thickness of the sheet (lower sheet). Figure 5.16(c) represents the magnified view of spot C in (b), and is composed of dimples. It is probable that this was the remaining region before catastrophic failure occurred. Still, it happened in a ductile manner.

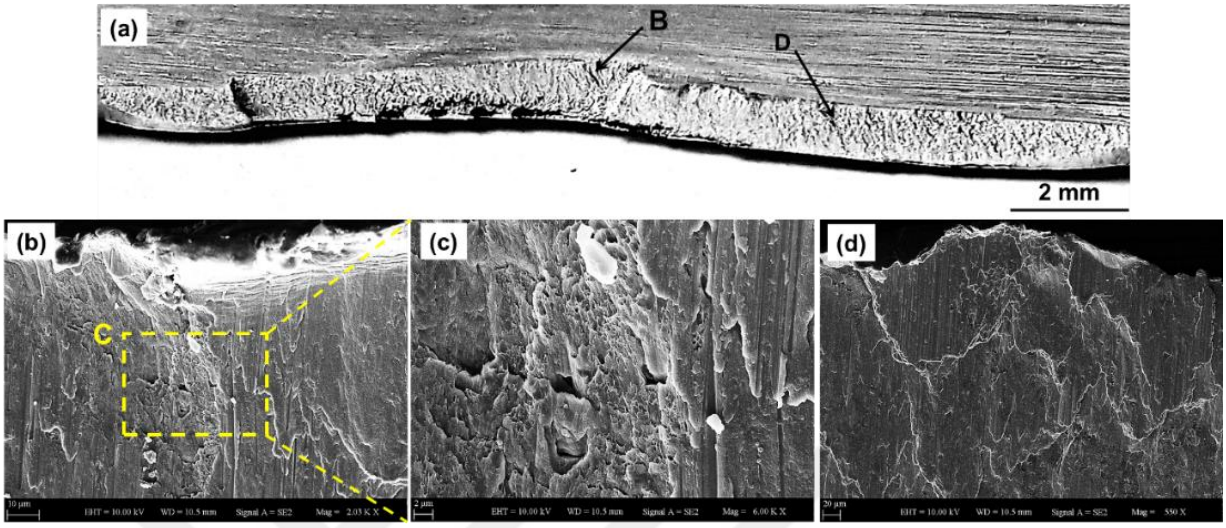

Figure 5.16 SEM of fracture surfaces (Group 3, condition 1), lower sheet: (a) P_{max} = 500 N and N_f = 1.7 × 10^6 and (b – d) magnified views at spots B, D in (a) and point C in (b), respectively

Figure 5.17 shows the fracture surface under a low load (P_{max} = 500 N) in condition 2. As in condition 1, the fracture in condition 2 occurred in the lower sheet. Figure 5.17(a) shows the surface of a fracture in the BM and Figure 5.17(b)-(d) is the enlarged views of the locations B, C, and D indicated by arrows in (a). Figure 5.17(b) is the point of the cracking initiation and Figure 5.17(c) and (d) shows the clear striation, confirming that the development of the crack is the same as in the case of the condition 1 metal.

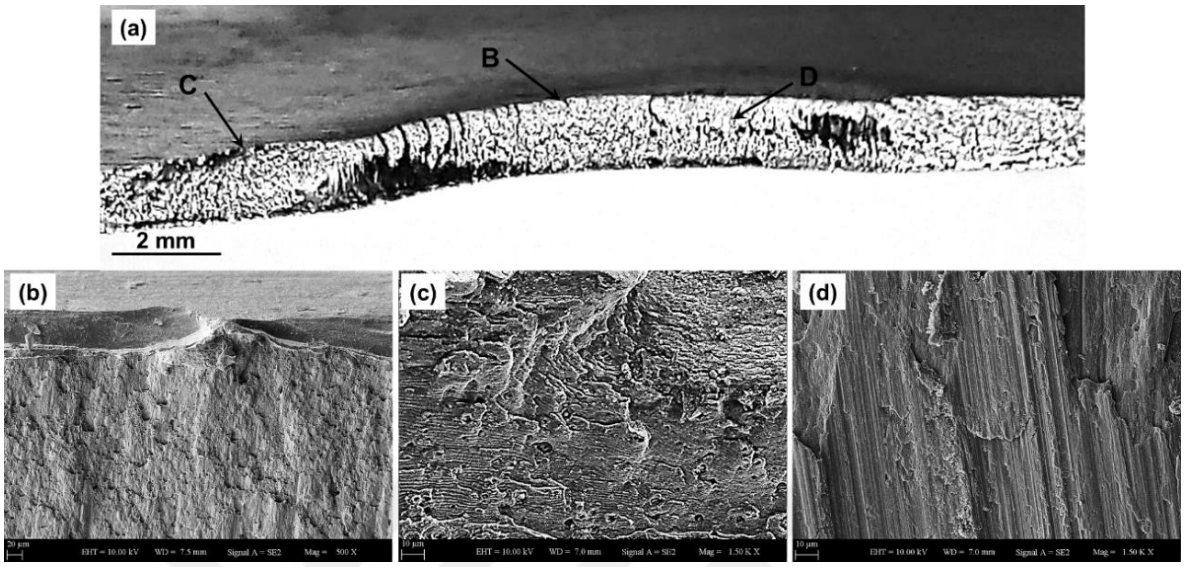

Figure 5.17 SEM of fracture surfaces (Group 3, condition 2), lower sheet: (a) P_{max} = 500 N and $N_f = 1.05 \times 10^6$ and (b – d) magnified views at spots B–D in (a), respectively

5.3.3 Fracture Morphology

Figure 5.18 shows the schematic illustrations of the fracture morphology of the welded joints under fatigue conditions and their load dependency based on the macroscopic and microscopic appearance of the fracture. When the high load applied, the fracture mode was shear through the weld nugget in addition to the tearing fracture in the BM of the lower sheet. The crack mainly propagates along two paths: one is along the sheet's interface through the weld nugget along the stretch side with load direction, and the other is through the BM of the lower sheet. As the low load applied, the crack was probably starting at the SZ/TMAZ interface and propagate transversely through the BM of the lower sheet.

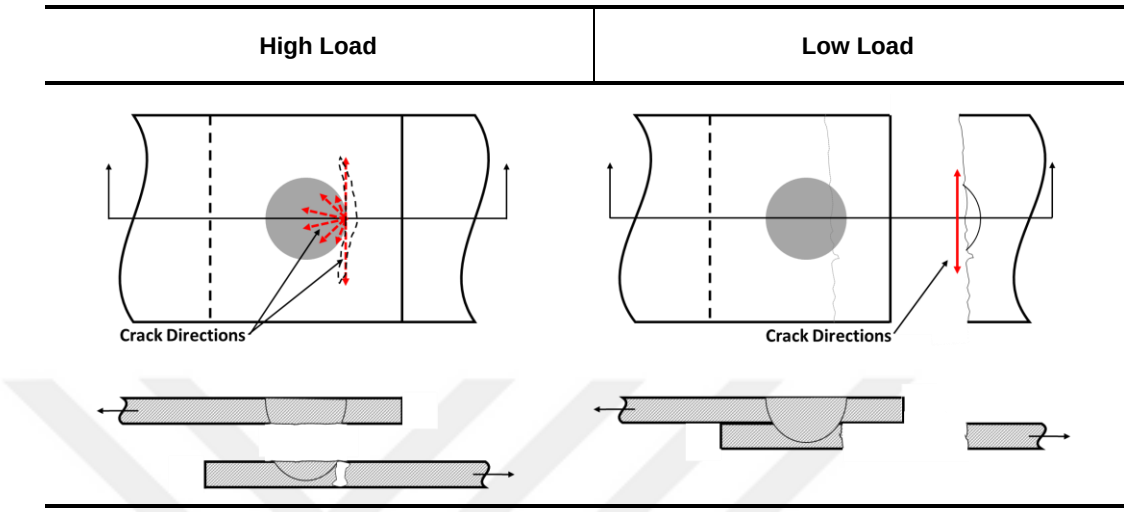

Figure 5.18 Illustrations of the fatigue fracture morphology (Group 3)

5.4 Summary of Fatigue Test

In each groups weld, the fracture morphology was different. In the groups themselves, the fracture morphologies were similar in each of the metal conditions (1 and 2), except in group 3. The load dependency of the fracture morphology may be considered to be as follows. The bonding at the boundary interface between the upper and lower sheets is adequate. Except group 2, herein separation occurs at a relatively early stage of load repetition along the boundary interface, especially in condition 1 (Figure 5.7). In terms of the load dependency of the fracture configuration, the fracture that occurs in the joint under high load is affected by heat treatments. In all groups, the annealing treatment was observed to have a negative effect on the N_f. However, no heat treatment effect was observed under low load levels, except in group 2, where the annealing had a positive effect on the N_f. The heat input and residual strain during the welding were different in the upper and lower sheets, which made the upper sheet harder near the nugget. This explains that the openings were formed near the boundary of the weld nugget in all groups of the welds.

CHAPTER VI

THE THERMAL AND MECHANICAL MODELS OF SIMILAR AND DISSIMILAR WELDS FABRICATED BY THE IL-FSSW PROCESS

6.1 Coupled-Field Analysis

The main objective of the numerical analysis in this chapter is simulating the temperature distribution and the joint mechanical properties during the IL-FSSW welding process and comparing the simulation results with the data measured experimentally during the weld processing.

When an engineering problem to be analyzed and simulated contains two or more physical phenomena coupled together, the coupled-field finite element method is a powerful technique that can be used. There are several examples of coupled-field problems such as electrical field interacting with a magnetic field, a magnetic field producing structural forces, and a temperature field affecting the fluid flow [141].

There are two ways to solve such problems, either by solving the problem as a single field problem and applying the result as a load into another field problem, or, by using an element which can work with both problems. ANSYS 18.2 software has some elements such as SOLID 98 and SOLID 226, which can be used for the thermal and structural degrees of freedom [142,143].

6.2 The IL-FSSW Developed Models

The temperature distributions and joint strength during the IL-FSSW process were investigated by finite element simulations. A nonlinear, transient three-dimensional heat transfer model was developed to determine the temperature distribution of similar and dissimilar welds of Al 6061-T6 and Al 2024-T3 to Al 6061-T6, respectively. Moreover, the joint strength and the behavior of the weld through shear-tensile test were also investigated for different welds. The finite element models were parametrically built using Ansys Parametric Design Language (APDL) provided by ANSYS 18.2. In order to validate the developed model, the output of these models was compared with the experimental data.

6.2.1 The Model Analysis

A three-dimensional transient finite element model was developed to simulate the IL-FSSW process for the similar Al 6061-T6 and dissimilar Al 2024-T3 to Al6061-T6 sheets.

For thermal analysis, as a first step, the transient temperature field (T) which is a function of time (t) and the spatial coordinates (x,y,z), were solved [144].

$$\frac{\partial}{\partial x}\left(k\left(\frac{\partial T}{\partial x}+\frac{\partial T}{\partial y}+\frac{\partial T}{\partial z}\right)\right)+\mathrm{Q}_{\mathrm{int}}=\rho c\frac{\partial T}{\partial t} \quad \text{.....(6.1)}$$

where,

ρ Density, kg/m,

c Specific heat J/kg K,

k Thermal conductivity along x, y, and z directions, W/mK,

T Absolute temperature, K,

Q_{int} internal heat source (heat generation).

The modeling of the heat evolution between the welding tool (stationary heat source) and the metal sheets is an important step in order to understand how heat is affecting the material flow and microstructure modification within and surrounding the welding region. To compensate for the lack of a predicted temperature field, the measured temperature values from the experimental tests were used to construct an approximate temperature field of the process [93,145].

Regards to mechanical analysis, the results of the mechanical tests obtained experimentally were used to calibrate and validate a numerical model that was used to predict the welds strength and failure mode. The model reproduced the specimen geometry and load conditions adopted in the shear-tensile test. The joint was considered as being formed by three main regions that were explained in chapter IV (SZ, TMAZ, and HAZ), whose properties and dimensions were based in microhardness evaluation and macrographic analysis of welded samples.

6.2.2 Assumptions

The modeling of the actual physical phenomena of the IL-FSSW process is rather complicated. Therefore, several simplifying assumptions were made.

1. The material of the workpiece is isotropic and homogeneous.

2. The workpieces are assumed to obey the BISO (bilinear isotropic) model.

3. No melting occurs for any part during the weld processing.

4. The thermal boundary conditions are symmetrical across the spot weld centerline.

5. The initial temperature is assumed to be 41 °C.

6. It is assumed 80% of the dissipated energy that is caused by the friction effect is transformed into heat.

7. The tool, upper clamping disc, and the rigid anvil are assumed rigid and no deformation occurs in these parts.

8. The SZ diameter will depend only on tool diameter and the variant of the process chosen. Since tools of different diameters can be adjusted and no traverse movement is possible through the IL-FSSW process.

9. The mechanical model was developed considering the tool diameter and sheets' configuration actually used in mechanical tests.

10. Since no mechanical test data on the properties of the SZ, TMAZ, and HAZ regions were available, the hardness profiles of an actual welded sample using the optimum welding conditions were used to estimate these properties.

11. Based on the hardness distribution of the welds in chapter IV, it is possible to see that there is a great difference in hardness between SZ and TMAZ/HAZ. Based on this general aspect, the model of joint interface was assumed to have three different regions; SZ, TMAZ/HAZ, and BM.

6.2.3 Geometry

For the thermal model, the half of the upper and lower sheets, the IL part, the stationary shoulder, the welding tool, and the anvil were modeled as shown in Figure 6.1. A symmetric condition was used to reduce the simulation time.

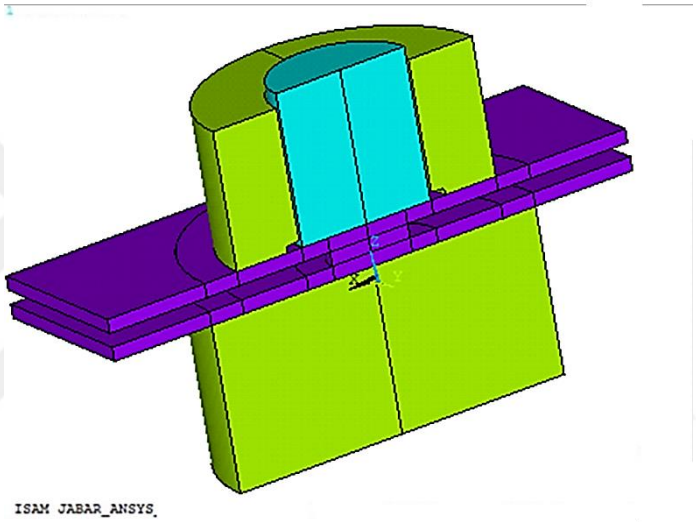

Figure 6.1 The geometry of the thermal model

The joint geometry of mechanical model was defined as shown in Figure 6.2. This figure shows the interface between the upper and lower sheets in lap configuration, as well as different joint regions. The SZ can be seen exactly where the tool penetrates. Around the periphery of SZ is located the TMAZ/HAZ, where a constant width of 1.5 mm was assumed according to the microstructure investigations in chapter IV, and beyond its external boundary, the BM (upper and lower sheets) that did not has experienced any microstructure change.

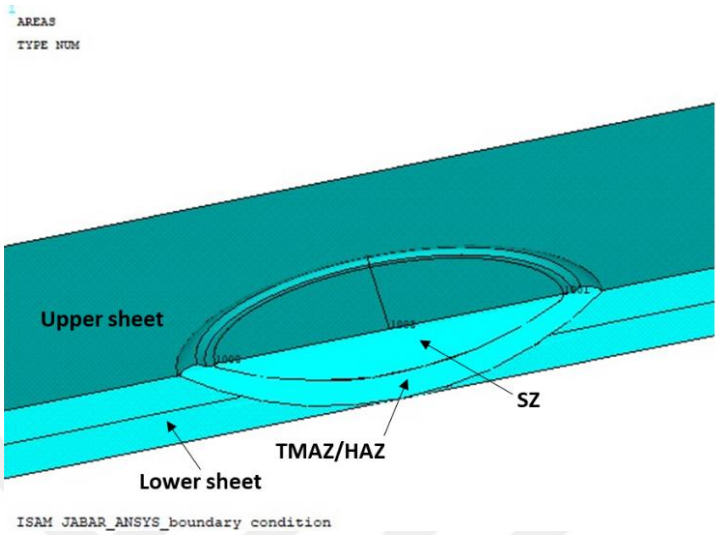

Figure 6.2 The joint geometry of the mechanical model

6.2.4 Elements Used

The metal sheets were meshed with the SOLID226 element, which has twenty nodes with up to five degrees of freedom at each node. The stationary shoulder and the rigid anvil were meshed with the SOLID98 tetrahedral coupled field solid element. This element has up to six degrees of freedom at each node [146]. The heat generation can be input as surface loads at the element faces, as shown by the circled numbers on the element geometry in Figure 6.3.

In order to include radiation heat transfer and convection heat loss, the SURF152 element was used with the extra node option [146,147]. It simulates the radiation heat loss to a space node and is applied to a 3-D thermal analysis. The space node serves to absorb all the radiated energy from the model surfaces [148]. The space node temperature was set as the ambient temperature.

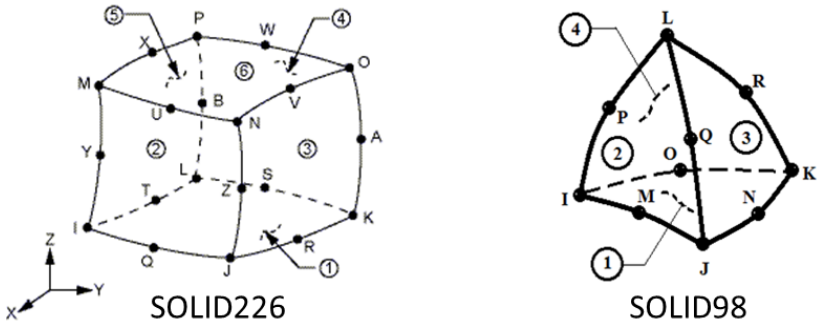

Figure 6.3 Three dimensional coupled-field solid elements [146]

6.2.5 Mesh Generation

For the thermal model, SOLID226 elements were used to mesh the sheets and IL part whereas for all the tools, stationary shoulders, and the anvil, SOLID98 elements were used in the meshing processing. The sheets and IL part were divided into 200 parts along the length, 10 parts along the width and 2 parts along the thickness direction. The mesh was composed of 34591 as a total number of elements, Figure 6.4(a).

For the mechanical model, the Figure 6.4(b) shows the general aspect of the resulting mesh of the weld regions. As the highest stresses are developed in the region of contact between the sheets, the mesh density should be greater in this zone. The number of elements was about 31815.

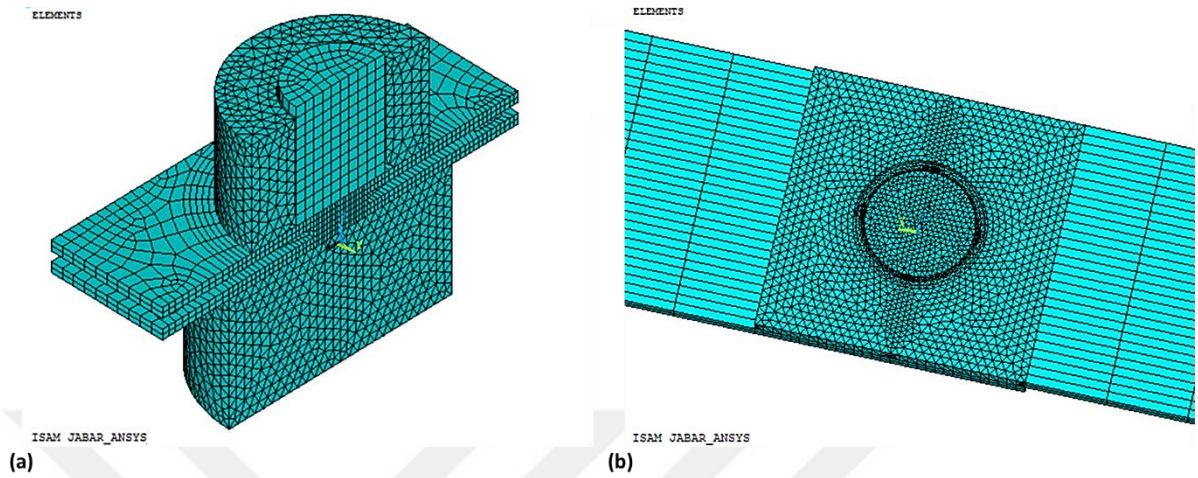

Figure 6.4 The mesh generated of IL-FSSW simulation, (a) the thermal model and (b) the mechanical model.

6.2.6 Material Properties

Regarding the thermal model, the properties of the materials used, such as specific heat, thermal conductivity, and density are temperature dependent. The modeling of the accurate temperature estimation in the welding processes is critical because the developing of stresses and strains of the welding regions are temperature dependent [149,150]. Therefore, the temperature dependent thermal properties of the Al 6061-T6 [145,151] and Al 2024-T3 [147,152] alloys were used in the model, as shown in Tables 6.1 and 6.2.

In order to define the temperature dependent properties, combinations of MPTEMP and MPDATA commands were used. The MPTEMP was used to define the temperature series and the MPDATA was used to define the corresponding material property values. The ambient temperature was assumed to be 41°C, which is equal to that measured in the experiments. The initial temperature of the workpiece is assumed to be equal to the ambient temperature [153].

Table 6.1 Temperature dependent material properties for the Al 2024-T3 alloy [147,152]

Temperature (°C)	Thermal conductivity (W/m °C)	Heat Capacity (J/Kg °C)	Density ($Kg/m^{3)}$	E (GPa)	Yield stress (MPa)	Coefficient of thermal expansion (10^{-6}/ °C)
20	164	881	2780	72.4	473	14.000
100	182	927	2780	66.5	416.5	23.018
200	194	1047	2780	63.5	293.5	24.509
300	202	1130	2780	60.4	239.8	25.119
400	210	1210	2780	56.1	150	25.594
500	220	1300	2780	50	100	26.637

Table 6.2 Temperature dependent material properties for the Al 6061-T6 alloy [145,151]

Temperature (°C)	Thermal conductivity (W/m °C)	Heat Capacity (J/Kg °C)	Density ($Kg/m^{3)}$	E (GPa)	Yield stress (MPa)	Coefficient of thermal expansion (10^{-6}/ °C)
37.8	162	945	2685	68.54	274.4	23.45
93.3	177	978	2685	66.19	264.6	24.61
148.9	184	1004	2667	63.09	248.2	25.67
204.4	192	1028	2657	59.16	218.6	26.60
260	201	1052	2657	53.99	159.7	27.56
315.6	207	1078	2630	47.48	66.2	28.53
371.1	217	1104	2630	40.34	34.5	29.57
426.7	223	1133	2602	31.72	17.9	30.71

Regarding to the mechanical model, the properties of the BM region were chosen also according Tables 6.1 and 6.2. The properties of the other regions (TMAZ/HAZ and SZ) were estimated depending on the hardness values of the welded samples as shown in Figure 6.5.

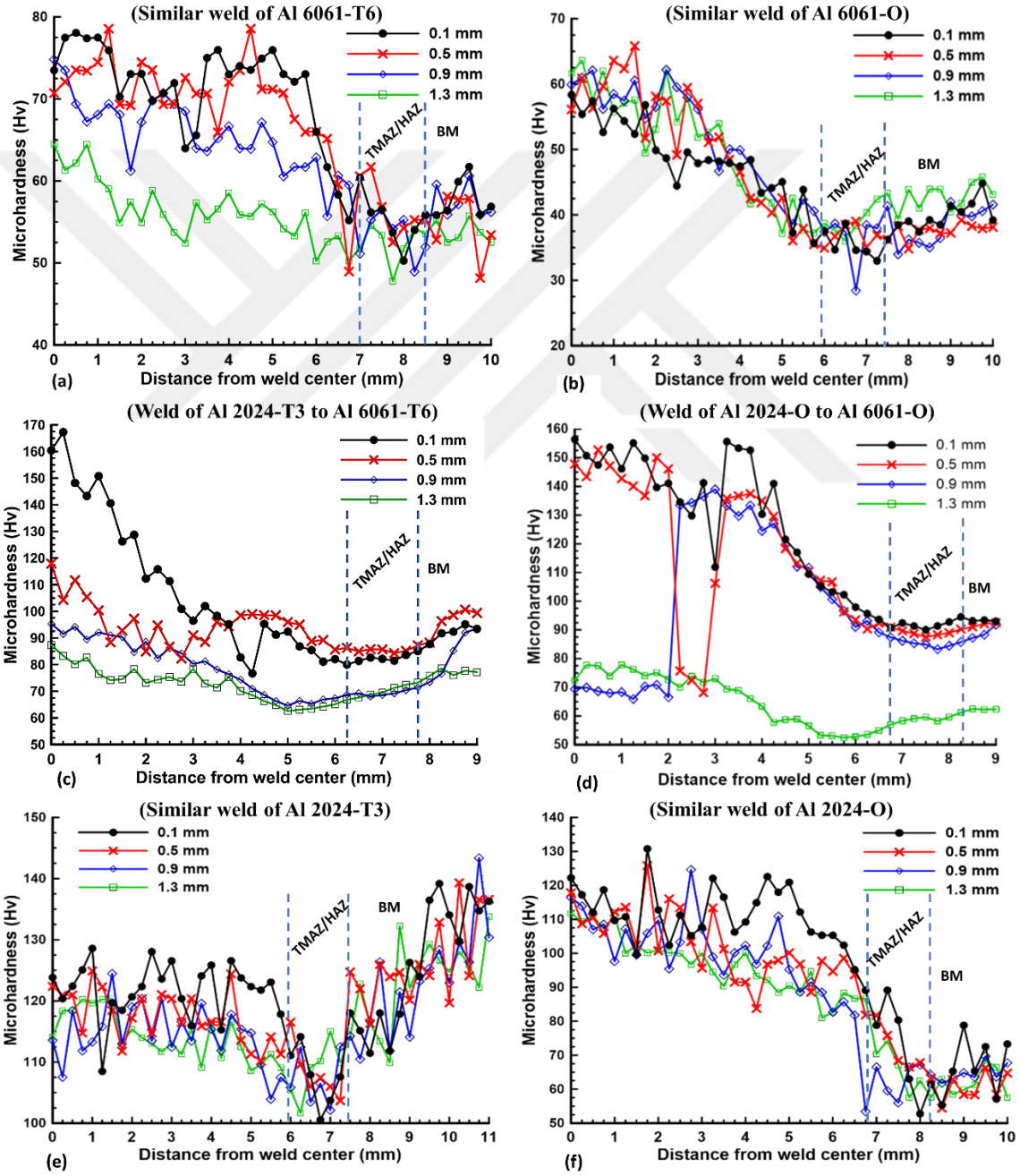

Figure 6.5 Typical hardness profiles of different welded samples

The blue dashed lines define the position of TMAZ/HAZ boundaries approximately. Analyzing the hardness curves, it is observed that there was a significant change in hardness between the TMAZ/HAZ and SZ regions, whereas a slightly hardness decreases in the boundary region between TMAZ/HAZ and BM in general. Based on this, three different tensile curves were assumed for each region, as shown in Figure 6.6. The middle black lines show the stress-strain curve corresponding to the base metal properties whereas both the blue and the red lines show the proposed tensile curves for SZ and HAZ/TMAZ welds' regions.

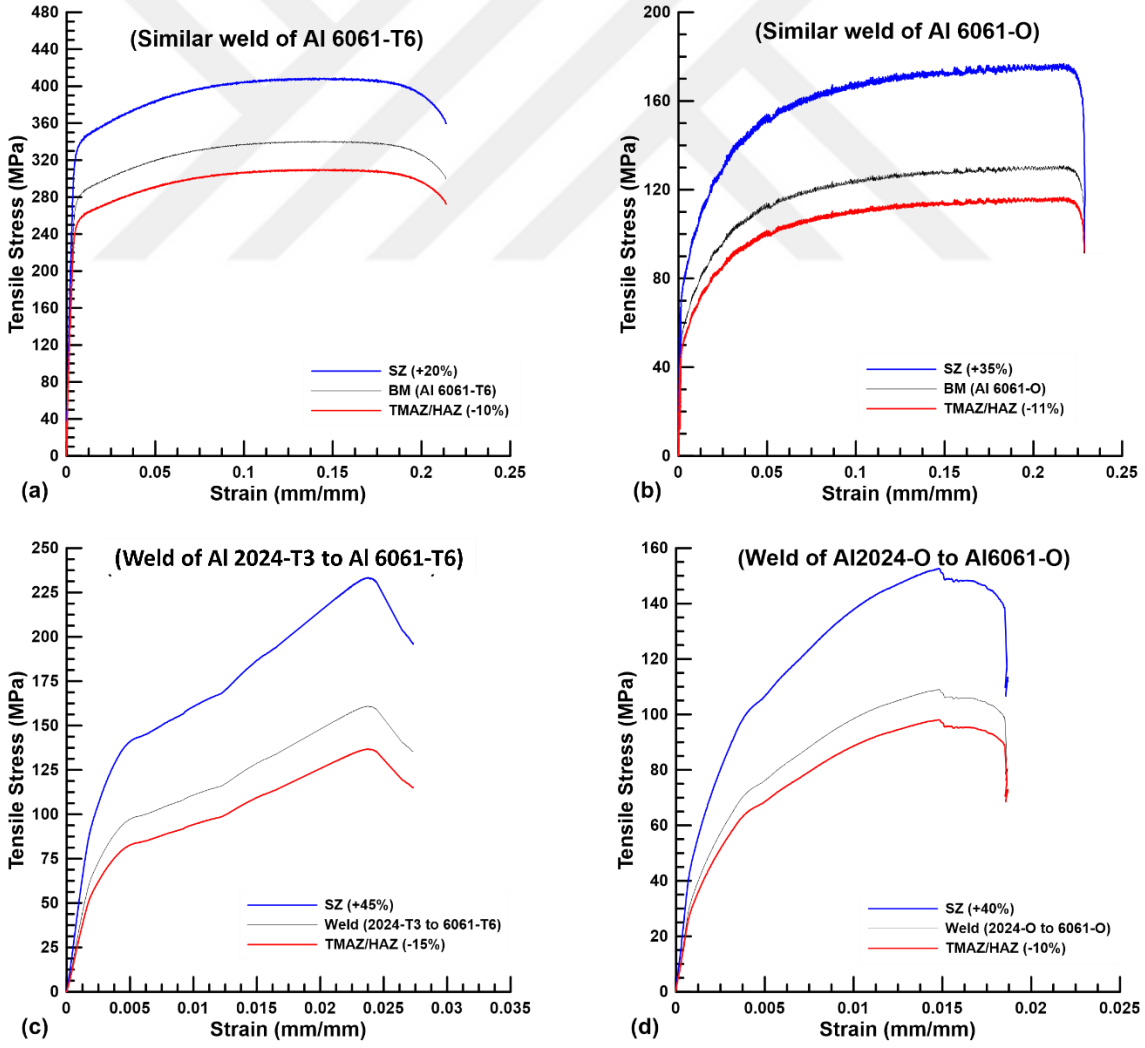

Figure 6.6 The stress-strain curves assumed for weld regions in the mechanical model for different samples

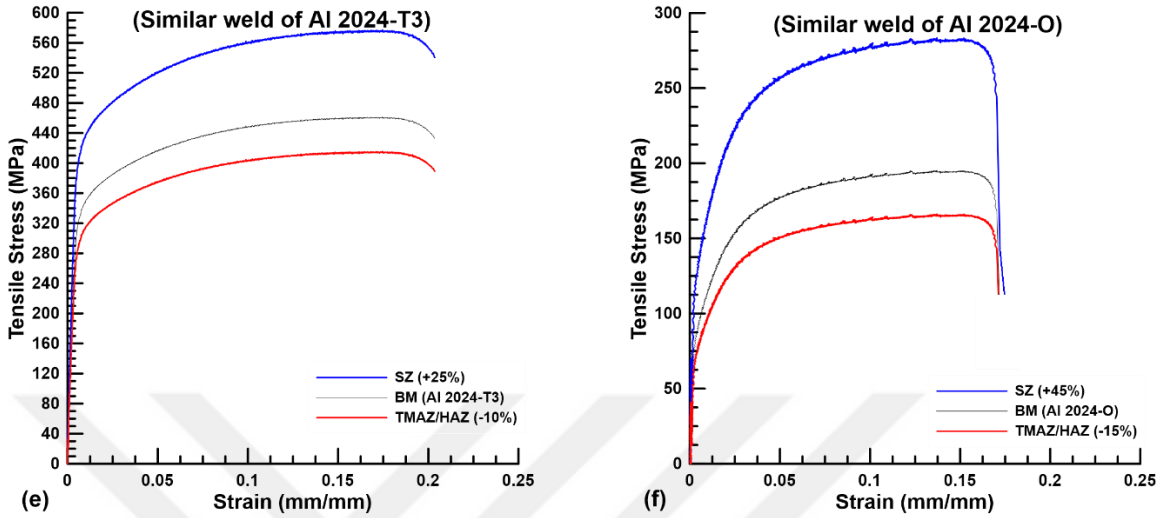

Figure 6.6 (Continuing)

6.2.7 Boundary Conditions

The boundary conditions of the IL-FSSW model were specified as surface loads through the ANSYS 18.2 codes. Assumptions were made for various boundary conditions based on the data collected from different published papers [149,150,153,154]. For the thermal model, convective and radiative heat losses to the ambient occur across all the free surfaces of the workpieces, and conduction losses occur from the workpieces' surfaces to the anvil and the stationary shoulder. According to the literature, it has been noted that no specific theory has been found to predict the heat loss through the bottom and top surfaces of the upper and the lower sheets. However, the heat loss (q_s) was calculated using the following equation [151,155];

$$q_s = h(T - T_0) + \xi\varepsilon(T^4 - T_0^4) \quad \text{.....(6.2)}$$

Here T is the absolute temperature of the workpiece, T_0 is the ambient temperature (41

°C), ε is the emissivity of the plate surfaces (0.5), and ξ is the Stefan-Boltzmann constant (5.67×10^{-12} W/cm^2 °C), and h is the heat convection coefficients on the top surface and the bottom surface of both the upper and the lower sheets, which is taken to be (30 W/m^2 °C) as a typical value for a natural convection between aluminum and air [145,149]. Figure 6.7 shows the schematic of the boundary conditions that were used.

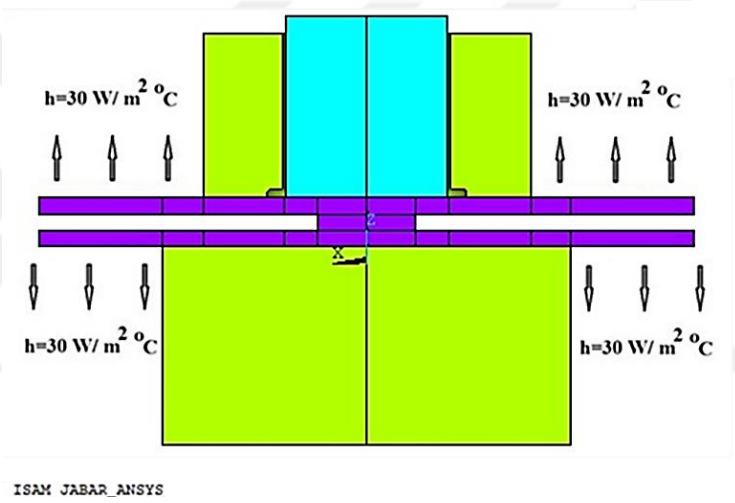

Figure 6.7 Schematic diagram represent the boundary conditions of the thermal model

In the mechanical model, to simulate the actual load condition experimented during the shear-tensile test, the extremity of the simulated sample was pinned at one side, which means that the displacements in the orthogonal directions x, y, and z were set to equal to zero. On the other hand, the opposite side was set to be free to displeased with the load direction, which is y-axis in this model. Also, the vertical movement of the external portion of both sheets was not allowed, to reproduce the effect of shear- tensile test. As shown in Figure 6.8

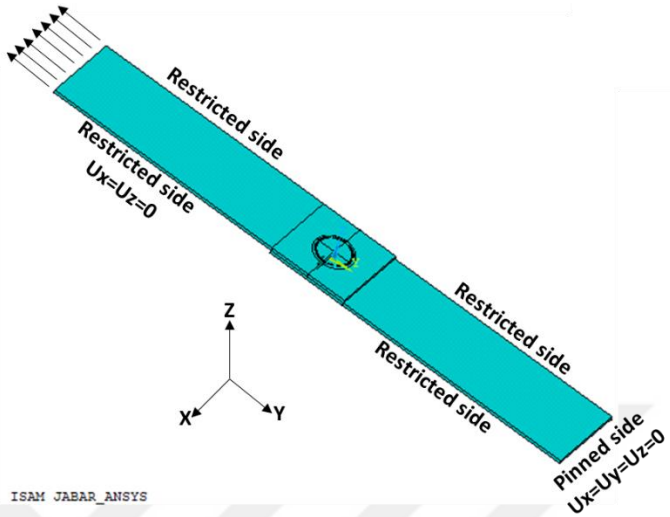

Figure 6.8 Lap-shear model, geometry and boundary conditions

6.3 Heat Generation in IL-FSSW

The heat generation and rising temperature of the workpieces' surfaces are generally associated with the friction that converts kinetic energy into thermal energy [145]. According to Blau [156], about 90-95% of energy due to friction is transformed to heat and about 5-10% of the remaining energy is used to deform the material and some of it is stored as defects in the contacting materials. In the IL-FSSW process, the mechanical interaction, as a result of the velocity difference between the rotational tool and the fixed workpiece, produces heat by frictional work[145], Figure 6.9(a). According to Figure 6.9(b), the contact area changing during the tool advance with the increasing of the plunging depth may be derived and based on the following equation;

$$dA = 2\pi \, rdr \quad \text{.....(6.3)}$$

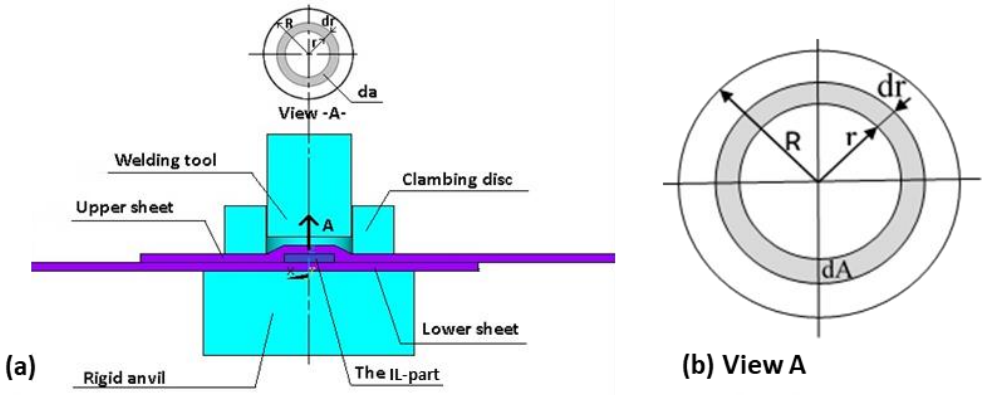

Figure 6.9 (a) Schematic representation of welding set-up, (b) contact area between the tool and upper sheet

The experiments were conducted to measure the contact area during the tool advance by measuring the imprint diameters of the tool's contact for the nine steps of the plunging depth as shown in Table 6.3.

Table 6.3 The contact diameter with respect to the plunging depth for both cases of the Al 6061-T6 and Al 6061-T6 to Al 2024-T3 weld processing

Plunging depth (mm)	Contact diameter (mm)	
	Similar Al 6061-T6 sheets	Dissimilar Al 6061-T6 to Al 2024-T3 sheets
0.1	4	6
0.2	5	7.5
0.3	6.5	8.7
0.4	9	10
0.5	10	10
0.6	10	10
0.7	10	10
0.8	10	10
0.9	10	10

The frictional torque required to rotate a circular shaft relative to a plane surface under the action of an axial load is given by:

$$T = \frac{2}{3}\pi\mu Pr^3 \quad (6.4)$$

where: T is the interfacial torque,

μ is the instantaneous frictional coefficient,

P is the interfacial pressure,

$$\mu = \frac{3T}{2\pi Pr^3} \quad (6.5)$$

$$P = \frac{\text{Axial load}}{\text{Contact area}} \quad (6.6)$$

Measuring the axial load helps to calculate P by dividing the axial load over contact area, Equation 6.6. The contact area between the tool and the surface of the upper sheet was measured in Table 6.3. According to Equation 6.5, the μ is calculated at each step of the tool plunging depth via P and T values, in which these values were measured experimentally by using a rig specially designed for this reason. The values of P and T are tabulated in tables 6.4 and 6.5. The total frictional heat for the rotating tool at an angular speed of (1-δ)ω is:

$$Q = \frac{2}{3}\pi(1-\delta)\omega\mu Pr^3 \quad (6.7)$$

where δ is the slip factor that compensates for the tool/material relative velocity [157]. The typical value for the slip factor found in the literature ranges between (0.6 – 0.85), and it was selected to be 0.7 in this study [157].

The ω value can be calculating according to the equation

$$\omega = \frac{2\pi N}{60} \quad \text{.....(6.8)}$$

For the cases of similar welds of Al 6061-T6, $\omega = 125.66\, rad/sec$, whereas for the cases of dissimilar welds of Al 2024-T3 to Al 6061-T6, $\omega = 157.08\, rad/sec$.

According to Equation (6.7), the Q values for each step of the plunging depth were calculated and tabulated in Tables 6.4 and 6.5, and used as input loads in the IL-FSSW modeling in order to calculate the temperature distribution on the welded sheets.

Table 6.4 P, μ, & Q for each step of plunging through welding of the Al 6061-T6 sheets

Plunging depth (mm)	Axial load (N)	Tool torque (N.m)	P (MPa)	μ	Q (Watt)
0.1	338.1	0.5	26.89	1.109	18.849
0.2	812.8	1.2	41.38	0.886	45.2376
0.3	1424.9	2.1	42.92	0.680	79.1658
0.4	2141.8	3.2	33.65	0.498	120.6336
0.5	2318	5.8	29.50	0.751	218.6484
0.6	3139.8	7.2	39.96	0.688	271.4256
0.7	4103.3	8.9	52.22	0.651	335.5122
0.8	4969.9	8.8	63.25	0.531	331.7424
0.9	5409	8.3	68.84	0.460	312.8934

Table 6.5 P, μ, & Q for each step of plunging through welding of Al 2024-T3 to Al 6061-T6

Plunging depth (mm)	Axial load (N)	Tool torque (N.m)	P (MPa)	μ	Q (Watt)
0.1	160.9	0.2	5.69	0.622	9.4248
0.2	718.4	0.46	16.25	0.256	21.67704
0.3	2094.5	1.77	35.22	0.291	83.40948
0.4	2314	3.75	29.45	0.486	176.715
0.5	2900.8	4.81	36.92	0.497	226.6664
0.6	3743.7	6.04	47.65	0.484	284.629
0.7	5030.2	6.74	64.02	0.402	317.6158
0.8	6810.8	6.85	86.68	0.302	322.7994
0.9	6839.7	6.93	87.05	0.304	326.5693

6.4 Temperature Distributions

In the model, the plunging feed rate was chosen (20 mm/min) for the weld processing of the similar Al 6061-T6 sheets, and the corresponding process time was approximately 3.7 s, whereas in the case of the dissimilar welding of the Al 2024-T3 to Al 6061-T6 sheets, the plunging feed rate was (25 mm/min) and the corresponding process time was 3.16 s. There was 1 s initially used as a time for moving the stationary shoulder for each case. Figures 6.10 and 6.11 show the temperature contours of the IL-FSSW weld processing model. The highest temperature was observed in the center, since the rotating of the tool contributes to the highest heat flux in this region. The higher heat dissipation is through the contact surfaces between the sheets and, the anvil and the stationary shoulder were compared with the top surface of the upper sheet, where the heat generation source exists.

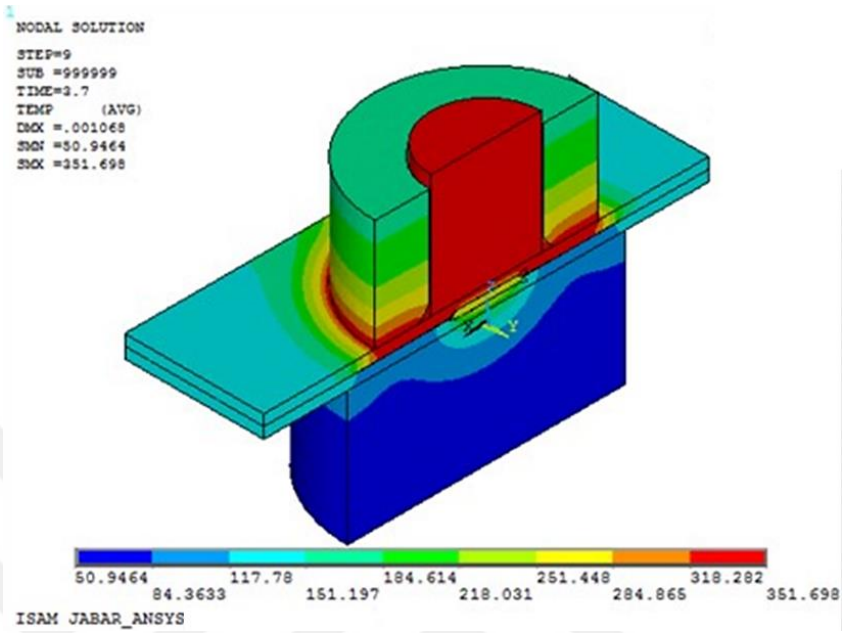

Figure 6.10 Temperature distribution during the weld processing of the similar Al 6061-T6 sheets, (feed=20mm/min and ω=1200 rpm)

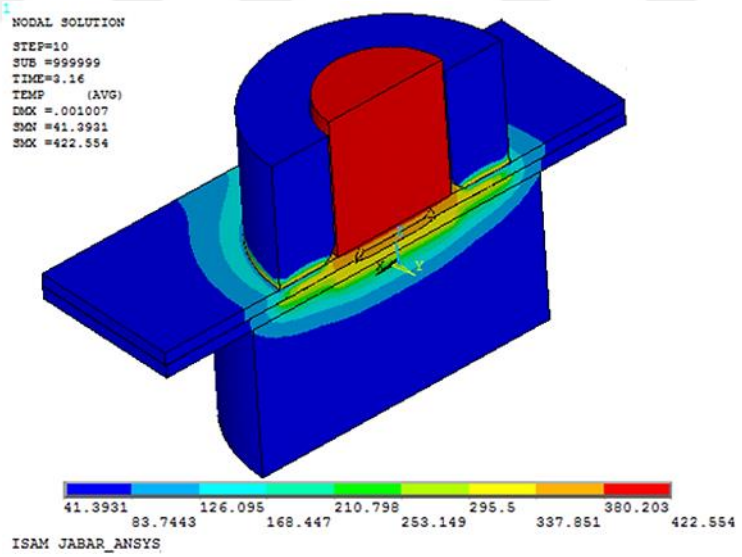

Figure 6.11 Temperature distribution during the weld processing of the dissimilar Al 2024-T3 to Al 6061-T6 sheets, (feed=25mm/min, ω=1500 rpm)

Figure 6.12 shows the top view of the upper sheet during the weld processing, the temperature increases with the increasing of the plunging depth, i.e., the time of the process. The maximum temperature occurred at the friction region. This is attributed to the fact that

the highest heat is generated in this region. The highest heat radiation and convection dissipations occur in the regions just beyond the tool edge.

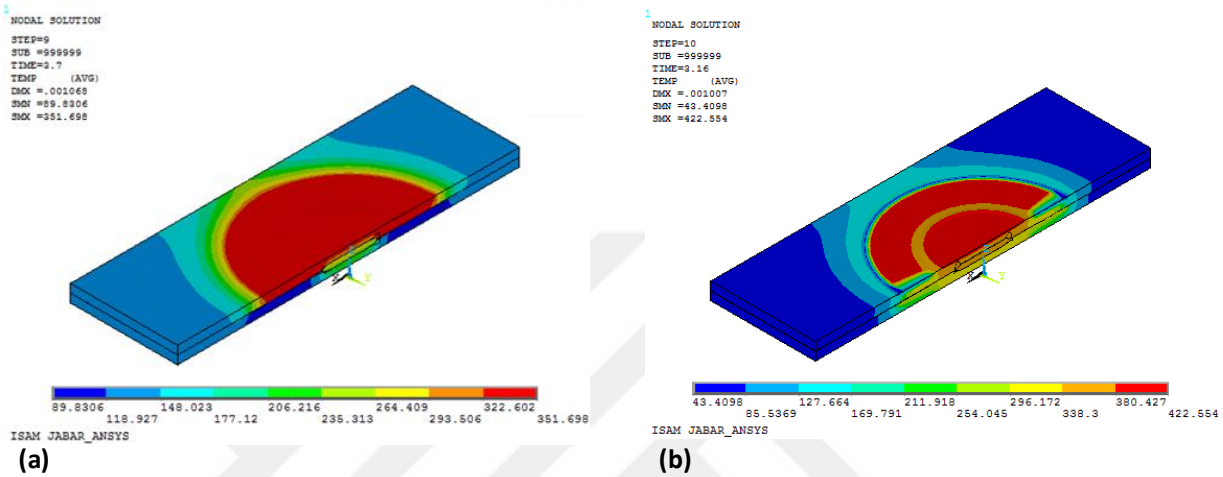

Figure 6.12 Top view of the welded sheets of the IL-FSSW weld processing model (a) Al 6061-T6 sheets, (b) Al 2024-T3 to Al 6061-T6 sheets

Figures 6.13 and 6.14 show the temperature distribution measured experimentally and theoretically, by the ANSYS model for the similar Al 6061-T6 and Al 2024- T3 to Al 6061-T6 welded sheets. It is clear from these figures that there is a reasonable difference in the temperature distributions. The reason is, at the ANSYS modeling, there are many assumptions which affect the results. It can be noticed that the temperatures measured experimentally are always higher than those in the ANSYS model. The reason for that is that heat load was applied as a step load in the model, while the actual load was applied as a continuous ramp load. The other reason is that at the end of the process, the contact area was not only between the surface of the tool and the top surface of the upper sheet, but also there were some metal particles which flowed up and came into contact with the periphery of the tool, which produces an additional source of heat not considered in the ANSYS simulation.

Figure 6.13 showed that the maximum experimental temperature was 358 ℃ at the center, while it was 330 ℃ in the model. The error was about 7.8 %. The curve of 10 mm from the center of the spot showed close values between the experimental and model temperature distribution, whereas the experimental and model values were 225 ℃ and 230 ℃, respectively, and the error was 2.2 %. At a 15 mm distance from the weld center, the temperatures' values were 90 ℃ and 77 ℃ in the experimental and model curves, respectively. The error percentage was 14.4 %. Figure 6.14 shows the temperature distribution of the Al 2024-T3 to Al 6061-T6 welded sheets. At the center of the spot, the values for both the experimental and model were very close, the maximum temperature was 367 ℃ from the experimental test, while it was 358 ℃ from the ANSYS model, and the error was 2.4 %. At 10 mm from the spot center, the temperatures were 187 ℃ and 170 ℃ in the experimental and ANSYS model curves, respectively. The error was 9 %. In the 15 mm curve, the temperatures were 155 ℃ and 134 ℃ in the experimental and model values, respectively. The error percentage was 13 %.

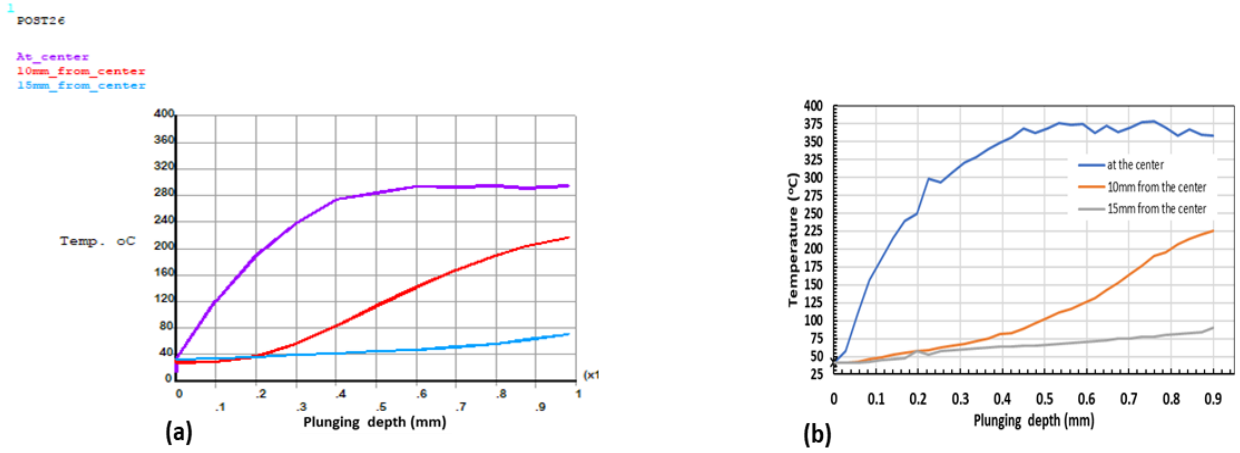

Figure 6.13 Temperature distribution through the weld processing of weld similar Al 6061-T6 sheets (a) ANSYS model results, (b) experimental results

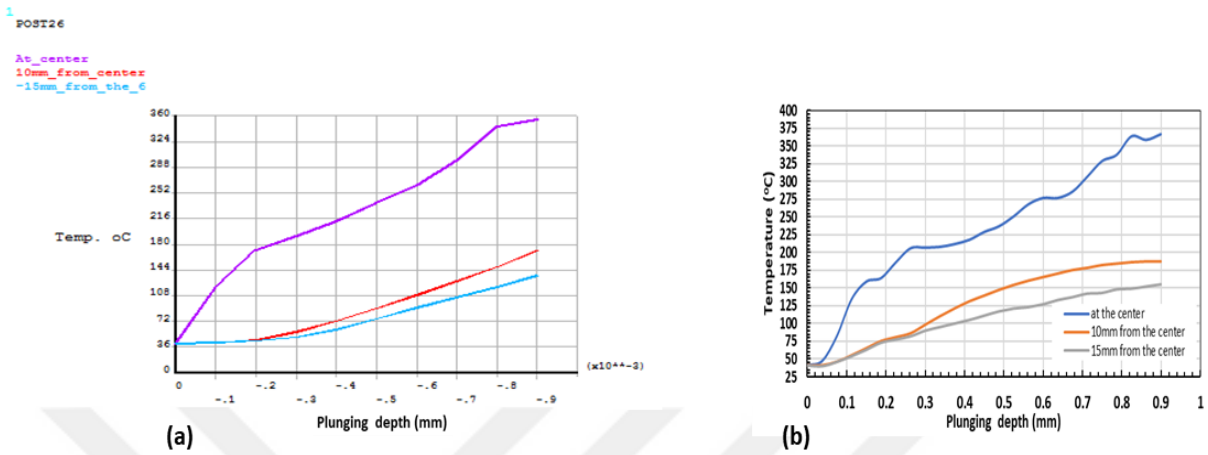

Figure 6.14 Temperature distribution through the weld processing of dissimilar Al 2024-T3 to Al 6061-T6 sheets (a) ANSYS model results, (b) experimental results

6.5 Results of The Mechanical Model

The view from the progression of the tensile simulation of the joints are demonstrated in Figure 6.15(a). The increase in the displacement levels occurs predominantly at the edge of lap configurations of the welded sheets around the weld nugget. The behavior of the welded sample in the simulation is similar with that in the experimental test, in which the welded sample undergoes a rotation of the nugget zone as seen in Figure 6.15(b),

During simulation progress, as the load produced by the relative displacement between the sheets is increased, the region of stress concentration is formed around the spot of the weld region as seen of the stress state ratio in Figure 6.16.

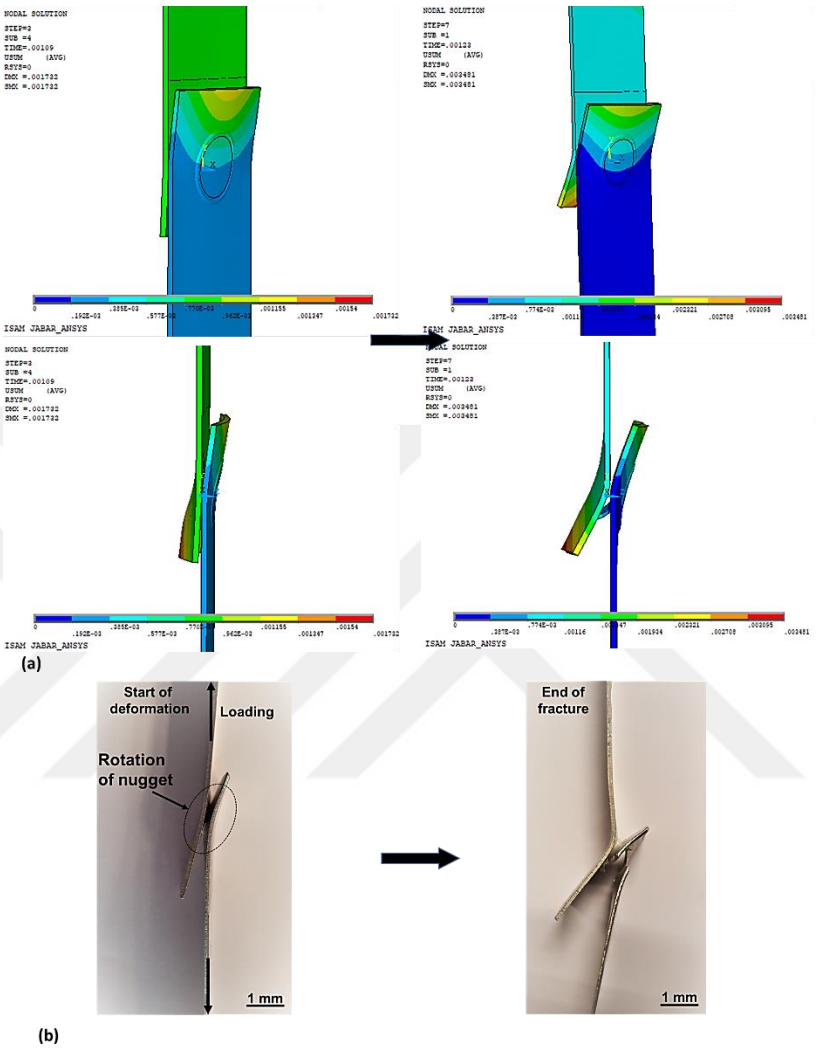

Figure 6.15 Failure development of Al 2024-O to Al 6061-O dissimilar weld under tensile loading: (a) simulation progress, (b) experimental progress

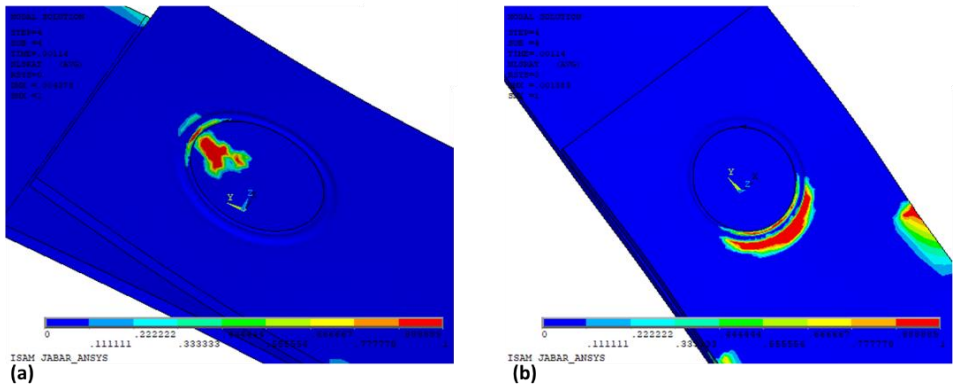

Figure 6.16 Stress state ratio of the weld sample: (a) Al 6061-T6 sheets, (b) Al 2024-T3 to Al 6061-T6 sheets

A further load increasing tend to increase the internal stresses which led to failure stage as seen in Figure 6.17. The failure mode will depend on how the fracture develops.

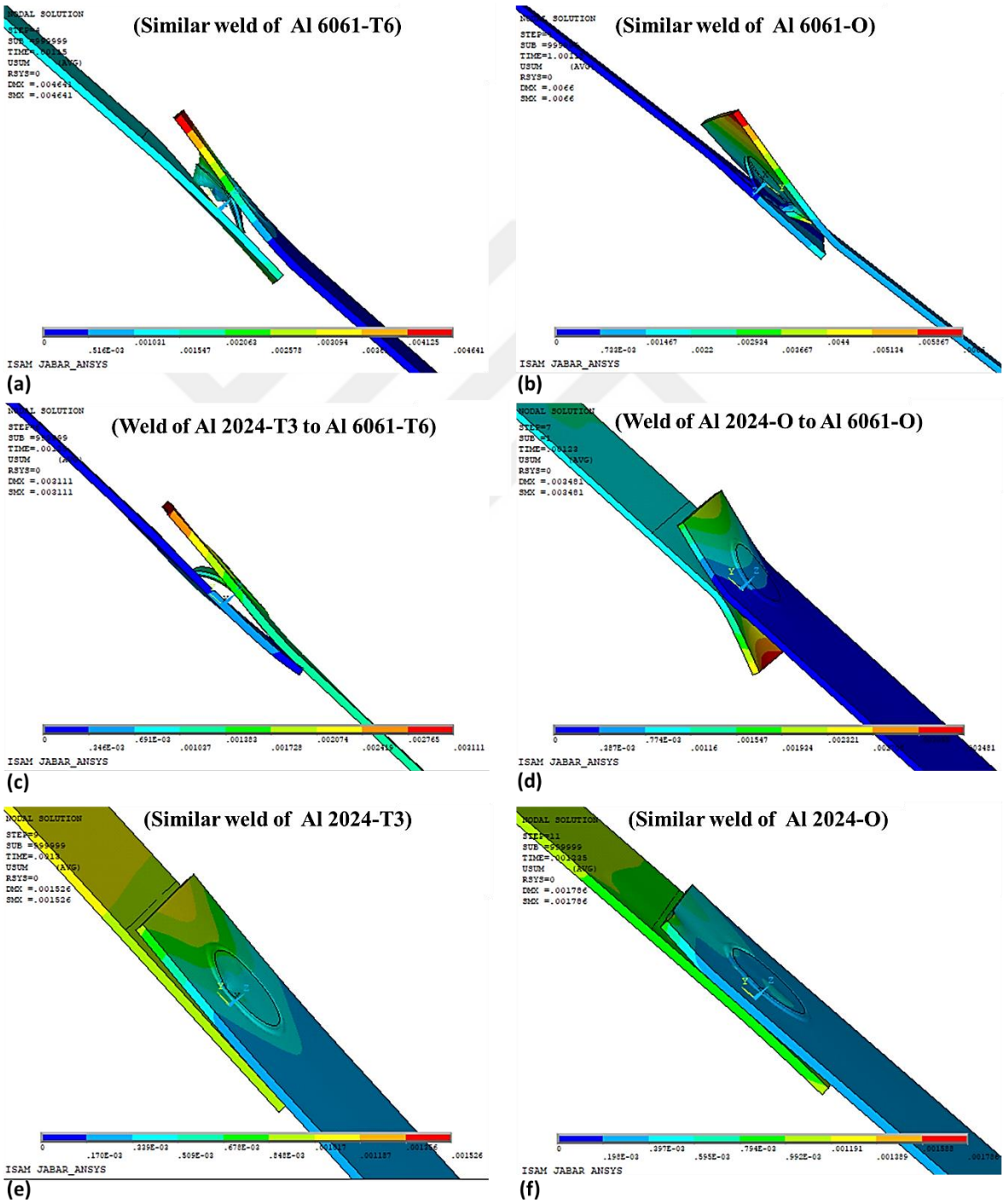

Figure 6.17 Failure behavior during the simulation of shear-tensile test of different welds

From Figure 6.17 the regions of higher stresses within the weld nugget extends indicating a possible plug-off and shear fracture types. This behavior is acceptable since the model exhibits similar failure behaviors with that in the experiment tests.

A comparison between the experiment results of shear-tensile tests performed for samples welded using the optimum parameters and the numerical model is shown in Figure 6.18. Although the maximum lap-shear force obtained from the simulation is not very similar to the value obtained during actual tests, still the error percentages between the model and experiment results are observed stable within limited range as shown in Table 6.6. This give good indication in which the results obtained from the model are coherent with the experimental values and allow to estimate approximate values of strength and failure mode.

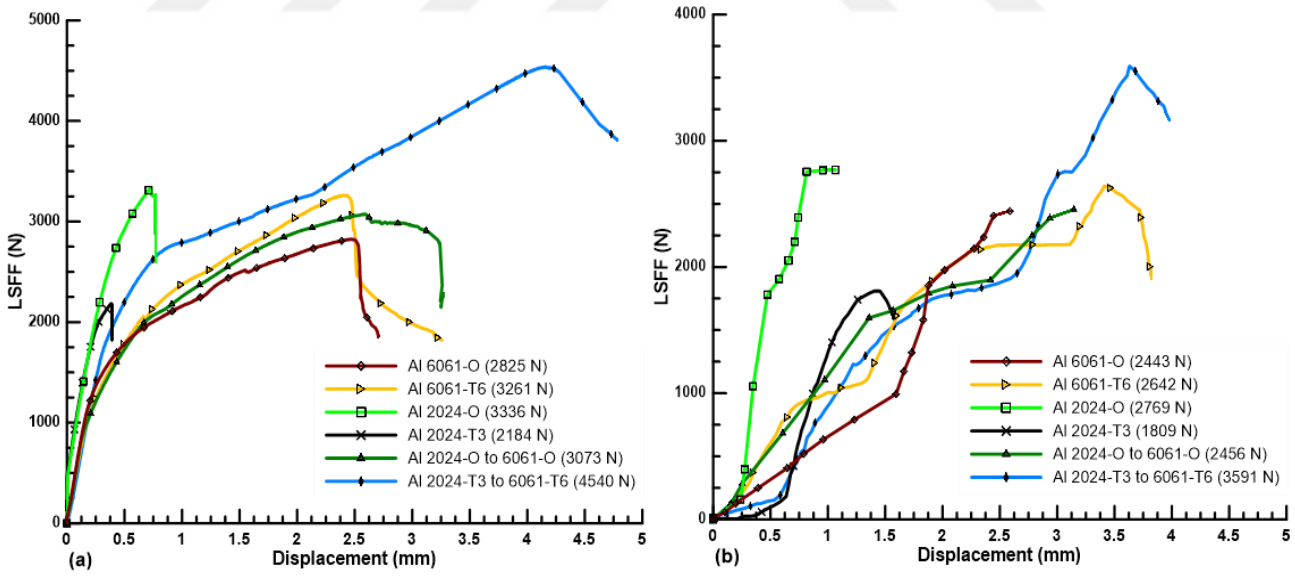

Figure 6.18 LSFF-displacement curves of different welds: (a) experimental results, (b) ANSYS model results

Table 6.6 The error values between the experimental and model results

Welded samples	LSFF (N)		Error %
	Experiment	Model	
Similar of Al 6061-T6	3261	2642	19
Similar of Al 6061-O	2825	2443	14.5
Al 2024-T3 to Al 6061-T6	4540	3591	21
Al 2024-O to Al 6061-O	3073	2456	20
Similar of Al 2024-T3	2184	1809	17.2
Similar of Al 2024-O	3336	2769	17

6.6 The Summary

The objective of this chapter was to study the variation of the transient temperature in the IL-FSSW of similar and dissimilar aluminum sheets. A numerical investigation was performed to model the temperature distribution during the weld processing. The 3D FE model was built using ANSYS codes to simulate this model. The torque and axial load of the tool were measured experimentally to determine the coefficient of friction, which was used with other parameters to find the applied heat flux in the used model. The temperature distribution values of the model were compared with the experiment values measured using three thermocouples to validate the results. The results show good agreement between the numerical and experimental values with a range of 2.2 – 14.4 error percentage.

Regarding the mechanical model corresponding to shear-tensile test samples were developed. The simulation showed limited levels of error arranged between 14.5% to 21% when compared with experiments result.

CHAPTER VII

THE CHARACTERIZATIONS OF Pure Cu/Al 6061 WELDS FABRICATED BY THE IL-FSSW PROCESS

7.1 Microstructure and Hardness Characterizations

The Al 6061-O alloy and pure copper sheets of a 1 mm thickness were welded by the IL-FSSW process and conventional FSSW process as a reference for the comparison in the shear-tensile test investigation. For the IL-FSSW, a 10 mm diameter tool of flat tip without pin was used, whereas for the conventional FSSW, the tool was combined of shoulder and 4 mm pin diameter, which about 1/3 of the tool shoulder diameter (10 mm) with a 1.5 mm pin length as decided, Figure 7.1.

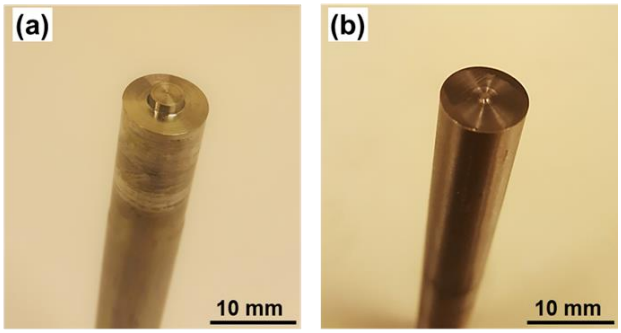

Figure 7.1 Welding tool: (a) conventional FSSW, (b) IL-FSSW.

Figure 7.2 shows the macroscopic views of the welds' top sides made by the IL-FSSW and the conventional FSSW processes. The sound joints with no keyhole was fabricated by the IL-FSSW process (Figure 7.2(a)).

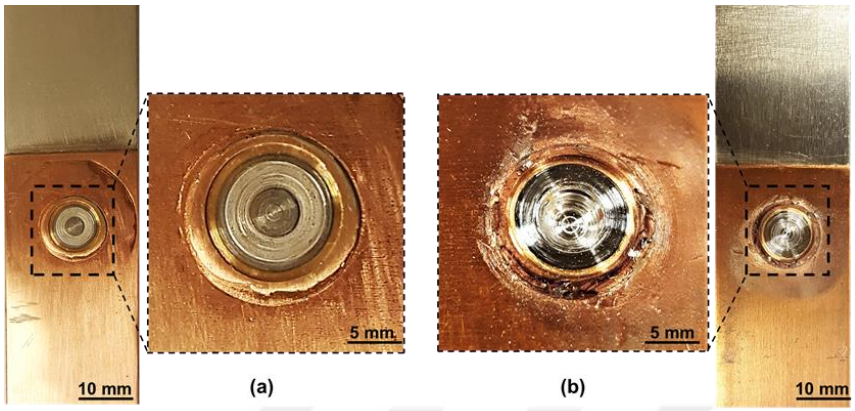

Figure 7.2 Macroscopic views of the spot welds: (a) IL-FSSW, (b) Conventional FSSW

Figure 7.3 shows the micrographic views of the joint fabricated employing the IL-FSSW and conventional FSSW. The formation of the intermetallic compounds was in between the sheets, at the tool periphery region, and can be observed in Figure 7.3(a) and (b) shows that a swirl layered structure is formed due to the mixing of the materials. Figure 7.3(a) shows the interlocking regions between the upper, lower sheets, and the intermetallic compounds. Also, the appearance of breakthrough to the top of the IL materials appeared due to the tool movement action being downwards with the increasing of the friction temperature. All of this provides a chance for the formation of intermetallic compounds.

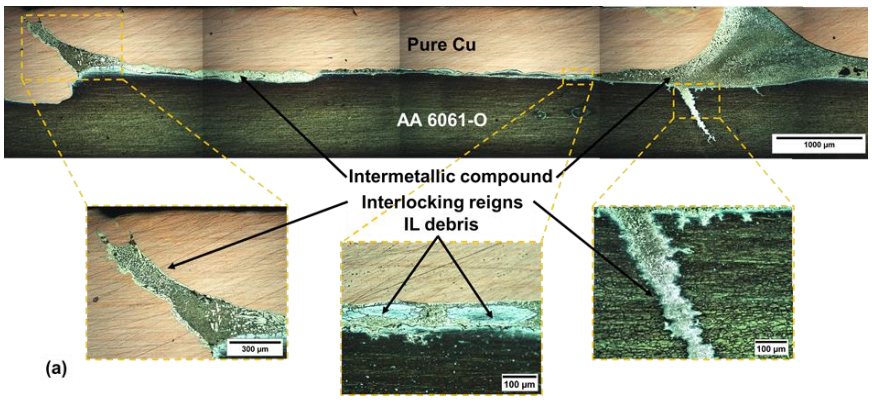

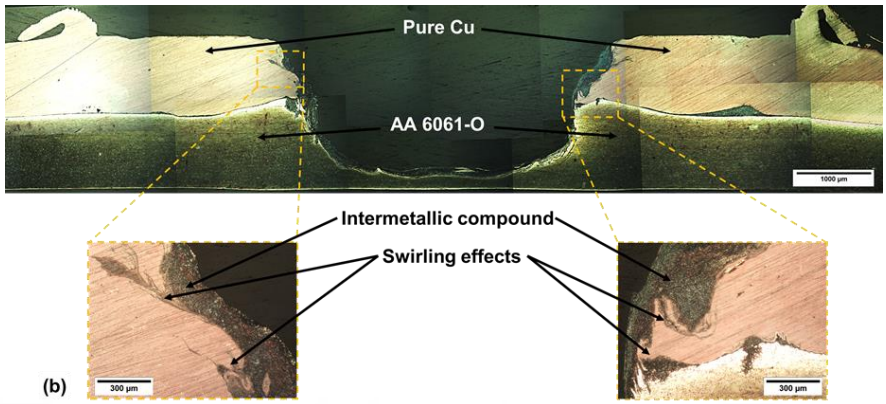

Figure 7.3 Microscopic images of welds cross section (a) IL-FSSW, (b) conventional FSSW.

The microhardness measurements using a Vickers microhardness tester were performed at a 100 gf for 15 s of a through-thickness IL-FSSW weld, along four parallel lines. The distance between one indent point to another was 0.25 mm along each line. Figure 7.4 shows the microhardness indents at different microstructural regions. The hardness of the heat unaffected regions of the base metals on the weld cross section were 58–75 Hv for the Al side and 75–95 Hv for the Cu side, respectively. The minimum value was approximately 52 Hv, which was located in the heat affected zone (HAZ) of the Al side.

Obviously, there are significant variations in the hardness numbers and indents sizes (Figure 7.4, enlarged of section A, marked by numbers 1–4) at different microstructural regions of the weld cross section. There was a fluctuating of the hardness (59–575 Hv) in the weld nugget that was related to the different microstructures of the formed intermetallic compounds and the separated patterns of the IL material. This is because the hardness as well as the strength of the intermetallic compounds were definitely higher than the base metals used.

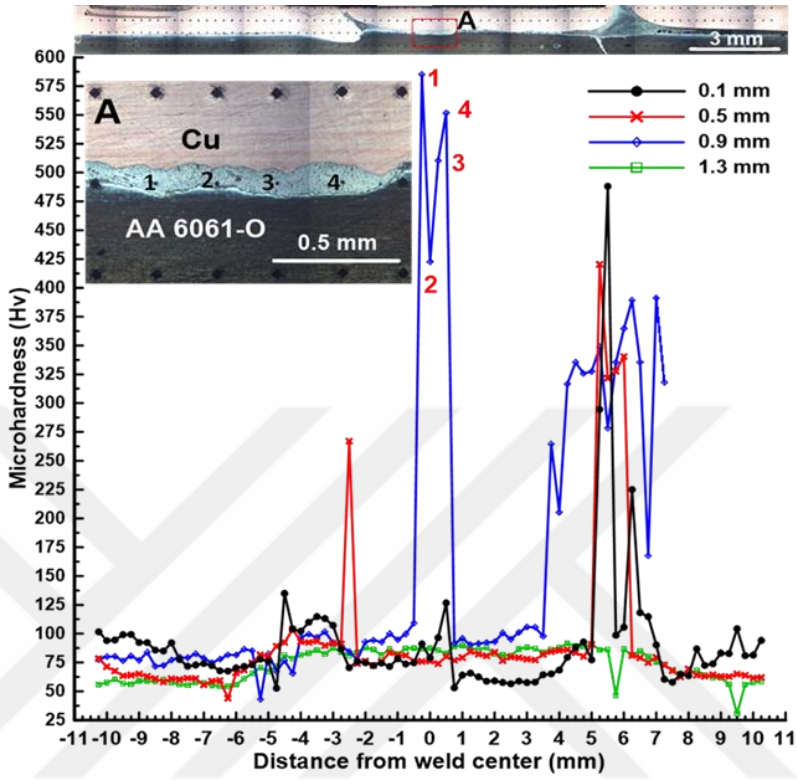

Figure 7.4 The Hv hardness profile of the IL-FSSW welded joint.

The hardness of the area covered by the intermetallic compounds at the IL region of the weld cross section was measured at about 200–575 Hv as shown in Figure 7.4 (the 0.9 mm line). Microhardness variations are common throughout the weld as a result of the diversity in the microstructures of the weld nugget and base metals such as grain size, density, precipitates, and intermetallic compounds.

7.2 Mechanical Characterizations

The lap shear failure forces (LSFF) were recorded for both the IL-FSSW and the conventional FSSW welds. It can be observed from Figure 7.5 that there is a slightly increase in the LSFF from 2.78 kN of conventional FSSW to 2.92 kN of the IL-FSSW, where the clear

variation demonstrates in the displacement distance between both welds. The difference in the displacement distance can be related to the keyhole indentation effect, i.e. the area covered by the intermetallic compound that formed at the joint interface of IL-FSSW weld is obviously much more than that in the conventional FSSW weld. The intermetallic compounds have a significant role in providing resistance to the crack propagation under the tensile load due to the interlocking effect with the Al and Cu sides [158]. From Figure 7.5, increasing displacement can be seen, the maximum displacement was increased from 0.82 mm of the conventional FSSW welds to 1.6 mm of the IL-FSSW welds.

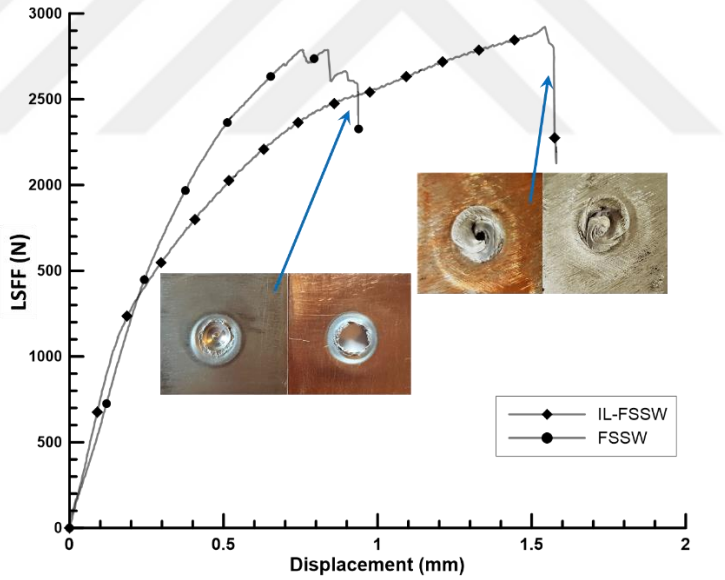

Figure 7.5 LSFF-displacement curves of the IL-FSSW and conventional FSSW spot welds

In both cases, the failure and separation of the sheets were observed from the weld spot peripheral. Additionally, for the joints prepared with the FSSW as well as the IL-FSSW process, the stirred metal particles below the welding tool intermixed. During the shear-tensile test, the weld nugget failure was observed mostly from the Cu side leaving part of Cu

metal attached on the Al side. The movement of the rotating tool downward in the plunging stage of weld processing caused an increase in the frictional heat on the IL material rapidly between the sheets to form an intermetallic compound and create a hardened region in the weld nugget.

7.3 Analysis EDS and XRD Results

The EDS analysis of the intermetallic compound region, the Al and Cu base metal sides, was performed to verify the compositions of these regions as shown in Figures 7.6(a)–(c), respectively. From Figure 7.6(b), it can be seen that the major elements presented in the intermetallic compound were Al and Cu, which supports the fact of the intermixing of the IL part with the upper and lower sheets, and leads to the forming of the Al/Cu intermetallic compound. The presence of the distinguished proportion of the O_2 in the EDS curves ensures the oxidation of the base metals. Figures 7.6(d) and (e) show the compositions of the elements present in spots 4 and 5 in the IL debris. The major element present in these spots was Al, which supports the fact that the IL part was crashed under the movement action of the rotational tool downward. The presence of the O_2 in spots 4 and 5 indicates the formation of oxides in the IL debris region as a diffusion beginning before the forming of the intermetallic compounds in this zone.

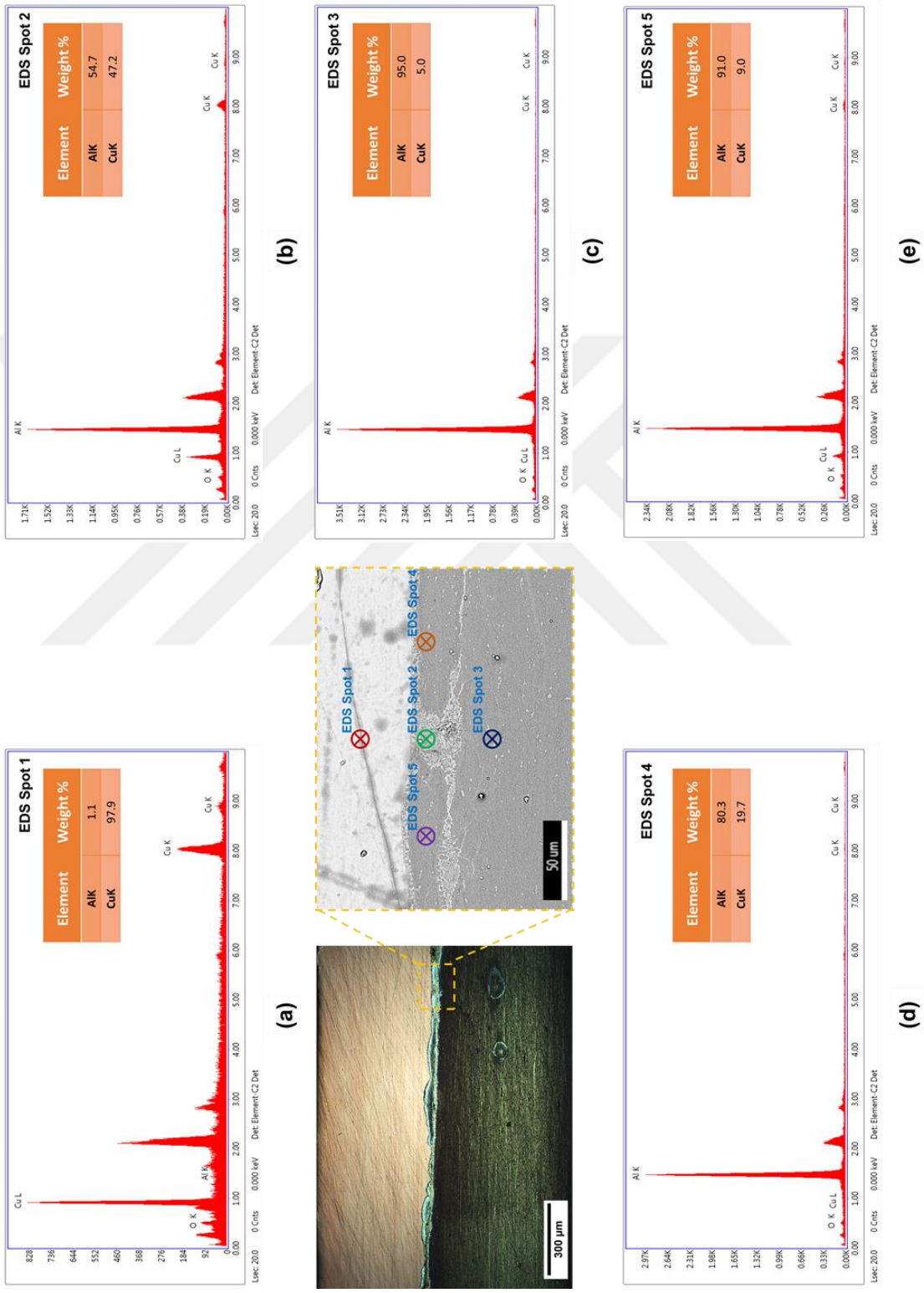

Figure 7.6 EDS analysis results of the IL-FSSW welded joint

The X-ray diffraction patterns on the centerline of the weld cross section are shown in Figure 7.7. The results illustrate that the joint consists mainly of intermetallic compounds such as Al_2Cu and Al_4Cu_9 together with some amounts of Al and Cu (the saturated solid solution of Al in Cu). The variations of the Al, Cu, and intermetallic compound peaks corroborate the complex mixing of the Al and Cu grains in the weld zone. Conferring to the XRD results, the high frictional temperatures correlated with the stirring action caused by the mixing of Al and Cu heterogeneously, which lead to the form intermetallic compounds like Al_2Cu and Al_4Cu_9. This means that a chemical reaction occurred between the Al and Cu during the weld processing. Hard, brittle intermetallic compounds between the dissimilar joint of the Cu to Al are formed through the liquid state reaction, which results from the excessive frictional heat generated and phase transformation [159–161].

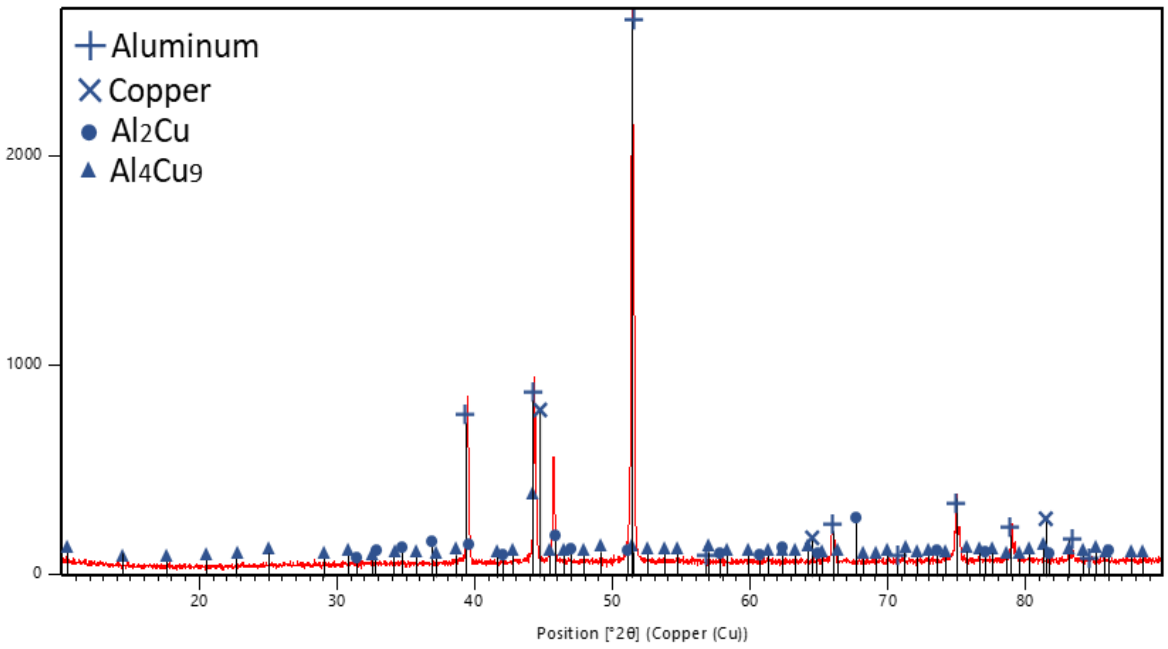

Figure 7.7 X-ray diffraction patterns of the IL-FSSW welds at the weld centerline

7.4 Analysis of Intermetallic Compounds Formation

Figure 7.8 represents the optical microscopic images of the through-thickness section of the welded joint. In general, fluid-like complex flow patterns arise due to the irregular solid system formed by the flow of one recrystallized metallic regime through another [162–165]. The darker regions indicate to Al rich side, whereas the visible regions indicate to Cu rich side. Figure 7.8(a) shows the bonded region between both the Cu-Al sheets and the IL part, which was observed with a notable demarcation line. Almost, all of the IL material (Al 6061-O) was found stirred with copper at the bottom surface of the upper sheet to form the Al_2Cu and Al_4Cu_9 intermetallic compounds (the saturated solid solution of aluminum in a copper) as the XRD test revealed.

The intermetallic compounds were formed as a result of the diffused IL material with the upper and lower sheets. In order to know how the intermetallic compounds are formed, it is necessary to analyze the Al–Cu phase diagram, Figure 7.9 [166]. Still, this diagram is ineligible in the explanation of the thermal changes that occur rapidly during the welding process. Based on the fact of the existence of the Al_2Cu and Al_4Cu_9 intermetallic compounds, the peak temperature inside the weld nugget is expected to be higher than the eutectic temperature (548 °C) of the Al–Cu binary system. The peak temperature was measured experimentally by the embedded thermocouple at the bottom of the lower sheet as 361 °C. This is assuming that a very good materials mixing is obtained by the friction/stirring action of the welding tool and the time was sufficient to reach the equilibrium condition of the liquid phase reactions. The phase diagram indicates two ways to form Al_2Cu, peritectic reaction ($L + \eta 1 \rightarrow \theta$ (Al_2Cu) at 590 °C) and eutectic reaction ($L \rightarrow \alpha Al + \theta$ at 548.3 ◦C). Based on, it can

be concluded the temperature in the reaction zone was higher than that measured experimentally.

The Al_4Cu_9 phase is formed probably due to the interdiffusion along the grain boundaries as a result of the friction surfaces dissolution. At temperature greater than 120 °C, there is susceptibility of the Al/Cu interfaces in the solid state to nucleation and form intermetallic compounds [167–169].

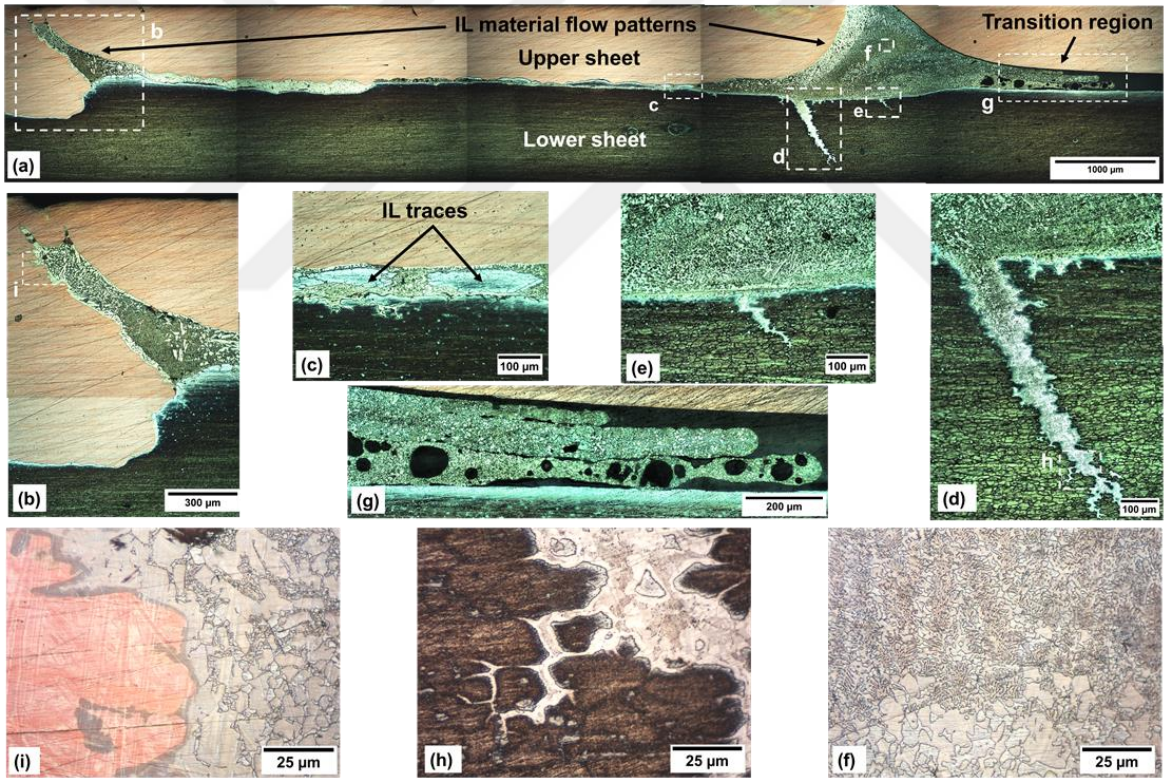

Figure 7.8 Microstructure view of the IL-FSSW weld cross section: (a) morphology at low magnification; (b) interlocking of the intermetallic compound with the upper layer; (c) IL traces; (d) and (e) interlocking of the intermetallic compound with the upper layer; (f) primary dendrite of the intermetallic compounds at the upper sheet; (g) localized solidification defect in the transition region; (h) orientated flow of the intermetallic compounds through the grain boundaries of the aluminum zone; (i) magnified view of the Cu zone.

The view of the intermetallic compounds flow pattern below the tool shoulder can be indicated. Figure 7.8(g) shows some solidified defects into the partially bond region, out of the tool shoulder peripheral, in which some of the intermetallic compounds separated between two matched surfaces through the sheets' interface and introduce the unsymmetrical, peripheral flow pattern around the weld nugget. This region called the transition region, where is the bonding between the sheets is weak [158]. The zoomed image of the selected portion marked c (Figure 7.8(c)) shows that the traces of the IL can be seen clearly surrounded with the intermetallic compound layer. The EDS analysis was observed for the IL-FSSW joint and the results indicated that the major elements present in the intermetallic compound were Cu, Al, and the slightly amount of O_2.

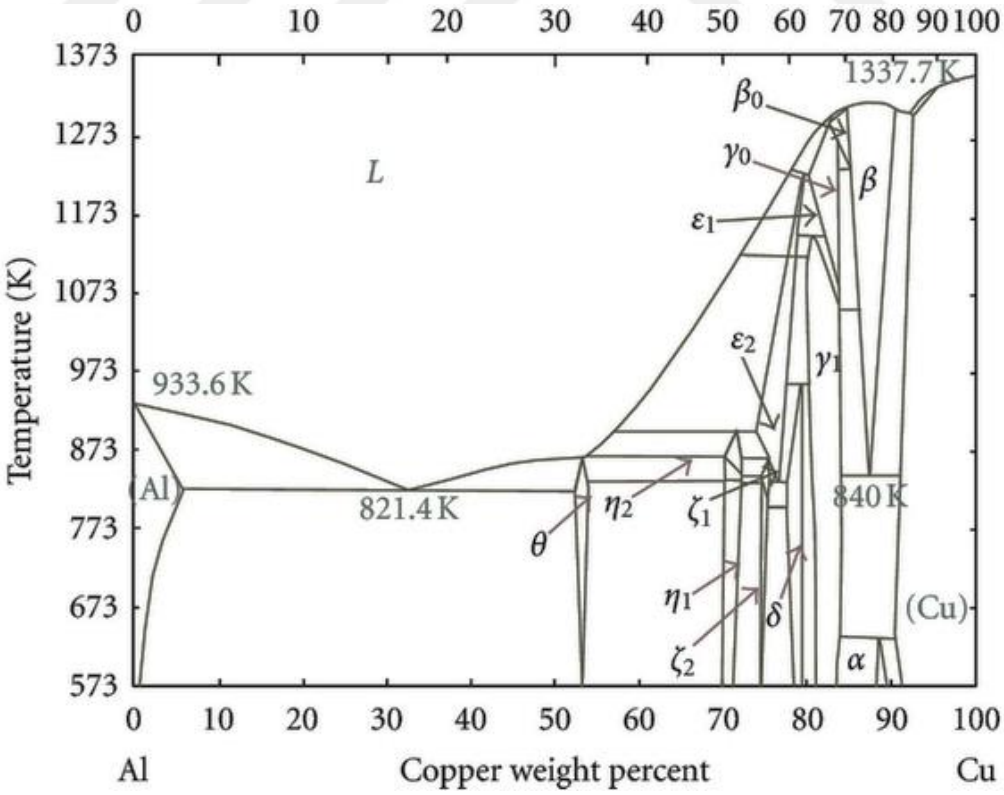

Figure 7.9 Aluminum-copper binary phase diagram [166]

From Figure 7.8(a), it can be seen that the upper sheet mainly consists of parts of the intermetallic compounds, and the grains of these compounds exhibit irregular shapes with a wide size range of 5-25 μm as shown in Figure 7.8(i). The EDS analysis revealed that the average chemical compositions measured at a selected spot (spot 2) of the intermetallic compounds region were 54.7 Al wt% and 47.2 Cu wt% as shown in Figure 7.6(b). The primary dendrites' regions of these compounds are clearly observed at the upper sheet as shown in Figure 7.8(f), and the dendrites exhibit a flower-like of size less than 1 μm. These dendrites are supposed to nucleate and grow from the liquid phase directly to show the random/asymmetric growth morphologies of the intermetallic compounds crystals at the edges of the Cu zone that were deformed as shown in Figures 7.8(a), (b), (i), and (f). Similar observations of the intermetallic compounds in both the friction stir welding and the cold roll welding of the Cu-Al bimetal system were also detected with different morphologies at the narrow weld zones [75,168].

Figures 7.8(d), (e), and (h) illustrate that one of the most interesting features is the microstructural change at the bottom zones of the weld nugget. A perusal of the flowing-like intermetallic compounds intercalated into the boundaries of the grains in the lower sheet before dissolving these grains (Figure 7.8(h)), which formed these deep, complex root-like structures, enables the visualization of the fascinating solid-state flow phenomena. Moreover, it reveals the complex inter-diffusion and chemical interaction between the materials grains of the upper and the lower sheets, and the IL part.

7.5 Fracture Morphology Analysis

Figure 7.10 illustrates the fracture surfaces of both the aluminum and copper sides of the welded joint after the shear-tensile test, and the fracture morphologies were studied using SEM to obtain an understanding of the failure modes. Figures 7.10(c) and (e) show the low magnification fracture features of the lower sheet (top surface) and upper sheet (bottom surface), respectively. As seen, high deformation takes place in the weld nugget before the fracture. Figure 7.10(b) shows the SEM zoomed view of the bonded region below the tool surface at the periphery of the nugget. The small equiaxed dimples elongated along the loading direction with the micro voids indicated that the failure occurred under the shear mode. Figure 7.10(d) shows the dimples that elongated with the loading direction, which indicated that the sheets separation occurred under the shear mode. Figure 7.10(f) shows the layers of the ridges that are formed under the stirring action of the tool. Figure 7.10(g) shows the overhead view of the transition bonding region that is showed in Figure 7.8(g), in which the specimen fails under the adhesion and shear fracture. The SEM image here revealed the separation of intermetallic compounds between the matched surfaces. The fracture in some regions is noted as a typical brittle with no dimples due to the cleavage fracture mode as shown in Figure 7.10(a) and (h). This is mainly due to the intermetallic compounds as well as the oxide formation at these regions. According to these observations, the fracture mode of the Pure Cu/Al welds were made by IL-FSSW process, can be defined as a mixed mode, with combined brittle and ductile fracture types.

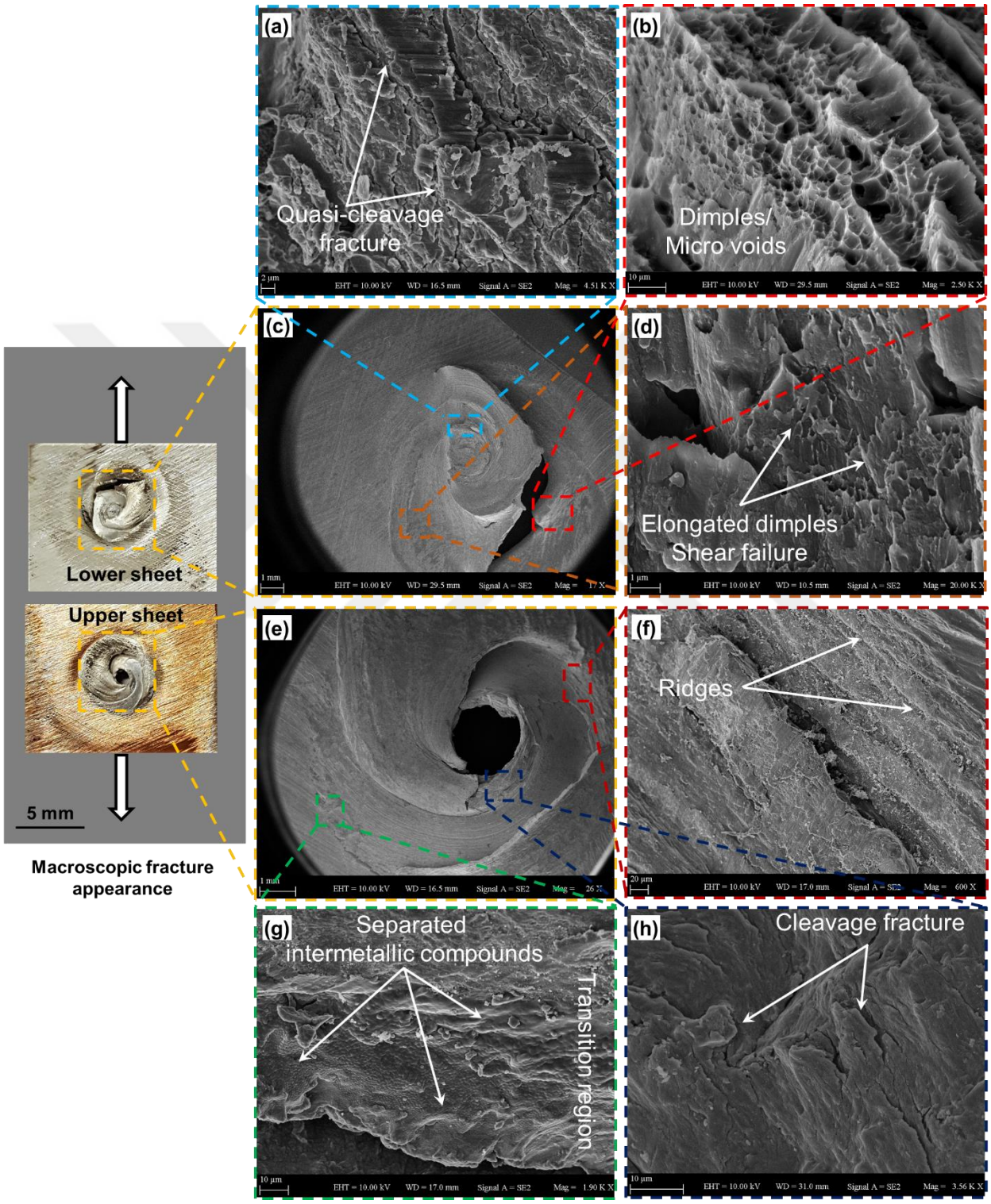

Figure 7.10 Fracture morphologies of Al/Pure Cu dissimilar joint weld by the IL-FSSW, and the load direction is vertical

7.6 Summary of Al 6061/Cu Welds Fabricated by IL-FSSW

Two sheets of Al 6061-O aluminum alloy and pure copper were lap joined successfully by the IL-FSSW and conventional FSSW processes. Mechanical tests, fracture analyses, and XRD were performed. Flat, uniform weld joints were achieved with the IL-FSSW process without the keyhole defect that forms in the conventional FSSW joints. The microscopic results revealed formation of intermetallic compounds at the interface of the sheets' surface mainly consisted of Al_2Cu and Al_4Cu_9. The experiments showed greater microhardness values on the area covered by intermetallic compounds than that of the base metals, which effects to increasing in the hardness values in some regions on the weld cross section. Regarding to the shear-tensile results, the weld strength obtained in IL-FSSW process was not too much higher than that of the conventional FSSW process. The fractural analysis micrographic and the SEM images showed a mixed failure mode, and the presence of dimples indicating a ductile fracture as well as a cleavage or brittle fracture, was also observed in some regions from the fracture surfaces.

CHAPTER VIII

CONCLUSION

From the results, we can conclude the new IL-FSSW process can be used successfully to fabricate spot welds from similar and dissimilar sheet. The keyhole, which classified as a defect in the conventional FSSW, is eliminated. Welds with no keyhole were achieved with acceptable strength. The conclusions from the present work are given in the following:

1. The keyhole, which commonly forms using traditional FSSW is eliminated by using the IL-FSSW process, flat weld joints were achieved. From the observations the bonding at the boundary interface between the upper and lower sheets is adequate.

2. The welding parameters required to achieve the optimal strength of the IL-FSSW welds were as follows; for Al 2024-O/Al 6061-O, similar Al 6061-T6, and similar Al 2024-O sheets of 1.0 mm thick, and the rotational speed and plunging feed rates were 1200 rpm and 20 mm/min, respectively. While for the welding of Al 2024-T6/Al 6061-T6 and similar Al 2024-T6 sheets, the dominant rotational speed and plunging feed rate was 1500 rpm and 25 mm/min, respectively, whereas for the welding of the similar Al 6061-O sheets, the dominant rotational speed and plunging feed rate was 900 rpm and 15 mm/min, respectively.

3. For the IL-FSSW welding process of pure commercial copper to the Al 6061-O sheets of 1.0 mm thick, the rotational speed and plunging feed rate were 1800 rpm and 25 mm/min, respectively.

4. The plunging depth was directly proportional to the strength of the welds. For all the welded samples, the utilized depth was 0.9 mm, which is less than the thickness of the IL part (1 mm).

5. The joint formation of the dissimilar sheets in IL-FSSW process can be attributed to the formation of hooks between the IL and the upper sheets during the welding process. Whereas the joint between the IL and the lower sheets was sole metallurgical bond without hook formation.

6. To assemble two dissimilar sheets by the IL-FSSW, it is recommended to use the higher melting temperature, harder sheets as an upper sheet, while the softer one should be used as a lower sheet and IL part.

7. Regarding the Pure Cu/Al 6061 joint experiments, the microscopic analysis revealed the intermetallic compounds that were formed at the interface of the sheets mainly consisted of the Al_2Cu and Al_4Cu_9 phases. The microhardness test showed that the Hv values of the intermetallic compounds were greater than those of the base metals used, which affected the increase in the joint hardness. Regarding the shear-tensile results, a much higher strength was not obtained at the IL-FSSW weld than that of the conventional FSSW process.

8. Regarding to the fatigue test, the fatigue life of the joints under high applied load is affected by heat treatments. In all groups, the annealing treatment was observed to have a negative effect on the N_f whereas no effect was observed when applying low levels of load. Except in group 2, where the annealing treatment had a positive effect on the N_f.

CHAPTER IX

FUTURE WORKS

Although some effort was made to investigate the mechanical behavior of the friction stir spot welds of the light alloys fabricated by the IL-FSSW in the current study, this method is a novel welding process which needs more experimentation. Therefore, a few suggestions for upcoming research efforts are listed below:

1. Using different process parameters by changing the IL dimensions or tool diameter in order to improve the welds' quality and help to in depth investigation of hook formation.

2. The effect of post heat treatment can be observed in order to enhance the mechanical properties of the processed samples.

3. The IL-FSSW process may be conducted by using different tool materials to join the sheets of the different materials.

4. The research can be extended through using IL or sheets made from other series of aluminum alloys used in the automotive industry such as 1x, 5x, 6x, and 7x. This could help the increase in the use of the IL-FSSW process.

5. Higher thickness aluminum plates can be welded by employing double sided IL-FSSW.

6. The welding of materials such as copper, titanium, magnesium and their alloys by using IL-FSSW is another area of interest.

BIBLIOGRAPHY

[1] A.K. Lakshminarayanan, V. Balasubramanian, K. Elangovan, Effect of welding processes on tensile properties of AA6061 aluminium alloy joints, Int. J. Adv. Manuf. Technol. 40 (2009) 286–296.

[2] R.S. Mishra, Z.Y. Ma, Friction stir welding and processing, Mater. Sci. Eng. R Reports. 50 (2005) 1–78.

[3] M.A. Sutton, B. Yang, A.P. Reynolds, R. Taylor, Microstructural studies of friction stir welds in 2024-T3 aluminum, Mater. Sci. Eng. A. 323 (2002) 160–166.

[4] H. Lipowsky, E. Arpaci, Copper in the automotive industry, John Wiley & Sons, 2008.

[5] G.M. Xie, Z.Y. Ma, L. Geng, Development of a fine-grained microstructure and the properties of a nugget zone in friction stir welded pure copper, Scr. Mater. 57 (2007) 73–76.

[6] R.L.O. Brien, N.W.L. Road, Jefferson's Welding Encyclopedia, 18th ed., American Welding Society, 1997.

[7] D.A. Wang, S.C. Lee, Microstructures and failure mechanisms of friction stir spot welds of aluminum 6061-T6 sheets, J. Mater. Process. Technol. 186 (2007) 291–297. doi:10.1016/j.jmatprotec.2006.12.045.

[8] S. Babu, V.S. Sankar, G.D.J. Ram, P. V Venkitakrishnan, G.M. Reddy, K.P. Rao, Microstructures and mechanical properties of friction stir spot welded aluminum alloy AA2014, J. Mater. Eng. Perform. 22 (2013) 71–84.

[9] Z.H. Zhang, W.Y. Li, Y. Feng, J.L. Li, Y.J. Chao, Improving mechanical properties of friction stir welded AA2024-T3 joints by using a composite backplate, Mater. Sci. Eng. A. 598 (2014) 312–318.

[10] Y.Q. Zhao, H.J. Liu, S.X. Chen, Z. Lin, J.C. Hou, Effects of sleeve plunge depth on

microstructures and mechanical properties of friction spot welded alclad 7B04-T74 aluminum alloy, Mater. Des. 62 (2014) 40–46. doi:10.1016/j.matdes.2014.05.012.

[11] M. Reimann, T. Gartner, U. Suhuddin, J. Göbel, J.F. Dos Santos, Keyhole closure using friction spot welding in aluminum alloy 6061-T6, J. Mater. Process. Technol. 237 (2016) 12–18. doi:10.1016/j.jmatprotec.2016.05.013.

[12] N.T. Kumbhar, K. Bhanumurthy, Friction stir welding of Al 6061 alloy, Asian J. Exp. Sci. 22 (2008) 63–74.

[13] H. Okuyucu, A. Kurt, E. Arcaklioglu, Artificial neural network application to the friction stir welding of aluminum plates, Mater. Des. 28 (2007) 78–84.

[14] S.R. Ren, Z.Y. Ma, L.Q. Chen, Effect of welding parameters on tensile properties and fracture behavior of friction stir welded Al–Mg–Si alloy, Scr. Mater. 56 (2007) 69–72.

[15] R. Nandan, G.G. Roy, T. Debroy, Numerical simulation of three-dimensional heat transfer and plastic flow during friction stir welding, Metall. Mater. Trans. A. 37 (2006) 1247–1259.

[16] T. DebRoy, H. Bhadeshia, Friction stir welding of dissimilar alloys–a perspective, Sci. Technol. Weld. Join. 15 (2010) 266–270.

[17] D.M. Neto, P. Neto, Numerical modeling of friction stir welding process: a literature review, Int. J. Adv. Manuf. Technol. 65 (2013) 115–126.

[18] P. Prasanna, C. Penchalayya, D. Rao, Optimization and validation of process parameters in friction stir welding on AA6061 aluminum alloy using gray relational analysis, Int. J. Eng. Res. Appl. 3 (2013) 1471–1481.

[19] P. Prasanna, B.S. Rao, G.K.M. Rao, A. Prasad, Experimental and numerical evaluation of friction stir welds of AA6061-T6 aluminium alloy, ARPN J. Eng. Appl. Sci. 5 (2010) 1–18.

[20] R. Nandan, T. DebRoy, H. Bhadeshia, Recent advances in friction-stir welding–process, weldment structure and properties, Prog. Mater. Sci. 53 (2008) 980–1023.

[21] S. Guerdoux, Numerical simulation of the friction stir welding process, (2007).

[22] Y.S. Sato, M. Urata, H. Kokawa, Parameters controlling microstructure and hardness during friction-stir welding of precipitation-hardenable aluminum alloy 6063, Metall. Mater. Trans. A. 33 (2002) 625–635.

[23] Y.K. Yang, H. Dong, H. Cao, Y.A. Chang, S. Kou, Liquation of Mg alloys in friction stir spot welding, Weld. JOURNAL-NEW YORK-. 87 (2008) 167.

[24] R. Sakano, Development of spot FSW robot system for automobile body members, in: Proc. 3rd Int. Symp. Frict. Stir Welding, Kobe, Japan, 2004, 2004.

[25] J.H. Sederstrom, Spot friction welding of ultra high-strength automotive sheet steel, (2007).

[26] W. Yuan, R.S. Mishra, B. Carlson, R. Verma, R.K. Mishra, Material flow and microstructural evolution during friction stir spot welding of AZ31 magnesium alloy, Mater. Sci. Eng. A. 543 (2012) 200–209.

[27] D. Klobčar, J. Tušek, A. Skumavc, A. Smolej, Parametric study of friction stir spot welding of aluminium alloy 5754, Metalurgija. 53 (2014) 21–24.

[28] W. Yuan, Friction stir spot welding of aluminum alloys, (2008).

[29] L. Fratini, G. Buffa, CDRX modelling in friction stir welding of aluminium alloys, Int. J. Mach. Tools Manuf. 45 (2005) 1188–1194.

[30] D.S. Sahota, R. Singh, R. Sharma, H. Singh, Study of Effect of Parameters on Resistance Spot Weld of ASS316 Material, Mech. Confab. 2 (2013) 67–78.

[31] Z. Ling, Y. Li, Z. Luo, Y. Feng, Z. Wang, Resistance element welding of 6061 aluminum alloy to uncoated 22MnMoB boron steel, Mater. Manuf. Process. 31 (2016)

2174–2180.

[32] E.P.O. PROCESOV, Experimental comparison of resistance spot welding and friction-stir spot welding processes for the en aw 5005 aluminum alloy, Mater. Tehnol. 45 (2011) 395–399.

[33] K. Feng, M. Watanabe, S. Kumai, Microstructure and joint strength of friction stir spot welded 6022 aluminum alloy sheets and plated steel sheets, Mater. Trans. 52 (2011) 1418–1425.

[34] K. Mori, Y. Abe, A review on mechanical joining of aluminium and high strength steel sheets by plastic deformation, Int. J. Light. Mater. Manuf. (2018).

[35] Q. Yang, S. Mironov, Y.S. Sato, K. Okamoto, Material flow during friction stir spot welding, Mater. Sci. Eng. A. 527 (2010) 4389–4398.

[36] S. Bozzi, A.L. Helbert-Etter, T. Baudin, V. Klosek, J.G. Kerbiguet, B. Criqui, Influence of FSSW parameters on fracture mechanisms of 5182 aluminium welds, J. Mater. Process. Technol. 210 (2010) 1429–1435.

[37] T. Sakiyama, G. Murayama, Y. Naito, K. Saita, Y.M.H. Oikawa, T. Nose, Dissimilar metal joining technologies for steel sheet and aluminum alloy sheet in auto body, Nippon Steel Tech. Rep. 103 (2013) 91–98.

[38] W.-H. Choi, Y.-J. Kwon, S.-O. Yoon, M.-S. Kang, C.-Y. Lim, J.-D. Seo, S.-T. Hong, D.-H. Park, K.-H. Lee, Influence of Welding Parameters on Macrostructure and Mechanical Properties of Friction-Stir-Spot-Welded 5454-O Aluminum Alloy Sheets, J. Weld. Join. 29 (2011) 56–64.

[39] H. Liu, Y. Zhao, X. Su, L. Yu, J. Hou, Microstructural characteristics and mechanical properties of friction stir spot welded 2A12-T4 aluminum alloy, Adv. Mater. Sci. Eng. 2013 (2013).

[40] K. Elangovan, V. Balasubramanian, Influences of tool pin profile and welding speed

on the formation of friction stir processing zone in AA2219 aluminium alloy, J. Mater. Process. Technol. 200 (2008) 163–175.

[41] M.D. Tier, T.S. Rosendo, J.F. dos Santos, N. Huber, J.A. Mazzaferro, C.P. Mazzaferro, T.R. Strohaecker, The influence of refill FSSW parameters on the microstructure and shear strength of 5042 aluminium welds, J. Mater. Process. Technol. 213 (2013) 997–1005. doi:https://doi.org/10.1016/j.jmatprotec.2012.12.009.

[42] M. Merzoug, M. Mazari, L. Berrahal, A. Imad, Parametric studies of the process of friction spot stir welding of aluminium 6060-T5 alloys, Mater. Des. 31 (2010) 3023–3028.

[43] W. Yuan, R.S. Mishra, S. Webb, Y.L. Chen, B. Carlson, D.R. Herling, G.J. Grant, Effect of tool design and process parameters on properties of Al alloy 6016 friction stir spot welds, J. Mater. Process. Technol. 211 (2011) 972–977.

[44] Y.F. Sun, H. Fujii, N. Takaki, Y. Okitsu, Microstructure and mechanical properties of mild steel joints prepared by a flat friction stir spot welding technique, Mater. Des. 37 (2012) 384–392.

[45] M. Goodarzi, S.P.H. Marashi, M. Pouranvari, Dependence of overload performance on weld attributes for resistance spot welded galvanized low carbon steel, J. Mater. Process. Technol. 209 (2009) 4379–4384.

[46] Y. Bozkurt, M.K. Bilici, Application of Taguchi approach to optimize of FSSW parameters on joint properties of dissimilar AA2024-T3 and AA5754-H22 aluminum alloys, Mater. Des. 51 (2013) 513–521.

[47] W.Y. Li, T. Fu, L. Hütsch, J. Hilgert, F.F. Wang, J.F. Dos Santos, N. Huber, Effects of tool rotational and welding speed on microstructure and mechanical properties of bobbin-tool friction-stir welded Mg AZ31, Mater. Des. 64 (2014) 714–720.

[48] L.C. Campanelli, U.F.H. Suhuddin, J.F. dos Santos, N.G. de Alcântara, Parameters optimization for friction spot welding of AZ31 magnesium alloy by Taguchi method,

Soldag. Inspeção. 17 (2012) 26–31. doi:10.1590/S0104-92242012000100005.

[49] C. Schilling, J. dos Santos, Method and device for joining at least two adjoining work pieces by friction welding, (2004).

[50] Y. Bozkurt, S. Salman, G. Çam, Effect of welding parameters on lap shear tensile properties of dissimilar friction stir spot welded AA 5754-H22/2024-T3 joints, Sci. Technol. Weld. Join. 18 (2013) 337–345. doi:10.1179/1362171813Y.0000000111.

[51] Y. Uematsu, K. Tokaji, Y. Tozaki, T. Kurita, S. Murata, Effect of re-filling probe hole on tensile failure and fatigue behaviour of friction stir spot welded joints in Al–Mg–Si alloy, Int. J. Fatigue. 30 (2008) 1956–1966.

[52] Y.F. Sun, H. Fujii, N. Takaki, Y. Okitsu, Novel spot friction stir welding of 6061 and 5052 Al alloys, Sci. Technol. Weld. Join. 16 (2011) 605–612. doi:10.1179/1362171811Y.0000000043.

[53] Y.F. Sun, H. Fujii, N. Takaki, Y. Okitsu, Microstructure and mechanical properties of dissimilar Al alloy/steel joints prepared by a flat spot friction stir welding technique, Mater. Des. 47 (2013) 350–357.

[54] K. Chen, X. Liu, J. Ni, Keyhole refilled friction stir spot welding of aluminum alloy to advanced high strength steel, J. Mater. Process. Technol. 249 (2017) 452–462.

[55] Y. Tozaki, Y. Uematsu, K. Tokaji, A newly developed tool without probe for friction stir spot welding and its performance, J. Mater. Process. Technol. 210 (2010) 844–851. doi:10.1016/j.jmatprotec.2010.01.015.

[56] J.D. Destefani, Properties and selection: Nonferrous alloys and special-purpose materials, ASM Handb. 2 (1992) 1770.

[57] D. Veljic, A. Sedmak, M. Rakin, N. Radović, N. Popović, H. Daşcău, N. Bajic, Advantages of friction stir welding over arc welding with respect to health and environmental protection and work safety, 2015.

[58] M. Perović, S. Baloš, D. Kozak, D. Bajić, T. Vuherer, Influence of kinematic factors of friction stir welding on the characteristics of welded joints of forged plates made of EN AW 7049 A aluminium alloy, Teh. Vjesn. 24 (2017) 723–728.

[59] N.Z. Khan, A.N. Siddiquee, Z.A. Khan, Friction Stir Welding: Dissimilar Aluminium Alloys, CRC Press, 2017.

[60] M. Handbook, Vol. 2-Properties and Selection: Nonferrous Alloys and Special-Purpose Mater, ASM Inter.,. 2 (1992) 464.

[61] S.P. Ringer, K. Hono, Microstructural evolution and age hardening in aluminium alloys: atom probe field-ion microscopy and transmission electron microscopy studies, Mater. Charact. 44 (2000) 101–131.

[62] B.F. Jogi, P.K. Brahmankar, V.S. Nanda, R.C. Prasad, Some studies on fatigue crack growth rate of aluminum alloy 6061, J. Mater. Process. Technol. 201 (2008) 380–384.

[63] M.A. Tashkandi, J.A. Al-Jarrah, M. Ibrahim, Spot Welding of 6061 Aluminum Alloy by Friction Stir Spot Welding Process, Eng. Technol. Appl. Sci. Res. 7 (2017) 1629–1632.

[64] C.D. Cox, B.T. Gibson, A.M. Strauss, G.E. Cook, Effect of pin length and rotation rate on the tensile strength of a friction stir spot-welded al alloy: a contribution to automated production, Mater. Manuf. Process. 27 (2012) 472–478.

[65] J. Chi-Sung, K. Yong-Jai, C.H.O. Hoon-Hwe, H.N. HAN, Material properties of friction stir spot welded joints of dissimilar aluminum alloys, Trans. Nonferrous Met. Soc. China. 22 (2012) s605–s613.

[66] M.K. Abbass, Effect of aging time on the mechanical properties of friction stir spot welding of Al-alloy (AA2024), Int. J. Eng. Res. Appl. 2 (2012) 1366–1374.

[67] M. Paidar, A. Khodabandeh, M.L. Sarab, M. Taheri, Effect of welding parameters (plunge depths of shoulder, pin geometry, and tool rotational speed) on the failure

mode and stir zone characteristics of friction stir spot welded aluminum 2024-T3 sheets, J. Mech. Sci. Technol. 29 (2015) 4639–4644.

[68] M. Paidar, M.L. Sarab, Friction stir spot welding of 2024-T3 aluminum alloy with SiC nanoparticles, J. Mech. Sci. Technol. 30 (2016) 365–370.

[69] S.T. Amancio-Filho, A.P.C. Camillo, L. Bergmann, J.F. Dos Santos, S.E. Kury, N.G.A. Machado, Preliminary investigation of the microstructure and mechanical behaviour of 2024 aluminium alloy friction spot welds, Mater. Trans. 52 (2011) 985–991.

[70] A.B. Handyside, V. Iyer, R. Preston, E. Boldsaikhan, M. McCoy, Process Developement of Integral Fasteners Using Friction Stir Spot Welding With "C-Frame" end Effector on an Aircraft Cabin Door Made From AA6061-T6 and AA2024-T3, in: Frict. Stir Weld. Process. VII, Springer, 2013: pp. 215–224.

[71] C.D. Association, The Copper Advantage. A guide to working with copper and copper alloys, (2010).

[72] X. Li, D. Zhang, Q.I.U. Cheng, W. Zhang, Microstructure and mechanical properties of dissimilar pure copper/1350 aluminum alloy butt joints by friction stir welding, Trans. Nonferrous Met. Soc. China. 22 (2012) 1298–1306.

[73] E.T. Akinlabi, S.A. Akinlabi, Effect of heat input on the properties of dissimilar friction stir welds of aluminium and copper, Am. J. Mater. Sci. 2 (2012) 147–152.

[74] S. Kahl, W. Osikowicz, Composite aluminum-copper sheet material by friction stir welding and cold rolling, J. Mater. Eng. Perform. 22 (2013) 2176–2184.

[75] J. Ouyang, E. Yarrapareddy, R. Kovacevic, Microstructural evolution in the friction stir welded 6061 aluminum alloy (T6-temper condition) to copper, J. Mater. Process. Technol. 172 (2006) 110–122.

[76] U. Özdemir, S. Sayer, Ç. Yeni, Effect of pin penetration depth on the mechanical

properties of friction stir spot welded aluminum and copper, Mater. Test. 54 (2012) 233–239.

[77] R. Heideman, C. Johnson, S. Kou, Metallurgical analysis of Al/Cu friction stir spot welding, Sci. Technol. Weld. Join. 15 (2010) 597–604.

[78] J. Shen, D. Wang, K. Liu, Effects of pin diameter on microstructures and mechanical properties of friction stir spot welded AZ31B magnesium alloy joints, Sci. Technol. Weld. Join. 17 (2012) 357–363.

[79] M.K. Bilici, A.İ. Yükler, M. Kurtulmuş, The optimization of welding parameters for friction stir spot welding of high density polyethylene sheets, Mater. Des. 32 (2011) 4074–4079.

[80] S. Bozzi, A.L. Helbert-Etter, T. Baudin, B. Criqui, J.G. Kerbiguet, Intermetallic compounds in Al 6016/IF-steel friction stir spot welds, Mater. Sci. Eng. A. 527 (2010) 4505–4509.

[81] H.-S. Shin, Y.-C. Jung, Characteristics of friction stir spot welding of Zr-based bulk metallic glass sheets, J. Alloys Compd. 504 (2010) S279–S282.

[82] Y. Hovanski, M.L. Santella, G.J. Grant, Friction stir spot welding of hot-stamped boron steel, Scr. Mater. 57 (2007) 873–876.

[83] C.M. Douglas, Design and analysis of experiments, John Wiley Sons. 5th (2001) 684.

[84] M.C. Cakir, A. Gurarda, Optimization and graphical representation of machining conditions in multi-pass turning operations, Comput. Integr. Manuf. Syst. 11 (1998) 157–170.

[85] I. Mukherjee, P.K. Ray, A review of optimization techniques in metal cutting processes, Comput. Ind. Eng. 50 (2006) 15–34.

[86] M.S. Phadke, Quality engineering using robust design, Prentice Hall PTR, 1995.

[87] Y. V Hui, L.C. Leung, R. Linn, Optimal machining conditions with costs of quality and tool maintenance for turning, Int. J. Prod. Res. 39 (2001) 647–665.

[88] Y. Bozkurt, M.K. Bilici, Application of Taguchi approach to optimize of FSSW parameters on joint properties of dissimilar AA2024-T3 and AA5754-H22 aluminum alloys, Mater. Des. 51 (2013) 513–521. doi:10.1016/j.matdes.2013.04.074.

[89] R.N. Verastegui, J.A. Esmerio Mazzaferro, C.C. Petry Mazzaferro, T.R. Strohaecker, J.F. Dos Santos, Welding of Aluminum to DP600 Steel Plates by Refill Friction Stir Spot Welding Process (Refill FSSW): Preliminary Results., Adv. Mater. Res. 1082 (2014).

[90] R.K. Kassab, H. Champliaud, N. Van Lê, J. Lanteigne, M. Thomas, Experimental and finite element analysis of a T-joint welding, J. Mech. Eng. Autom. 2 (2012) 411–421.

[91] A. Inc., ANSYS Mechanical APDL Theory Reference, (2013).

[92] K.-J. Bathe, Finite element procedures, Klaus-Jurgen Bathe, 2006.

[93] M. Awang, V.H. Mucino, Z. Feng, S.A. David, Thermo-mechanical modeling of friction stir spot welding (FSSW) process: use of an explicit adaptive meshing scheme, SAE Technical Paper, 2005.

[94] Z. Gao, F. Krumphals, P. Sherstnev, N. Enzinger, J.T. Niu, C. Sommitsch, Analysis of plastic flow during friction stir spot welding using finite element modelling, in: Key Eng. Mater., Trans Tech Publ, 2012: pp. 419–424.

[95] S.U. Khosa, T. Weinberger, N. Enzinger, Thermo-mechanical investigations during friction stir spot welding (FSSW) of AA6082-T6, Weld. World. 54 (2010) R134–R146.

[96] W. Fricke, Fatigue analysis of welded joints: state of development, Mar. Struct. 16 (2003) 185–200.

[97] P.L. Threadgill, A.J. Leonard, H.R. Shercliff, P.J. Withers, Friction stir welding of

aluminium alloys, Int. Mater. Rev. 54 (2009) 49–93.

[98] P.-C. Lin, J. Pan, T. Pan, Failure modes and fatigue life estimations of spot friction welds in lap-shear specimens of aluminum 6111-T4 sheets. Part 2: Welds made by a flat tool, Int. J. Fatigue. 30 (2008) 90–105.

[99] S. Hassanifard, M. Zehsaz, F. Esmaeili, Spot weld arrangement effects on the fatigue behavior of multi-spot welded joints, J. Mech. Sci. Technol. 25 (2011) 647.

[100] S. Joy-A-Ka, Y. Ogawa, A. Sugeta, Y.F. Sun, H. Fujii, Fatigue fracture mechanism on friction stir spot welded joints using 300 MPa-class automobile steel sheets under constant and variable force amplitude, Procedia Mater. Sci. 3 (2014) 537–543.

[101] D.-A. Wang, C.-H. Chen, Fatigue lives of friction stir spot welds in aluminum 6061-T6 sheets, J. Mater. Process. Technol. 209 (2009) 367–375.

[102] P.-C. Lin, Z.-M. Su, R.-Y. He, Z.-L. Lin, Failure modes and fatigue life estimations of spot friction welds in cross-tension specimens of aluminum 6061-T6 sheets, Int. J. Fatigue. 38 (2012) 25–35.

[103] S. Hassanifard, M. Mohammadpour, H.A. Rashid, A novel method for improving fatigue life of friction stir spot welded joints using localized plasticity, Mater. Des. 53 (2014) 962–971.

[104] H. Chandler, Heat treater's guide: practices and procedures for nonferrous alloys, ASM international, 1996.

[105] J.R. Kissell, R.L. Ferry, Aluminum structures: a guide to their specifications and design, John Wiley & Sons, 2002.

[106] G.E. Totten, D.S. MacKenzie, Handbook of Aluminum: Vol. 1: Physical Metallurgy and Processes, CRC Press, 2003.

[107] J.F. Occasione, Atmospheric Corrosion Investigation of Aluminum Coated, zinc Coated, and Copper Bearing Steel Wire and Wire Products (a Twelve Year Report),

ASTM International, 1984.

[108] M. Koilraj, V. Sundareswaran, S. Vijayan, S.R.K. Rao, Friction stir welding of dissimilar aluminum alloys AA2219 to AA5083–Optimization of process parameters using Taguchi technique, Mater. Des. 42 (2012) 1–7.

[109] A.K. Lakshminarayanan, V. Balasubramanian, Process parameters optimization for friction stir welding of RDE-40 aluminium alloy using Taguchi technique, Trans. Nonferrous Met. Soc. China. 18 (2008) 548–554.

[110] A.W. Society., C. on A. Welding., A.W. Society., T.A. Committee., A.N.S. Institute., Specification for automotive weld quality--resistance spot welding of steel, 2013.

[111] A. Commite, ASTM E92, Stand. Test Methods Vickers Hardness Met. Mater. 3 (2017).

[112] P.. American Society for Testing and Materials (Filadelfia, ASTM E3-01: Standard Guide for Preparation of Metallographic Specimens, in: ASTM, 2009.

[113] A.S.M.H. Vol, 9: Metallography and Microstructures, ASM Int. Mater. Park. OH. (2004).

[114] H.-R. Wenk, P. Van Houtte, Texture and anisotropy, Reports Prog. Phys. 67 (2004) 1367.

[115] Z. Zhang, X. Yang, J. Zhang, G. Zhou, X. Xu, B. Zou, Effect of welding parameters on microstructure and mechanical properties of friction stir spot welded 5052 aluminum alloy, Mater. Des. 32 (2011) 4461–4470.

[116] Q. Yang, X. Li, K. Chen, Y.J. Shi, Effect of tool geometry and process condition on static strength of a magnesium friction stir lap linear weld, Mater. Sci. Eng. A. 528 (2011) 2463–2478.

[117] A.G. Wiedenhoft, H.J. de Amorim, T. de S. Rosendo, M.A.D. Tier, A. Reguly, Effect of Heat Input on the Mechanical Behaviour of Al-Cu FSW Lap Joints, Mater. Res. 21

(2018).

[118] A. Kubit, M. Bucior, D. Wydrzyński, T. Trzepieciński, M. Pytel, Failure mechanisms of refill friction stir spot welded 7075-T6 aluminium alloy single-lap joints, Int. J. Adv. Manuf. Technol. 94 (2018) 4479–4491.

[119] Y. Tozaki, Y. Uematsu, K. Tokaji, Effect of processing parameters on static strength of dissimilar friction stir spot welds between different aluminium alloys, Fatigue Fract. Eng. Mater. Struct. 30 (2007) 143–148.

[120] Y. Tozaki, Y. Uematsu, K. Tokaji, Effect of tool geometry on microstructure and static strength in friction stir spot welded aluminium alloys, Int. J. Mach. Tools Manuf. 47 (2007) 2230–2236. doi:10.1016/j.ijmachtools.2007.07.005.

[121] T. Rosendo, B. Parra, M.A.D. Tier, A.A.M. da Silva, J.F. dos Santos, T.R. Strohaecker, N.G. Alcântara, Mechanical and microstructural investigation of friction spot welded AA6181-T4 aluminium alloy, Mater. Des. 32 (2011) 1094–1100. doi:https://doi.org/10.1016/j.matdes.2010.11.017.

[122] Z. Shen, X. Yang, S. Yang, Z. Zhang, Y. Yin, Microstructure and mechanical properties of friction spot welded 6061-T4 aluminum alloy, Mater. Des. 54 (2014) 766–778.

[123] M. Fujimoto, S. Koga, N. Abe, Y.S. Sato, H. Kokawa, Microstructural analysis of stir zone of Al alloy produced by friction stir spot welding, Sci. Technol. Weld. Join. 13 (2008) 663–670. doi:10.1179/136217108x347601.

[124] R.S. Mishra, Z.Y. Ma, Friction stir welding and processing, Mater. Sci. Eng. R Reports. 50 (2005) 1–78. doi:10.1016/j.mser.2005.07.001.

[125] P.B. Prangnell, C.P. Heason, Grain structure formation during friction stir welding observed by the ‘stop action technique,’ Acta Mater. 53 (2005) 3179–3192.

[126] X. Sauvage, A. Dédé, A.C. Munoz, B. Huneau, Precipitate stability and

recrystallisation in the weld nuggets of friction stir welded Al–Mg–Si and Al–Mg–Sc alloys, Mater. Sci. Eng. A. 491 (2008) 364–371.

[127] M. Mohammadtaheri, M. Haddad-Sabzevar, M. Mazinani, The Effects of Heat Treatment and Cold Working on the Microstructure of Aluminum Alloys Welded by Friction Stir Welding (FSW) Technique, in: Adv. Mater. Res., Trans Tech Publ, 2012: pp. 287–292.

[128] L. Zhou, D. Liu, K. Nakata, T. Tsumura, H. Fujii, K. Ikeuchi, Y. Michishita, Y. Fujiya, M. Morimoto, New technique of self-refilling friction stir welding to repair keyhole, Sci. Technol. Weld. Join. 17 (2012) 649–655.

[129] I.J. Ibrahim, G.G. Yapici, Optimization of the Intermediate Layer Friction Stir Spot Welding Process, Int. J. Adv. Manuf. Technol. (2019).

[130] Y. Uematsu, K. Tokaji, Comparison of fatigue behaviour between resistance spot and friction stir spot welded aluminium alloy sheets, Sci. Technol. Weld. Join. 14 (2009) 62–71.

[131] I.J. Ibrahim, G.G. Yapici, Application of a novel friction stir spot welding process on dissimilar aluminum joints, J. Manuf. Process. 35 (2018) 282–288.

[132] T.-Y. Pan, Friction Stir Spot Welding (FSSW)-A Literature Review, SAE Technical Paper, 2007.

[133] Z. Shen, X. Yang, Z. Zhang, L. Cui, Y. Yin, Mechanical properties and failure mechanisms of friction stir spot welds of AA 6061-T4 sheets, Mater. Des. 49 (2013) 181–191.

[134] H. Aydın, A. Bayram, A. Uğuz, K.S. Akay, Tensile properties of friction stir welded joints of 2024 aluminum alloys in different heat-treated-state, Mater. Des. 30 (2009) 2211–2221.

[135] Z. Li, S. Ji, Y. Ma, P. Chai, Y. Yue, S. Gao, Fracture mechanism of refill friction stir

spot-welded 2024-T4 aluminum alloy, Int. J. Adv. Manuf. Technol. 86 (2016) 1925–1932.

[136] X. Song, L. Ke, L. Xing, F. Liu, C. Huang, Effect of plunge speeds on hook geometries and mechanical properties in friction stir spot welding of A6061-T6 sheets, Int. J. Adv. Manuf. Technol. 71 (2014) 2003–2010.

[137] S.D. Ji, X.C. Meng, R.F. Huang, L. Ma, S.S. Gao, Microstructures and mechanical properties of 7N01-T4 aluminum alloy joints by active-passive filling friction stir repairing, Mater. Sci. Eng. A. 664 (2016) 94–102. doi:10.1016/j.msea.2016.03.131.

[138] S. Venukumar, S.G. Yalagi, S. Muthukumaran, S. V Kailas, Static shear strength and fatigue life of refill friction stir spot welded AA 6061-T6 sheets, Sci. Technol. Weld. Join. 19 (2014) 214–223.

[139] P.S. Effertz, V. Infante, L. Quintino, U. Suhuddin, S. Hanke, J.F. Dos Santos, Fatigue life assessment of friction spot welded 7050-T76 aluminium alloy using Weibull distribution, Int. J. Fatigue. 87 (2016) 381–390.

[140] A.A. Zainulabdeen, M.K. Abbass, A.H. Ataiwi, S.K. Khanna, B. Jashti, C. Widener, Investigation of fatigue behavior and fractography of dissimilar friction stir welded joints of aluminum alloys 7075-T6 and 5052-H34, (2014).

[141] K.H. Huebner, D.L. Dewhirst, D.E. Smith, T.G. Byrom, The finite element method for engineers, John Wiley & Sons, 2008.

[142] M.H. Majeed, Effects of Welding Parameters on Temperature Distribution and Tensile Strength of AA6061-T6 Welded by Friction Stir Welding, J. Eng. 21 (2015) 24–39.

[143] R. Silva, Direct Coupled Thermal-Structural Analysis in ANSYS WorkBench, in: ESSS Conf. Ansys Users Meet. Atibaia, Bras., 2013.

[144] A. Kumar, Computational & Experimental Analysis of Rotational Speed of Friction Stir Weld Tool, 2 (2013) 505–511.

[145] M. Awang, Simulation of friction stir spot welding (FSSW) process: study of friction phenomena, West Virginia University, 2007.

[146] T.D. Canonsburg, ANSYS Mechanical APDL Command Reference, ANSYS Man. 15317 (2010) 724–746. doi:www.ansys.com.

[147] K.N. Salloomi, L.A. Sabri, Y.M. Hamad, S.N. Mohammed, 3-Dimensional Nonlinear Finite Element Analysis of both Thermal and Mechanical Response of Friction Stir Welded 2024-T3 Aluminium Plates, J. Inf. Eng. Appl. 3 (2013) 6–15.

[148] B.G. Kıral, M. Tabanoğlu, H.T. Serindağ, Finite element modeling of friction stir welding in aluminum alloys joint, Math. Comput. Appl. 18 (2013) 122–131.

[149] Y.J. Chao, X. Qi, W. Tang, Heat transfer in friction stir welding—experimental and numerical studies, J. Manuf. Sci. Eng. 125 (2003) 138–145.

[150] X.K. Zhu, Y.J. Chao, Effects of temperature-dependent material properties on welding simulation, Comput. Struct. 80 (2002) 967–976.

[151] A.P.D.M.N. Hamzah, A.P.D.S.H. Bakhy, M.A. Fliayyh, Numerical and Experimental Investigations of Transient Temperature Distribution in Friction Stir Spot Welding of Aluminum Alloy AA6061, Al-Qadisiya J. Eng. Sci. 9 (2016) 388–407.

[152] Z. Na, Y. YANG, H. Ming, L.U.O. Xian, G. FENG, R. ZHANG, Finite element analysis of pressure on 2024 aluminum alloy created during restricting expansion-deformation heat-treatment, Trans. Nonferrous Met. Soc. China. 22 (2012) 2226–2232.

[153] M. Zahedul Huq. Khandkar, Thermo-mechanical modeling of friction stir welding /, 2005.

[154] H. Raikoty, I. Ahmed, G.E. Talia, High speed friction stir welding: a computational and experimental study, in: ASME 2005 Summer Heat Transf. Conf. Collocated with ASME 2005 Pacific Rim Tech. Conf. Exhib. Integr. Packag. MEMS, NEMS, Electron.

Syst., American Society of Mechanical Engineers, 2005: pp. 431–436.

[155] X.K. Zhu, Y.J. Chao, Numerical simulation of transient temperature and residual stresses in friction stir welding of 304L stainless steel, J. Mater. Process. Technol. 146 (2004) 263–272.

[156] P.J. Blau, Friction science and technology: from concepts to applications, CRC press, 2008.

[157] D. John, B. Douglas, M. Pavel, Thermal Modeling of a Friction Bonding Process, Idaho National Laboratory (United States). Funding organisation: DOE-NE (United States), 2007.

[158] A. Garg, A. Bhattacharya, Strength and failure analysis of similar and dissimilar friction stir spot welds: influence of different tools and pin geometries, Mater. Des. 127 (2017) 272–286.

[159] M. Aravind, P. Yu, M.Y. Yau, D.H.L. Ng, Formation of Al2Cu and AlCu intermetallics in Al (Cu) alloy matrix composites by reaction sintering, Mater. Sci. Eng. A. 380 (2004) 384–393.

[160] C. Meran, The joint properties of brass plates by friction stir welding, Mater. Des. 27 (2006) 719–726.

[161] H.I. Dawood, K.S. Mohammed, A. Rahmat, M.B. Uday, Microstructural Characterizations and Mechanical Properties in Friction Stir Welding Technique of Dissimilar (Al-Cu) Sheets, J. Appl. Sci. Agric. 10 (2015) 149.

[162] L.E. Murrr, Y. Li, E. Trillo, J.C. McClure, Fundamental issues and industrial applications of friction-stir welding, Mater. Technol. 15 (2000) 37–48.

[163] L.E. Murr, Microstructures in friction-stir welded metals, J. Mater. Process. Manuf. Sci. 7 (1998) 145–161.

[164] Y. Li, E.A. Trillo, L.E. Murr, Friction-stir welding of aluminum alloy 2024 to silver,

J. Mater. Sci. Lett. 19 (2000) 1047–1051.

[165] L.E. Murr, R.D. Flores, O. V Flores, J.C. McClure, G. Liu, D. Brown, Friction-stir welding: microstructural characterization, Mater. Res. Innov. 1 (1998) 211–223.

[166] A.S.M. Handbook, vol. 3, Alloy Phase Diagrams, ASM INTERNATIONAL, Materials Park, OH, 1992, Google Sch. (n.d.) 206.

[167] J. Ouyang, E. Yarrapareddy, R. Kovacevic, Microstructural evolution in the friction stir welded 6061 aluminum alloy (T6-temper condition) to copper, J. Mater. Process. Technol. 172 (2006) 110–122. doi:10.1016/j.jmatprotec.2005.09.013.

[168] M. Aritoshi, K. Okita, T. Enjo, K. Ikeuchi, F. Matsuda, Friction welding of oxygen free copper to pure aluminium, Weld. Int. 6 (1992) 853–859.

[169] M. Abbasi, A.K. Taheri, M.T. Salehi, Growth rate of intermetallic compounds in Al/Cu bimetal produced by cold roll welding process, J. Alloys Compd. 319 (2001) 233–241.

VITA

Isam Jabbar Ibrahim was born in 1983 in Baghdad, Iraq. After getting a technical diploma in Mechanics Techniques/Production from the Institute of Technology-Baghdad in 2002, he enrolled on a Bachelor's and Master's program at the Middle Technical University. He received his Bachelor's in Engineering in Welding Techniques in 2005. He finished his Master's in Welding Engineering Technology in 2009. Then, he worked at the same university as a lecturer in the Welding Engineering Department for four years. In 2013, he received a scholarship from the Iraqi Government to complete his doctoral studies in the Republic of Turkey. Currently, he is pursuing a PhD degree in Mechanical Engineering at Ozyegin University under the supervision of Associate Professor Dr. Guney Guven Yapici in MEMFIS research group. His research interest is mainly concentrated on developing a novel friction stir welding process called Intermediate Layer Friction Stir Spot Welding (IL-FSSW).